NASA-CR-197024

MCAT Institute
Annual Report
94-20

Control of Unsteady Separated Flow Associated With the Dynamic Stall of Airfoils

M. C. Wilder

July 1994

NCC2-637

MCAT Institute
3933 Blue Gum Drive
San Jose, CA 95127

Annual Report for Cooperative Agreement No. NCC2-637
31 July 1994

Control of Unsteady Separated Flow Associated With the Dynamic Stall of Airfoils

M. C. Wilder
MCAT Institute, San Jose, CA 95127

Abstract

A unique active flow-control device is proposed for the control of unsteady separated flow associated with the dynamic stall of airfoils. The device is an adaptive-geometry leading-edge which will allow controlled, dynamic modification of the leading-edge profile of an airfoil while the airfoil is executing an angle-of-attack pitch-up maneuver. A carbon-fiber composite skin has been bench tested, and a wind tunnel model is under construction. A baseline parameter study of compressible dynamic stall was performed for flow over an NACA 0012 airfoil. Parameters included Mach number, pitch rate, pitch history, and boundary layer tripping. Dynamic stall data were recorded via point-diffraction interferometry and the interferograms were analyzed with in-house developed image processing software. A new high-speed phase-locked photographic image recording system was developed for real-time documentation of dynamic stall.

Nomenclature

C_p	pressure coefficient
c	airfoil chord
f	oscillation frequency, Hz
k	reduced frequency, $\frac{\pi f c}{U_\infty}$
M	free stream Mach number
Re	Reynolds number based on c and U_∞
U_∞	free stream velocity
x,y	chordwise and vertical distance
α	angle of attack
$\dot{\alpha}$	pitch rate in deg/sec
α^+	nondimensional pitch rate, $\frac{\dot{\alpha} c}{U_\infty}$
γ	ratio of specific heats
ϵ	fringe number
ρ	density
ρ_r	density at reference (atmospheric) conditions

I. Introduction

The maneuverability of many modern aircraft is limited by the prospect of such unsteady separated flow phenomena as flutter and dynamic stall. Dynamic stall is an un-

steady fluid dynamics phenomena in which enhanced lift is produced through the rapid pitch-up of an airfoil. Flow over the pitching airfoil remains attached beyond the static stall angle of attack and high lift is produced. But, as the angle continues to increase, the flow eventually separates near the leading edge and a vortex is formed. This dynamic stall vortex initially acts to further enhance the lift by creating a low pressure region over the airfoil. As the vortex is convected downstream, however, the airfoil experiences large pitching moment fluctuations and eventually enters deep stall. The dynamic stall phenomenon is further complicated by fluid compressibility effects. Compressibility becomes a factor even at moderate freestream Mach numbers around M = 0.2[1], and has the affect of advancing the onset angle-of-attack of dynamic stall, rendering the high lift generated unexploitable in most flight domains. Carr et al[2] demonstrated that dynamic stall of an oscillating NACA 0012 airfoil changes from a trailing-edge stall to a leading-edge stall when compressibility effects become significant. It was also shown that a supercritical airfoil, the NLR-7301, exhibited trailing-edge stall even at compressible Mach number flows. Supercritical airfoils, though, are designed for use at transonic speeds and are inefficient at lower compressible speeds (e.g. $M \sim 0.3 - 0.5$).

The concept of this project is to develop an adaptive-geometry airfoil surface capable of changing from a baseline NACA 0012 profile to a supercritical profile while executing a dynamic-stall maneuver. The increased thickness of the supercritical leading-edge profile should mitigate the compressibility effects, prolonging the lift augmentation of dynamic stall. This change must occur within only a few milliseconds if pitch rates scalable to flight conditions are to be achieved. The challenge is to find a surface material flexible enough to achieve the response time required, yet rigid enough to deform repeatedly, in a controlled fashion, under rapidly varying aerodynamic loads.

A review of the literature indicates that previous experiments in active flow control were performed at low Mach numbers and for steady flow conditions[3,4,5]. Oscillating flaps and oscillatory suction/blowing have been investigated as circulation control techniques[3], but were used on airfoils at steady angles of attack.

Four interconnected lines of investigation are being simultaneously pursued in this research effort. They are:

1) Design, fabrication and testing of a unique adaptive-geometry airfoil, its control hardware and software.

2) Experimental investigations of dynamic stall over a fixed-shape airfoil to establish a baseline for evaluating the performance of the adaptive-geometry airfoil and for providing a thorough understanding of the physics involved in this complex, unsteady flow.

3) Development of a high-speed imaging system for data acquisition of the rapidly developing dynamic stall flow field.

4) Development of improved image analysis techniques for accurately, quickly and efficiently extracting quantified data from interferograms.

II. Description of the Experiments

A. The Dynamic Stall Studies

The dynamic stall experiments were conducted in the Compressible Dynamic Stall

Facility (CDSF) in the Fluid Mechanics Laboratory (FML) of NASA Ames Research Center; part of the in-draft wind tunnel complex at the FML. Refer to Ref. 6 for details of the facility design. Dynamic stall depends on a large number of parameters; including Mach number, Reynolds number, pitch rate, pitch history, and the state of turbulence in the boundary layer over the airfoil. Also, the inception of dynamic stall and the formation of the dynamic stall vortex occur very rapidly. For these reasons this investigation covers a large parameter space, and many data points comprise each parameter set. Experiments were conducted for a range of freestream Mach numbers from M = 0.2 to M = 0.45, corresponding to a Reynolds number range of Re = 2x10^5 to Re = 9x10^5 based on the 7.62 cm (3.0 inch) chord length of the NACA 0012 model. Further experiments are being conducted at the time of writing on a 15.24 cm (6.0 inch) chord NACA 0012 model. The unsteady motion of the airfoil was produced by one of two drive systems. One drive system produced oscillatory motion of the form $\alpha(t) = 10^0 - 10^0 sin\ 2\pi ft$. Oscillation frequencies up to f = 54 Hz were used, giving a reduced frequency range of $0 \leq k \leq 0.1$. The second drive system produced transient pitch-up maneuvers, rapidly pitching the model from 0^0 to 60^0 angle of attack with a linear change in angle. Pitch rates up to 3600^0/sec were possible, giving a nondimensional pitch rate range of $0 \leq \alpha^+ \leq 0.04$. Details of the transient pitch-up drive system are found in Ref. 7. For both drive systems, the airfoil was pitched about the quarter-chord point, and the angle of attack was reported by an 800 count/revolution optical encoder.

The non-intrusive optical flow diagnostic technique of point diffraction interferometry (PDI) was employed in this investigation. The PDI technique produces instantaneous images of the fluid density field around the airfoil in the form of interference fringe patterns. (See fig. 9 and the appendices for example interferograms.) Each fringe represents a line of constant density (averaged across the test section span), and application of the isentropic flow relations yields both global and surface pressure distributions. The analysis techniques applied to the images are described in section III D, and the details of PDI are in Refs. 8, 9.

A new phase-locked, high-speed photographic recording system was developed for use with the PDI technique (see Appendix D for details). The PDI technique employs a pulsed Nd:YAG laser as a light source. Custom equipment was designed in-house to phase-lock the laser pulsing with frame events in a high-speed drum camera, and simultaneously record the angle of attack of the airfoil. With this system, 200 interferograms could be recorded at rates up to 40,000 images/sec. The images were recorded on standard 35mm film, and analyzed digitally on a work station.

B. Adaptive-Geometry Airfoil Bench Tests

Two design approaches have been pursued in developing the adaptive-geometry airfoil. The first approach employed a material that uses electromagnetic repulsive force to change shape. This material was originally designed to forcefully expel ice build-up from the leading-edge of aircraft wings[10]. The material is simply a helical, or coil shaped conductive ribbon embedded in a non-conductive substrate, with the helix flattened. An elastic skin holds the flattened helix to the airfoil surface. The electromagnetic forces that result when a high-voltage pulse is sent through the ribbon cause the helix to open, and the elastic skin

returns the surface to its original shape when the electromagnetic forces have subsided, as is illustrated in Fig. 1. The high-voltage pulse was generated by discharging a capacitor through the coil. Voltages as high as 1000 volts were used.

Because of the intense electromagnetic fields produced at the surface of this material, a photographic method was selected to record the surface shape changes. The shape change, from neutral surface to full deflection and back to neutral surface, lasted from 3.5ms to 10ms. The exact duration depended on the design of the conducting coil and on the voltage of the driving pulse. A high-speed imaging system was developed to capture these rapid surface deflections and is described in Ref. 11. At the heart of the system is the IMACON image converting camera. The camera records up to eight images on 3in x 5in Polaroid film at a rate of 25,000 frames/sec. A TTL pulse emitted coincident with the high-voltage pulse initiated the camera framing cycle and ensured synchronization of the photographic cycle and the airfoil shape-change cycle. Adding a suitable delay to the TTL pulse permitted any portion of the cycle to be recorded. To quantify the surface shape changes, a grid of reflective tape was applied to the elastic skin of the airfoil. Successive photographs were digitized, and polynomial curves were fit to the grid lines using custom designed software. Digitized surface profiles are presented in section III.

A composite material skin was used in the second design approach to the adaptive-geometry airfoil. The skin was formed in the shape of the "deformed" surface and a load was applied to force the skin into the shape of the neutral airfoil (here, an NACA 0012). Releasing the load allowed the skin to return to its original shape. The bench-test model comprised the upper surface of the leading 25% chord of a five times over-sized (760 mm chord) airfoil. The leading-edge was clamped in place and a load was applied at the end of the upper surface (Fig. 2). A load cell measured the force required to deflect the skin to the NACA 0012 shape. This model was used for static loading and unloading tests to determine the strength and durability of the material. Surface shape profiles were photographically recorded and digitally processed. The results are also discussed in section III.

III. Results

A. The Adaptive-Geometry Airfoils

1. Electro-Repulsive Material Skin

Five adaptive-geometry airfoils using the electro-repulsive material have been bench tested. The results for the first model were reported in Ref. 11 and summarized in section III, above. The shape-change produced by this model was highly three-dimensional, and the model was primarily used as a test piece while developing the IMACON high-speed photographic data acquisition system. Based on the data collected for this model, the design of the electro-repulsive material was improved, making two-dimensional shape changes possible. Figure 3 shows several shape profiles determined from the IMACON images.

For the next model, a tighter conducting coil was used. The coil was mounted along the leading edge and extended over the first 25% of the surface. Two different outer skins were tried: one, a thin aluminum sheet held in place with adhesive backed kevlar film;

and the second, the kevlar film alone. The kevlar skin was bound to the trailing 50% of the airfoil and was free to move on the leading 50%. The aluminum skin tended to either prevent the shape change, or remain deflected; depending on how tightly the kevlar skin was applied. Without the aluminum skin a 2.5% deflection was measured at the 15% chord location. The deflection was two-dimensional and reached its maximum in 2.0 ms. However, the leading edge was constrained from movement, and the resulting profile had a sharper nose than the neutral shape. A step also resulted at the downstream end of the conducting coil. Representative profiles are shown in Fig. 4.

The fourth model employed a pair of the conductor coils arranged one atop the other on the leading edge. Again, the surface deflection was constrained at the nose, resulting in a sharp leading edge. The conductor coil was held too tightly when wrapped around the leading edge, and the electromagnetic force produced was insufficient to open the coil.

Finally, a model was constructed with a soft, sponge nose. This configuration is illustrated in Fig. 1. The sponge nose comprised the leading 10% of the airfoil and could be left hollow or stiffened with a sponge insert. A conductor coil extended from ten to thirty percent of the chord on both the upper and surfaces. As the coils opened up, the sponge nose was pulled back, resulting in a rounder leading edge. For both the solid (Fig. 5) and hollow (Fig. 6) nose, maximum deflection occurred in about 5 ms, and 10 ms passed before the surface returned to the neutral shape. This response time was nearly three times slower than for the previous models. Although the required shape change was being approached with this model, the sponge material was too flexible to support the aerodynamic loads expected in the wind tunnel.

At this stage a new approach was examined; constructing a stiff outer skin from carbon-fiber composite, and using mechanical force to effect the shape change.

2. Composite Material Skin

The test fixture sketched in Fig. 2 was used to measure the force required to pull the composite skin leading edge from its pre-formed shape into a NACA 0012 profile. The load was applied by hand-tightening a screw attached to a sliding bracket which clamped to the end of the skin. Displacement at the bracket was recorded verses the applied load, and representative data are presented in Fig. 7. Figure 7a shows the displacement while loading and unloading the surface. The hysteresis in the data was typical and was due to binding in the sliding bracket. The bench tests were also to ensure that the composite skin could endure repeated flexing and still deform in a predictable fashion. The loading/unloading cycle was performed repeatedly and the loading history for the first and 100th cycles are compared in Fig. 7b. Cycle-to-cycle variation were within the measured hysteresis shown in Fig. 7a. A load of 260 lbs (see Fig. 8) was required to achieve an NACA 0012 profile at the leading edge.

Based on these data, a computer controlled actuator is being designed and a 15.24 cm (6.0 in.) chord airfoil model is in the final stage of fabrication. The neutral shape of this model will be a supercritical profile. A metal push bar inside the airfoil and with the shape of an NACA 0012 leading edge will force the leading edge forward, causing the surface to bend inward to the 0012 profile. Stepper motors will provide the force to the push bar; releasing the load will allow the leading edge to spring from the 0012 profile to

the supercritical profile.

B. Dynamic Stall of Fixed-Shape Airfoils

PDI measurements of dynamic stall flow were performed for a sequence of five tripped NACA 0012 airfoils. Forcing the boundary layer to become turbulent is a common means for achieving Reynolds number similarity between low Reynolds number wind tunnel tests and high Reynolds number flight. A review of the literature revealed that estimates on the roughness size required to trip a boundary layer are either made considering zero-pressure-gradient flow over a flat plate, or are empirically determined by measuring the zero-lift drag coefficient for various trip sizes[12]. Such estimates proved not very useful when encountering the inherent unsteadyness and the large adverse pressure gradient encountered downstream of the suction peak in dynamic stall flow. However, the selection of the first trip size was based on formulae found in the literature. Five trips of varying height and chordwise length were tested. The effectiveness of a trip was gaged by the elimination of the laminar separation bubble observed on the untripped airfoil, and by the further delay of dynamic stall onset. Each trip was constructed by gluing a spanwise strip of roughness elements (polishing grit) to the leading edge of the airfoil.

The effects of the first trip on compressible dynamic stall were observed for both a transiently pitching (Appendix B) and an oscillating airfoil (Appendix C). This trip proved to be too high and even advanced stall. The subsequent four trips were used in oscillating airfoil dynamic stall only (Appendix C). The parameter spaces of the trip studies are shown in Tables 1a-1f. A complete set of leading-edge and full-flow-field PDI data were also obtained for the untripped oscillating airfoil; parameters listed in Tables 2a and 2b.

C. High-Speed Imaging

The dynamic stall flow field becomes highly non-linear at the time of boundary-layer separation and dynamic-stall vortex formation. Consequently, the flow field is not perfectly repeatable from cycle to cycle. Therefore, as part of this effort, a system was developed for photographically recording interferometry images at rates up to 40,000 images/sec.

Because of the limited recording time of the IMACON, a second system was developed around the Cordin (Dynafax Model 350 Framing Camera). This system is detailed in Appendix D, but a brief description is given here for completeness. The Cordin records up to 224 16mm-size frames, in two rows, along a strip of standard 35mm film, and is capable of rates up to 40,000 frames/sec. In-house custom-designed and -built hardware provides timing synchronization of the camera frames with the pulsed laser light source and the airfoil angle-of-attack position data. These position data are recorded in a data buffer for each exposure on the film. The advantages of the Cordin include the increased recording time, continuously selectable frames rates up to 40,000 frames/sec, and less expensive, higher resolution film can be used.

Sequences of 200 images have been obtained at frame rates of 11,560 frames/sec and 20,000 frames/sec for an oscillating airfoil at $M = 0.3$ and $M = 0.45$ at a reduced frequency of $k = 0.05$. Data for $M = 0.3$, $k = 0.05$ and 11,560 frames/sec were reported in Appendix D (Ref. 13). At these conditions, the dynamic stall was imaged over a single oscillation cycle with an average resolution of 0.07 degrees/image.

D. Image Analysis

Massive amounts of data can be obtained using the interferometry and imaging techniques described above and, when properly analyzed, each image can yield detailed, quantitative information on both the surface- and global-pressure distributions of the flow. The analysis procedure begins with rendering the photographic images in digital form for representation and manipulation on a computer work station. Digitization is performed with a Sharp color scanner at 300 dpi (dots per inch) resolution. Grayscale images are created with 256 possible intensity levels for each pixel. Images are typically from 700 to 900 square pixels in size requiring approximately 0.5 to 1 Megabyte of storage on the computer.

Quantitative data are extracted from the digitized images using in-house developed software. The image is displayed on the computer screen and objects in the image are picked with the mouse. Three registration marks located on one of the glass windows of the wind tunnel test section are used to establish the orientation of the coordinate axes, the scale factor of the image in pixels per physical units, and the location of the rotation axis (the quarter-chord point) of the airfoil. The user picks the screen location of the three registration marks and an airfoil outline is overlaid on the image. The outline can be manually repositioned and/or re-sized to provide the best fit to the image (see Fig. 9).

To obtain the surface pressure distribution the user picks the point were each fringe meets the airfoil surface - recall that the interference fringes represent lines of constant fluid density. The program projects the pick points to the surface of the airfoil. Given the fringe number of the stagnation fringe, the other fringes are automatically numbered. Local fluid density and pressure coefficient are calculated from fringe number according to the parameters of the optical system and the isentropic flow relations, respectively[8,9]. For global pressure field data, the user picks several points along the center line of a fringe and a cubic spline curve fit is performed. The density and pressure coefficient are calculated for the fringe and 100 coordinate points from the spline-fit are saved per fringe. The complete fringe map can then be color coded by pressure coefficient value (see Fig. 10). This tool is invaluable for determining how small changes to the airfoil surface affect the global properties of the flow. A new feature to the analysis program allows the user to magnify a portion of the image. Pick operations can be performed on either the original image or the magnified image. For data obtained at $M \geq 0.3$ the fringe spacing at the leading edge is only a few pixels, and magnifying this portion of the image is generally necessary.

The analysis program described in the preceding paragraph is tedious; requiring approximately ten minutes per surface pressure distribution and forty minutes per global pressure field. Since interferometry images are obtained in such abundance, and to help eliminate any possible operator bias from the analysis of the images, an automatic fringe analysis technique is being sought.

The main complication in developing an algorithm for detecting fringes is the complexity of the fringe pattern itself. The spacing, thickness and direction of the fringes vary greatly across an image. Furthermore, the illumination and contrast are not always uniform across an image, especially near the surface of the airfoil. This is illustrated in Fig. 11, which shows an enlarged portion of a typical interferogram after digitization, as well as the intensity profile of two rows of pixels across the image. The intensity profiles

are normalized and plotted about the half intensity value.

Many automatic fringe analysis techniques operate on a binary image[14-17]. A binary image is formed by making white all pixels having an intensity greater than a chosen threshold, and making all other pixels black. Figure 12 is the binary image of the image in Fig. 11. The fringe edges are very distinct and can be easily extracted by calculating the magnitude of the intensity gradient at each pixel. Two-point finite difference operators were applied to Fig. 12 and the resulting edge map is shown in Fig. 13. This method is highly dependent on the choice of the threshold level when forming the binary image. As is clearly seen in the second intensity profile of Fig. 11, there are light fringes with peak intensities nearly as low as some dark fringes in the outer flow, and consequently these fringes are lost in the binary image (Fig. 12). An adaptive technique which determines the optimum threshold for each sub-region of the image could improve this method.

Another technique, called thinning[18], operates on the binary image to locate the fringe centerlines. The thinning process systematically removes pixels from the border of an object (here, the black fringes). Thinning is performed iteratively until only the 'skeleton' of the object remains. The result of thinning the binary image in Fig. 12 is shown in Fig. 14. The 'tributaries' branching off the main fringe lines arise from irregularities present in the initial fringe edges. These irregularities can be smoothed by filtering the image prior to forming the binary image, however, great care must be taken not to filter out valid information in the high-frequency fringe regions and the low-contrast regions of the image.

Approaches which do not rely on having a binary image are presently being investigated, and include directional filtering[19] and zero crossing detection[20].

IV. Summary and Conclusions

An airfoil having a dynamically adaptive leading-edge profile is proposed as a unique device for the active control of unsteady separated flow. A carbon-fiber composite skin has been constructed for use as the adaptive-geometry airfoil surface. The skin was bench tested and shown to deform in a reliable, repeatable fashion. A wind tunnel test model is in the final stage of construction.

A high-speed phase-locked photographic data acquisition system was developed for recording interferometry images at rates up to 40,000 images/sec. The system will be used to record the instantaneous interactions between the deforming surface of the adaptive-geometry airfoil and the flow field around the airfoil. Encouraging progress has been made toward automating the image analysis process.

A series of baseline dynamic stall experiments were performed, and the issue of transition effects on dynamic stall was examined. Results show that achieving Reynolds number similarity by tripping the boundary layer is not straight-forward in the case of dynamic-stall flow. The large adverse pressure gradients encountered near the suction peak together with the highly unsteady nature of the flow field place exacting demands on the size of the trip (see Appendix C).

Acknowledgements

This project was supported. through the NASA co-operative agreement no. NCC2-637. by funds from the Navy-NASA Joint Institute of Aeronautics, the U. S. Air Force

Office of Scientific Research, and the U. S. Army Research Office. The guidance of Dr. M. S. Chandrasekhara, Associate Director of the Navy-NASA Joint Institute of Aeronautics, and Dr. L. W. Carr, U. S. Army ATCOM, is acknowledged. The work was performed in the Fluid Mechanics Branch of NASA Ames Research Center. The support of Dr. S. S. Davis, Chief, FML Branch is appreciated. The manual image analysis software was developed by Mr. P. J. Trosin of Sterling Federal Systems, Inc., and modified by Mrs. S. Nado of Foothills College and by the author. The electronics for the high-speed camera system were designed by Mr. D. Squires of Sverdrup Technology, Inc. The support of Mr. J. Loomis in conducting the experiments is acknowledged.

References

[1] Chandrasekhara, M.S. and Carr, L.W., "Flow Visualization Studies of the Mach Number Effects on the Dynamic Stall of an Oscillating Airfoil", *Journal of Aircraft*, Vol. 27, No. 6, pp. 516-522.

[2] Carr, L.W., McCroskey, W.J., McAlister, K.W., Pucci, S.L., and Lambert, O., "An Experimental Study of Dynamic Stall on Advanced Airfoil Sections Volume 3. Hot-Wire and Hot-Film Measurements", *NASA-TM-84245*, Dec. 1982.

[3] Wu, J. Z., Vakili, A. D., and Wu, J. M., "Review of the Physics of Enhancing Vortex Lift by Unsteady Excitation", *Prog. Aerospace Sci.*, Vol. 28, 1991, pp. 73-131.

[4] Rossi, M. J., Austin, F., and VanNostrand, W., "Active Rib Experiment for Shape Control of an Adaptive Wing", AIAA Paper 93-1700, 1993.

[5] Tsukamoto, H., Tanaka, K., Matsunaga, S., and Tanaka, H., "Development of a Shape-Controlled Airfoil by Use of SMA", *Japan Society of Mechanical Engineers, Transactions B*, Aug. 1992, pp. 169-173.

[6] Carr, L.W., and Chandrasekhara, M.S., "Design and Development of a Compressible Dynamic Stall Facility", *Journal of Aircraft*, Vol. 29, No. 3, pp. 314-318.

[7] Chandrasekhara M.S., and Carr, L.W., "Design and Development of a Facility for Compressible Dynamic Stall Studies of a Rapidly Pitching Airfoil", *ICIASF'89 RECORD*, IEEE Publication 89-CH2762-3, pp. 29-37.

[8] Carr, L.W., Chandrasekhara, M.S., Ahmed, S., and Brock, N.J., "A Study of Dynamic Stall Using Real Time Interferometry", *AIAA Paper 91-0007*.

[9] Brock, N.J., Chandrasekhara, M.S., and Carr, L.W., "A Real Time Interferometry System for Unsteady Flow Measurements", *The 14th ICIASF Conference*, Rockville, MD, Oct. 1991.

[10] Beard, J., "Plastic Ribbon Shakes the Ice off Aircraft", *New Scientist*, May 12, 1990, p. 36.

[11] Wilder, M. C., "Control of Unsteady Separated Flow Associated With the Dynamic Stall of Airfoils", *NASA-CR-190688*, August, 1992.

[12] Pope, A., and Goin, K.L., *High Speed Wind Tunnel Testing*. Kraeger Publishing Company, New York, NY, 1978.

[13] Chandrasekhara, M. S., Squires, D. D., Wilder, M. C., and Carr, L. W., "A Phase-Locked High-Speed Real-Time Interferometry System for Large Amplitude Unsteady Flows", 7th International Symposium on Applications of Laser Techniques to Fluid Mechanics, Lisbon, Portugal, July, 1994.

[14] Yu, Q., "Spin Filtering Processes and Automatic Extraction of Fringe Centerlines in Digital Interferometric Patterns". *Applied Optics*, Vol. 27, No. 18, 15 Sep. 1988, pp. 3782-3784.

[15] Hunter, J.C., Collins, M.W., and Tozer, B.A., "An Assessment of Some Image Enhancement Routines for use with an Automatic Fringe Tracking Programme", *Fringe Pattern Analysis, SPIE Vol. 1163*, 1989, pp. 83-94.

[16] Nubel, R., "Computer-aided Evaluation Method for Interferograms". *Experiments in Fluids*, No. 12, 1992, pp. 166-172.

[17] Bartels-Lehnhoff, H.-H., Baumann, P.H., Bretthauer, B., and Meier, G.E.A., "Computer Aided Evaluation of Interferograms", *Experiments in Fluids*, No. 16, 1993, pp. 46-53.

[18] Gonzalez, R.C., and Woods, R.E., *Digital Image Processing*, Addison-Wesley Publishing Company, June 1992.

[19] Khorsandi, S. and Venetsanopoulus, A.N., "Hierarchical Fuzzy Approach for Fingerprint Processing", *Nonlinear Image Processing IV, SPIE Vol. 1902*, 1993, pp. 224-234.

[20] Gasvik, K.J., Robbersmyr, K.G., and Vadseth, T., "Fringe Location by Means of a Zero Crossing Algorithm", *Fringe Pattern Analysis, SPIE Vol. 1163*, 1989, pp. 64-70.

Table 3a: Conditions for Trip #1. Transiently Pitching Airfoil

M	α^+					
	0	0.02	0.025	0.03	0.035	0.04
0.20	X		X	X		X
0.30	X	X	X	X	X	X
0.45	X	X	X	X		

Table 3b: Conditions for Trip #1, Oscillating Airfoil

M	k				
	0	0.025	0.05	0.075	0.1
0.20			X	X	
0.30		X	X	X	X
0.45		X	X		

Table 3c: Conditions for Trip #2, Oscillating Airfoil

M	k				
	0	0.025	0.05	0.075	0.1
0.20	X		X		X
0.30	X		X		X
0.45	X		X		

Table 3d: Conditions for Trip #3, Oscillating Airfoil

M	k				
	0	0.025	0.05	0.075	0.1
0.20	X		X		X
0.30	X		X		X
0.45	X		X		

Table 3e: Conditions for Trip #4, Oscillating Airfoil

M	k				
	0	0.025	0.05	0.075	0.1
0.30	X		X		X
0.45	X		X		

Table 3f: Conditions for Trip #5, Oscillating Airfoil

M	k				
	0	0.025	0.05	0.075	0.1
0.30	X		X		
0.45	X		X		

Table 4a: Conditions for Oscillating Airfoil Leading-Edge Studies

M	k				
	0	0.025	0.05	0.075	0.1
0.20			X	X	X
0.25			X	X	X
0.30	X	X	X	X	X
0.35		X	X	X	
0.40		X	X	X	
0.45		X	X	X	

Table 4b: Conditions for Oscillating Airfoil Global Flow-Field Studies

M	k					
	0	0.025	0.05	0.075	0.1	0.15
0.20	X		X	X	X	X
0.30	X	X	X	X	X	
0.40	X	X	X	X	X	
0.45	X	X	X	X		

Note: each X represents between 25 and 50 interferograms.

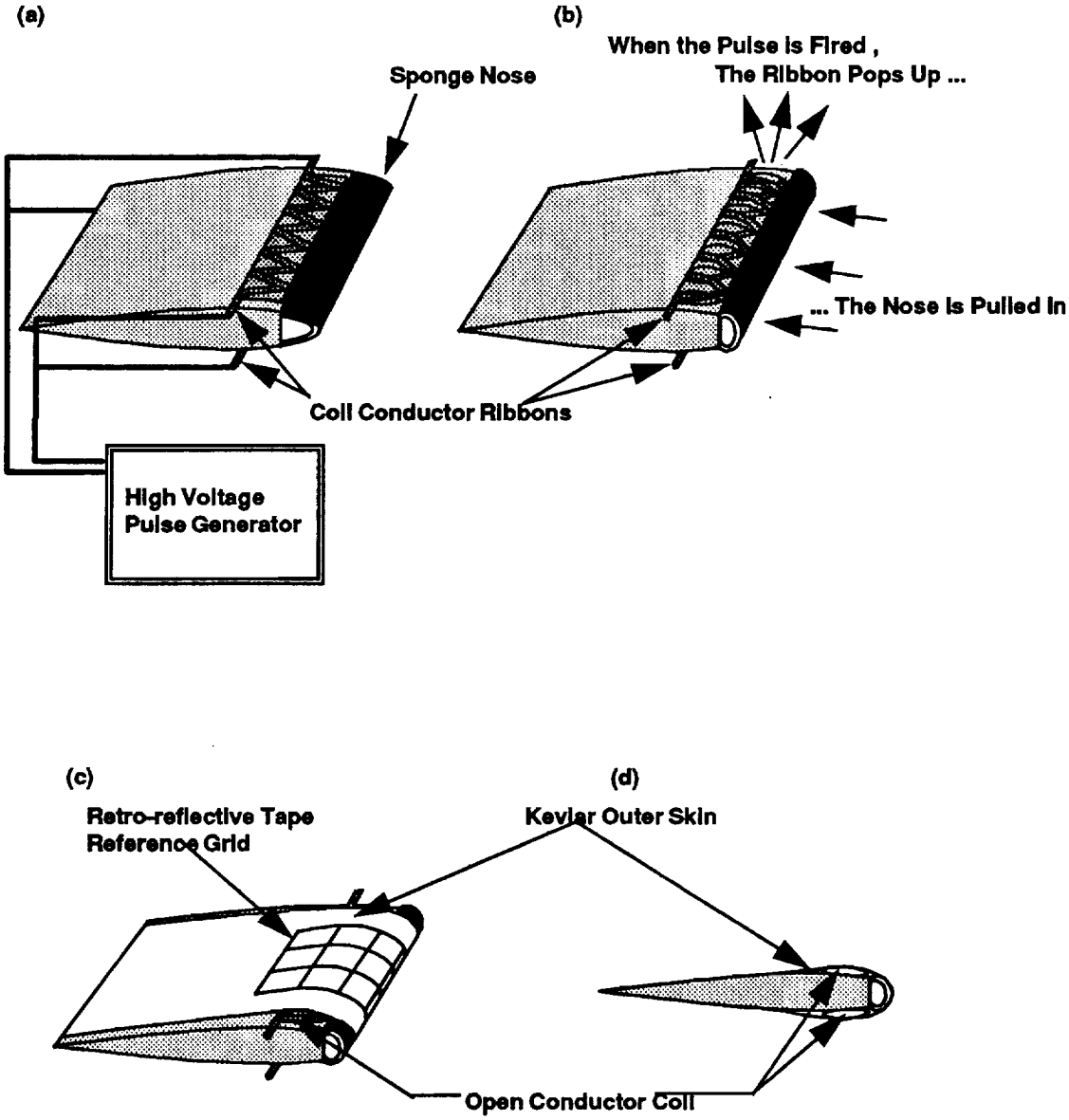

Fig. 1. Schematic of the Electro-Repulsive Leading-Edge Device as installed on the Sponge-Nose Model: (a) The Neutral State, (b) The Activated State, (c) Shown with Kevlar Outer Skin and Reference Grid, (d) Side View.

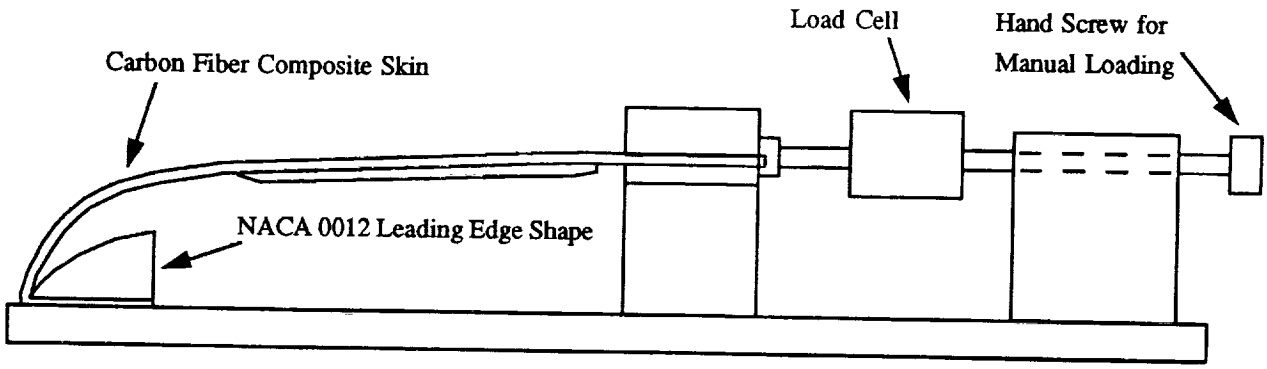

Fig. 2. Sketch of Composite–Skin Bench –Test Fixture: Side View, Not to Scale.

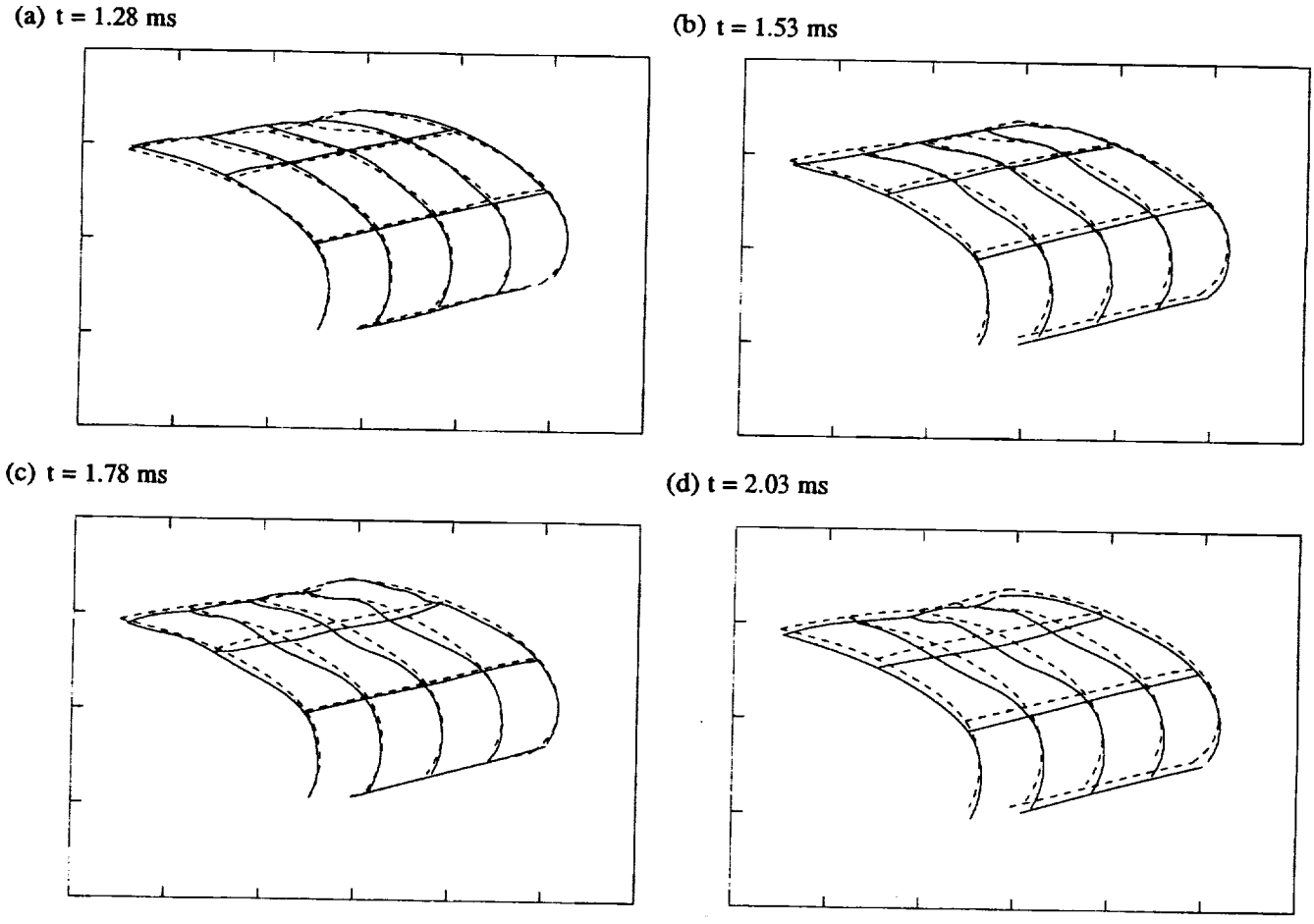

Fig. 3. Sequence of Surface Shape Profiles Obtained with the First Electro–Repulsive Surface: Perspective View. Time Measured from Initiation of High–Voltage Pulse.
— — — Reference surface, ——— Instantaneous Surface, 1in x 1in Surface Grid Cells.

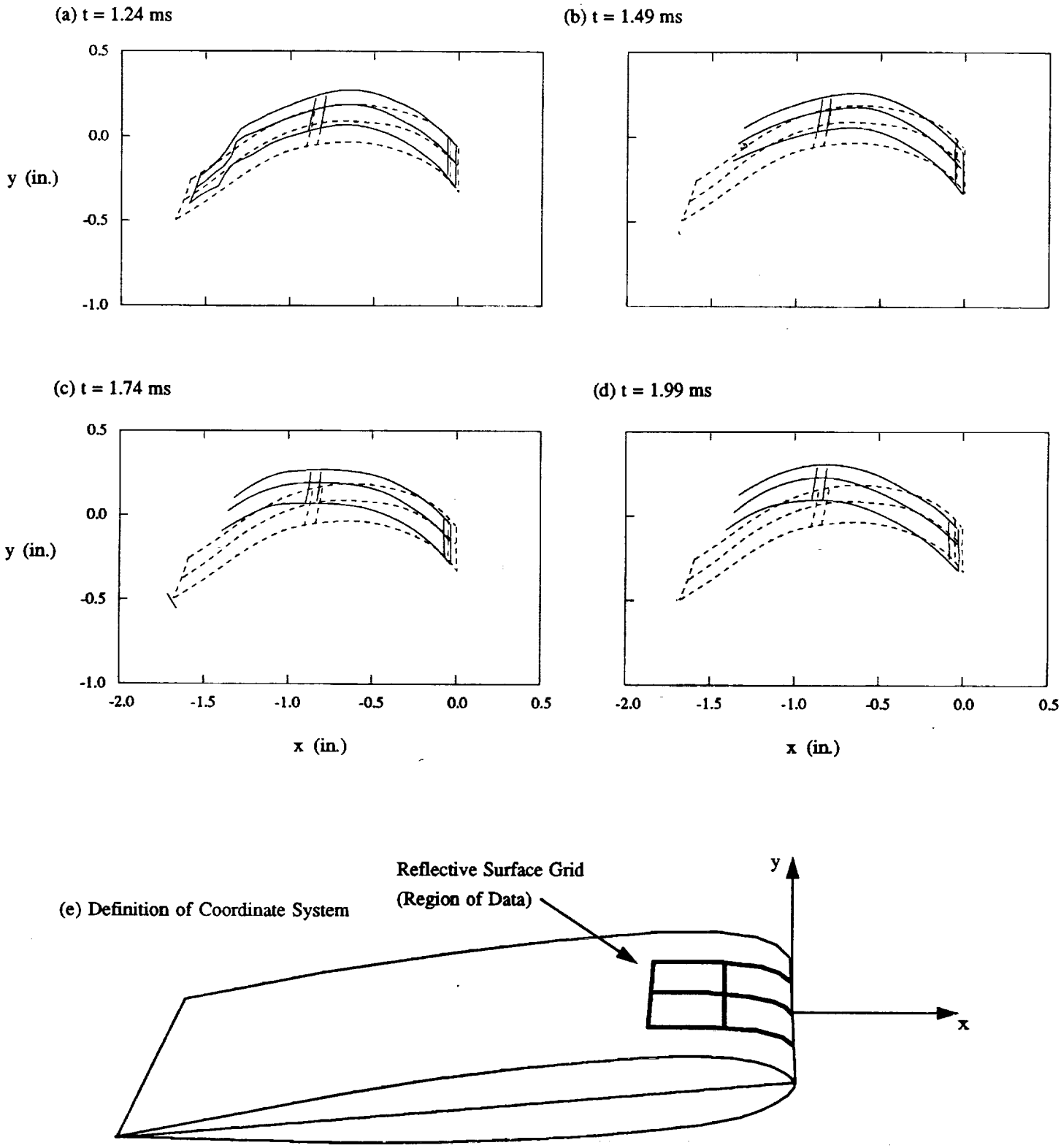

Fig. 4. Sequence of Surface Shape Profiles Obtained with the Third Electro-Repulsive Surface: Persective View of Leading Edge. Time Measured from Initiation of High-Voltage Pulse.
— — — Reference surface, ——— Instantaneous Surface, 1in x 1in Surface Grid Cells.

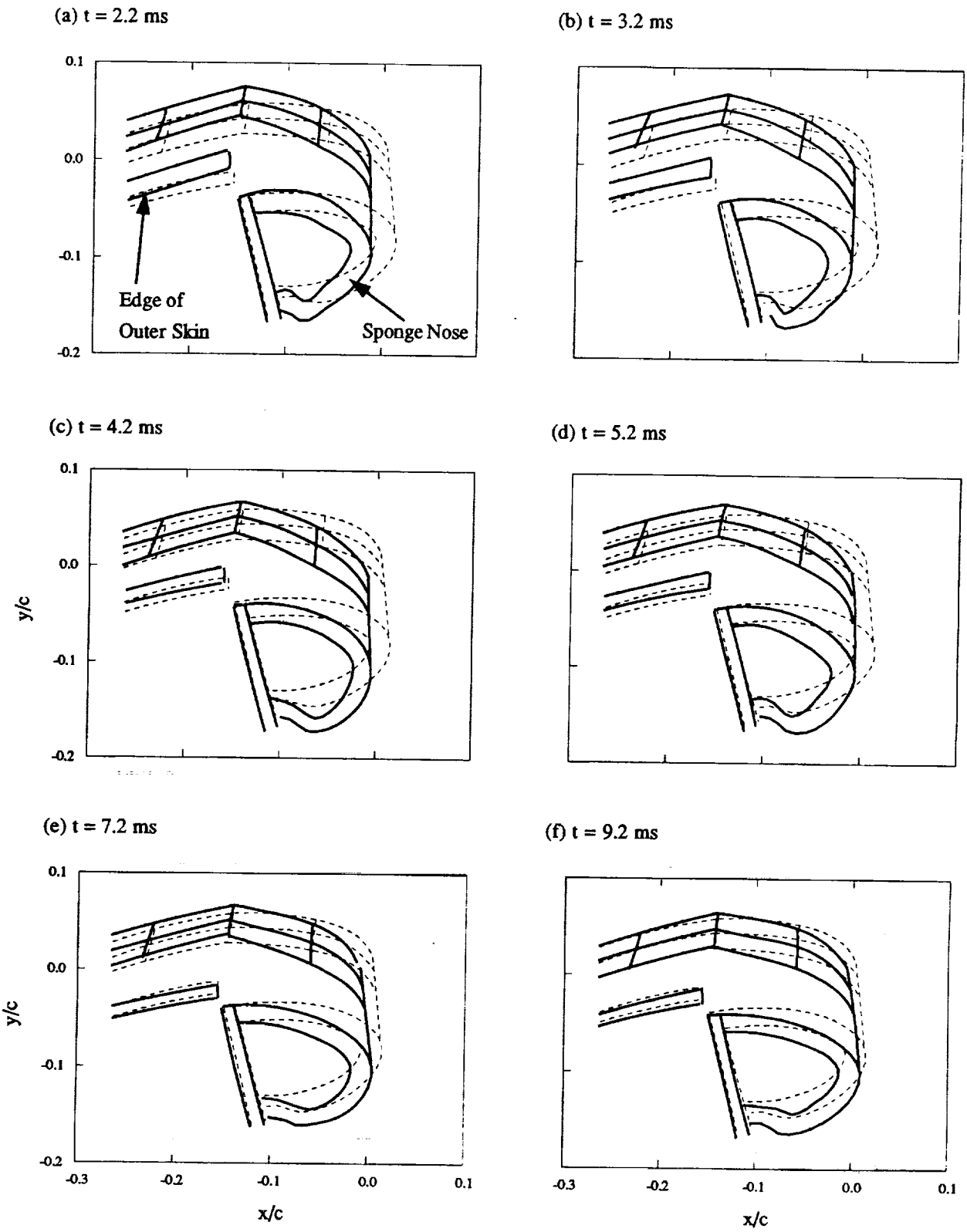

Fig. 5. Sequence of Surface Shape Profiles Obtained with the Solid Sponge Nose Airfoil: Perspective View. Time Measured from Initiation of High-Voltage Pulse. See Fig. 1 for Location of Grid on Airfoil Surface. — — — Reference surface, ———— Instantaneous Surface.

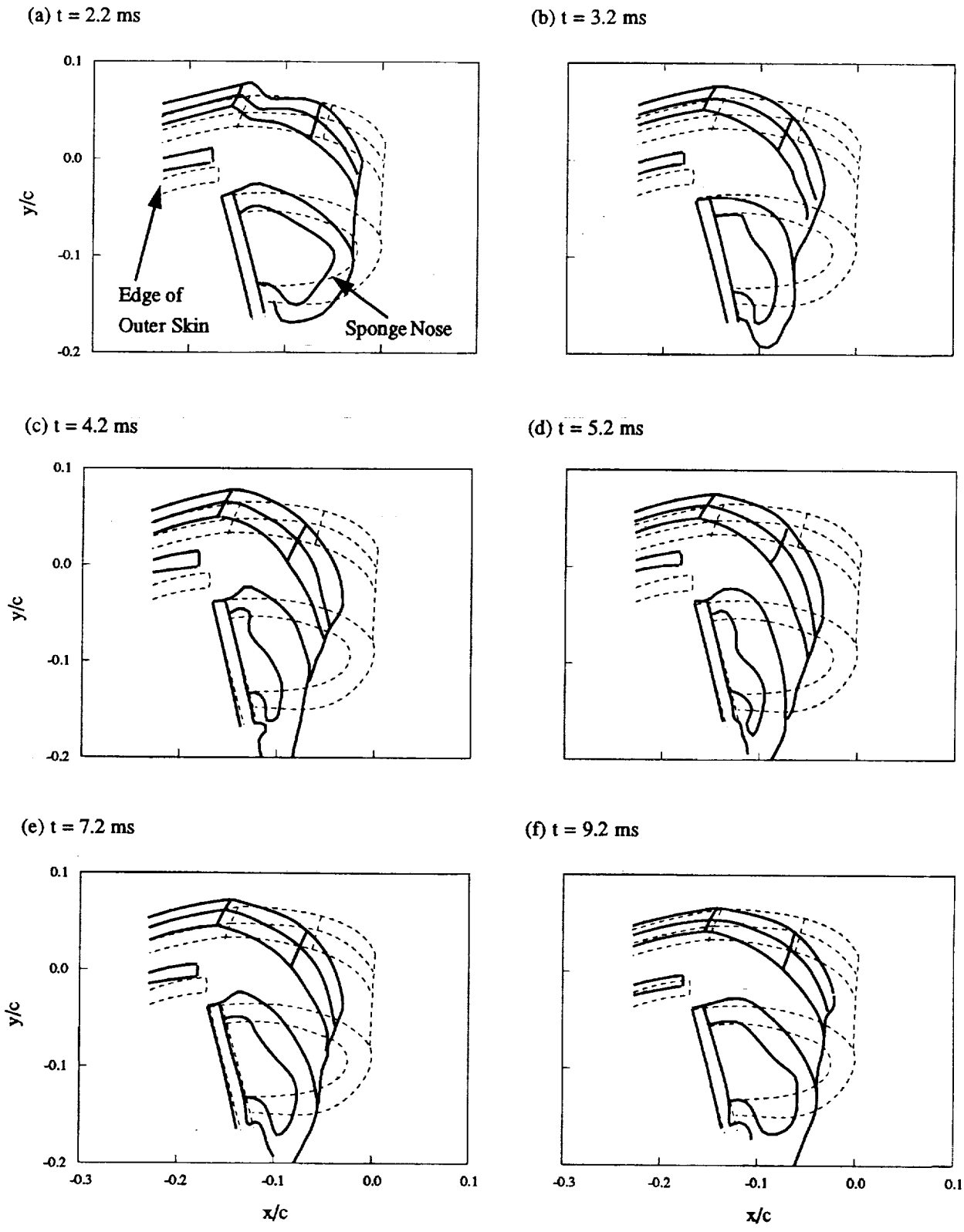

Fig. 6. Sequence of Surface Shape Profiles Obtained with the Hollow Sponge Nose Airfoil: Perspective View. Time Measured from Initiation of High–Voltage Pulse. See Fig. 1 for Location of Grid on Airfoil Surface.
— — — Reference surface, ———— Instantaneous Surface.

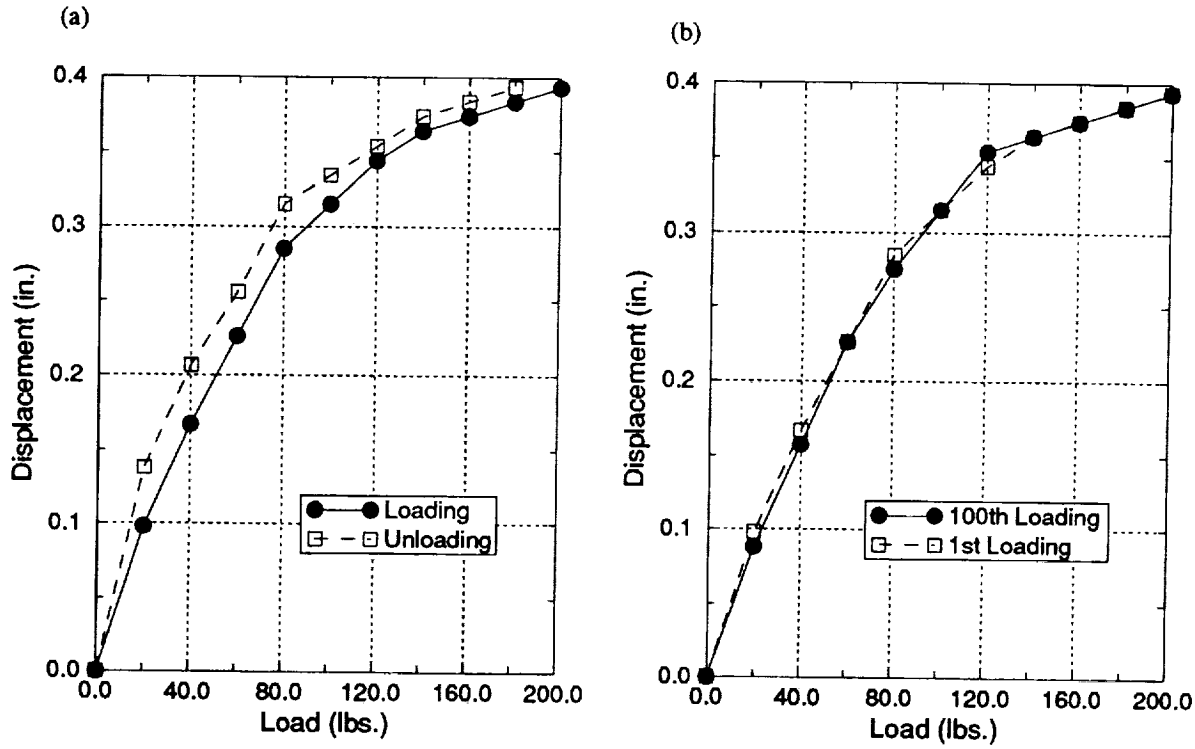

Fig. 7. Displacement of Composite Skin vs. Applied Load: (a) Loading/Unloading Cycle, (b) First and 100th Loading Cycles.

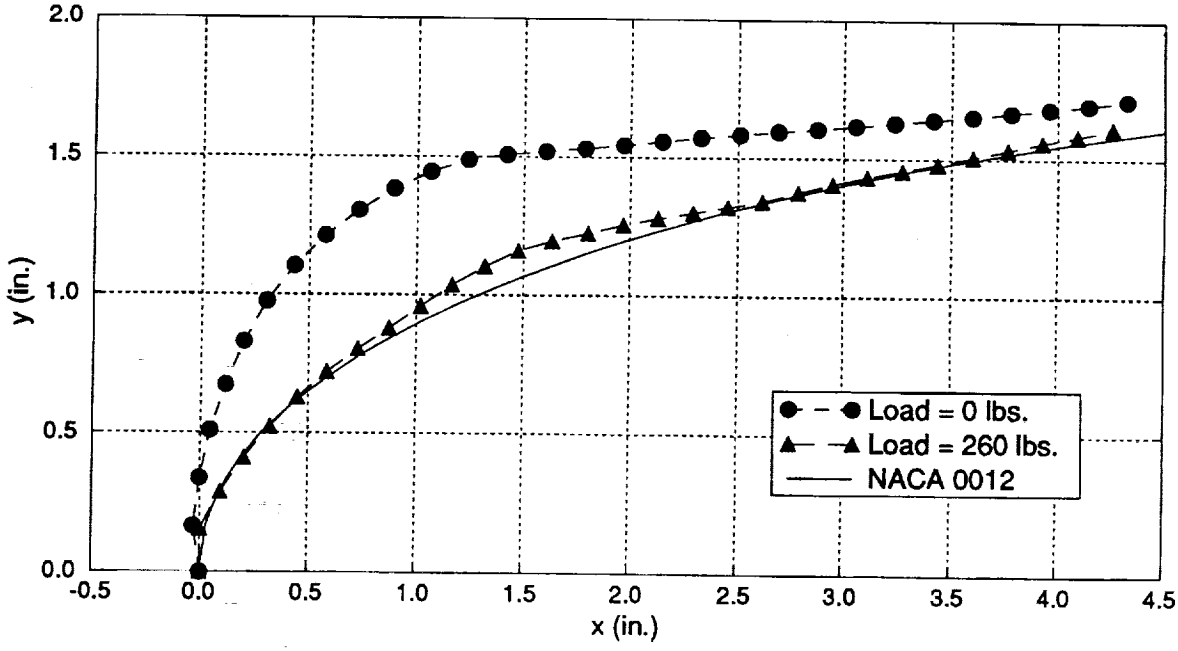

Fig. 8. Surface Profile of Composite Skin Model for Unloaded and Loaded Conditions. Solid Line is NACA 0012 Reference Profile.

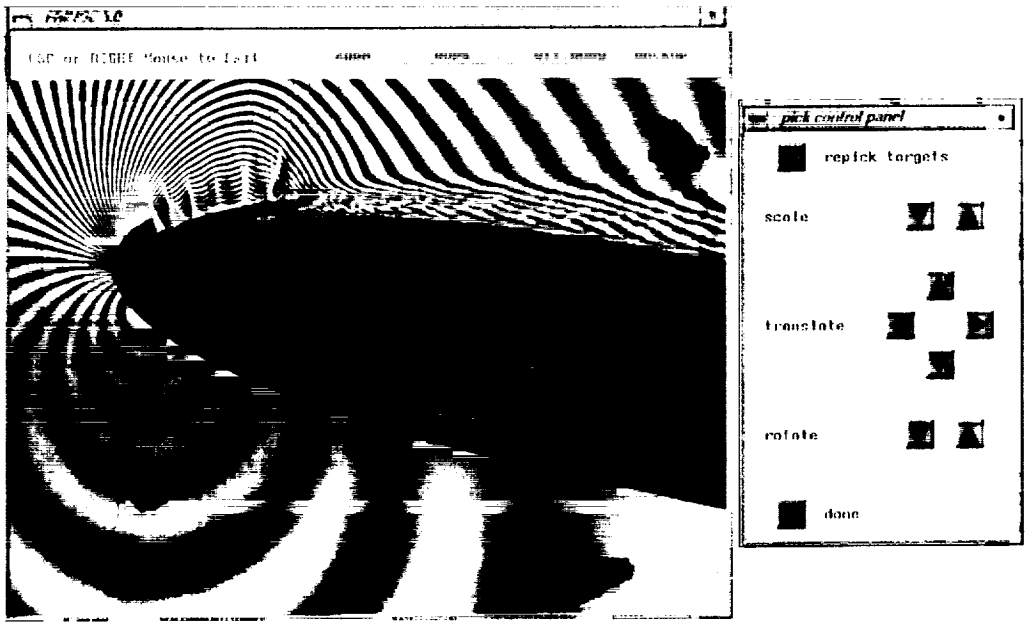

Fig. 9. Fringe Analysis Software: Airfoil Overlay/Coordinate System Definition

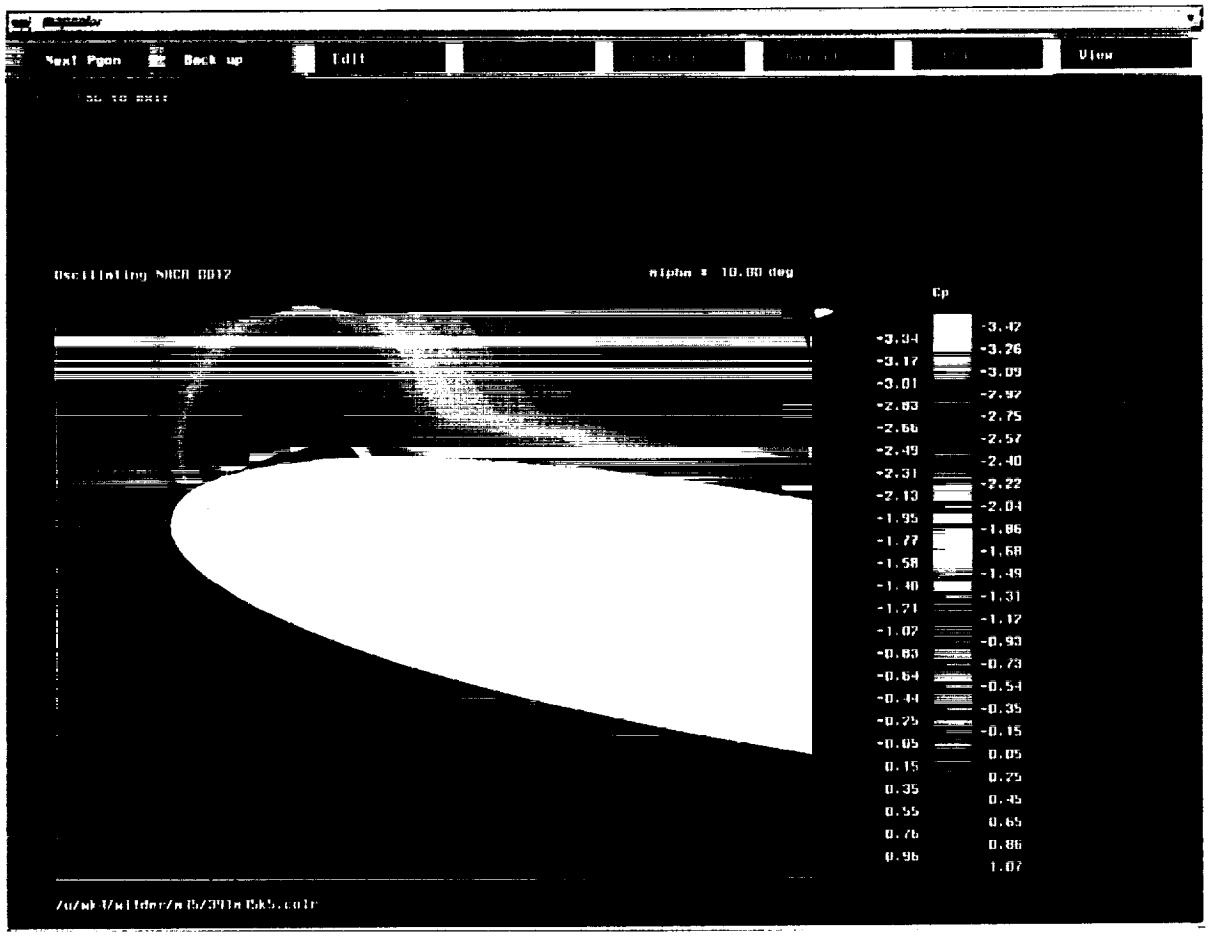

Fig. 10. Fringe Analysis Software: False-Color Pressure Field Obtained from Fig. 9 Image.

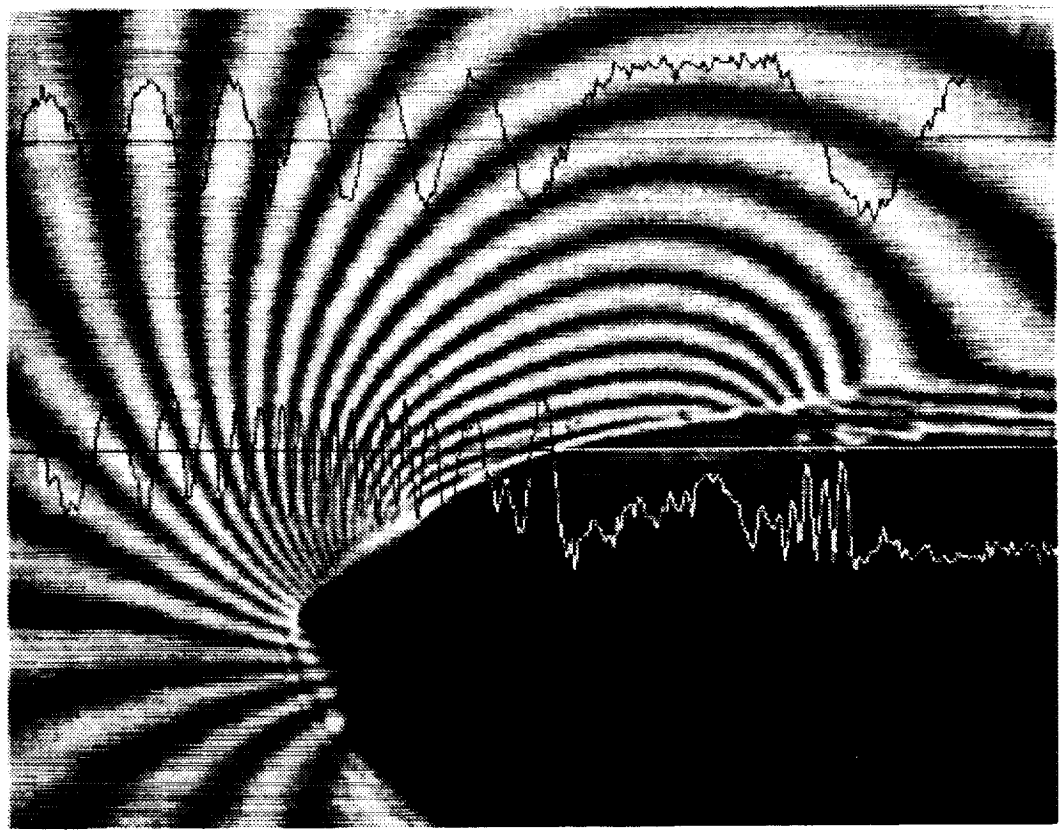

Fig. 11. PDI Image Near Leading-Edge of an Oscillating NACA 0012 Airfoil Showing the Intensity Profiles Along Two Rows of Pixels.

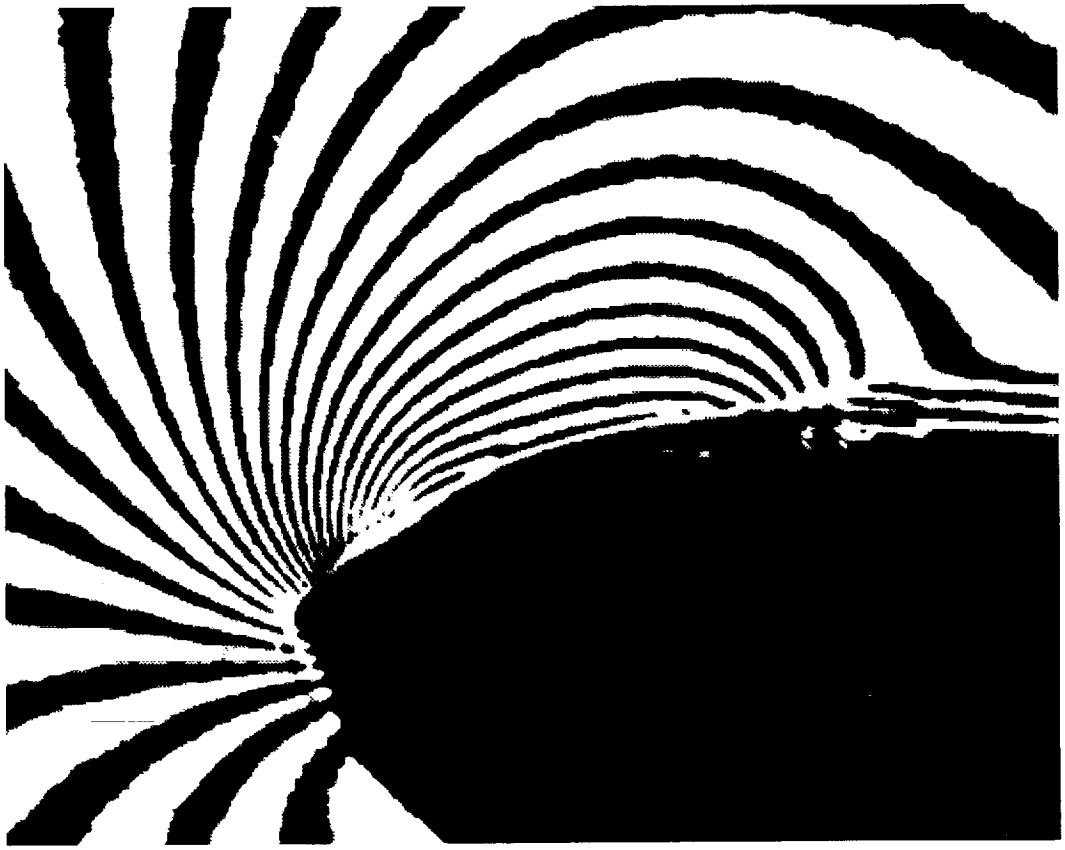

Fig. 12. Binary Image of Image in Fig. 11 Using a Threshold Intensity of 170.

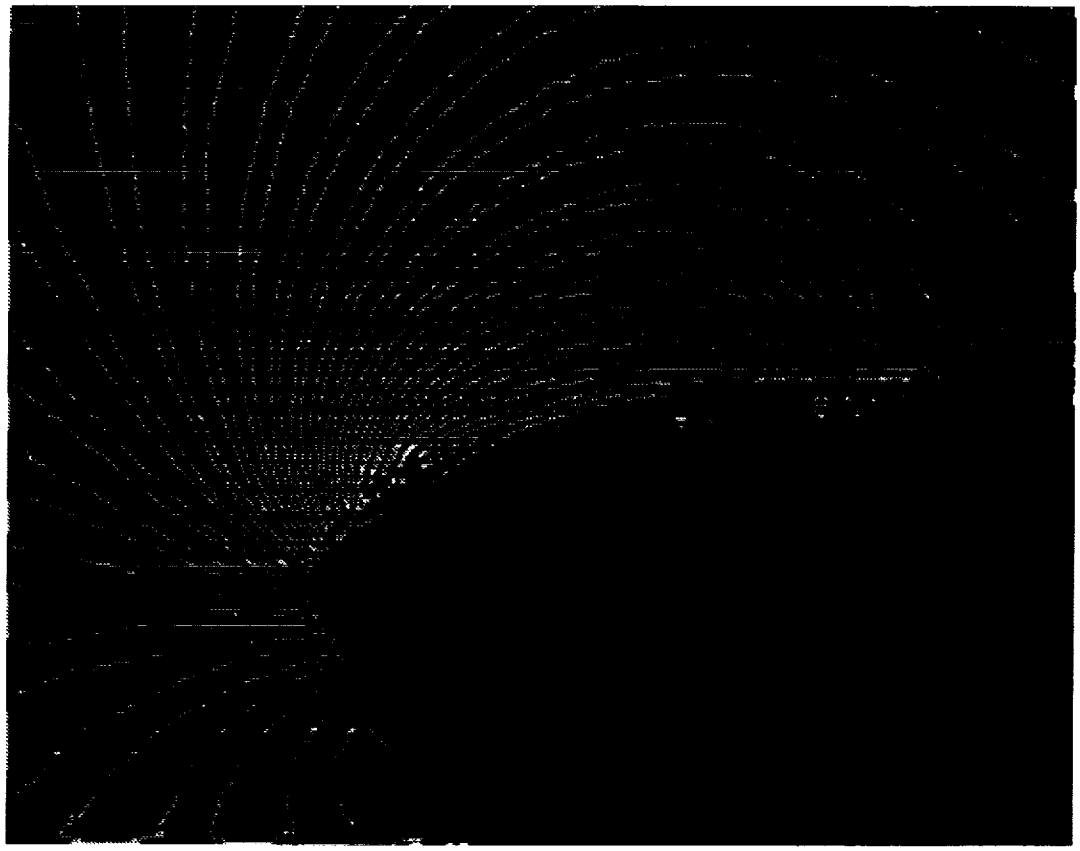

Fig. 13. Edge Detection by Gradient Operator Applied to Binary Image (Fig. 11).

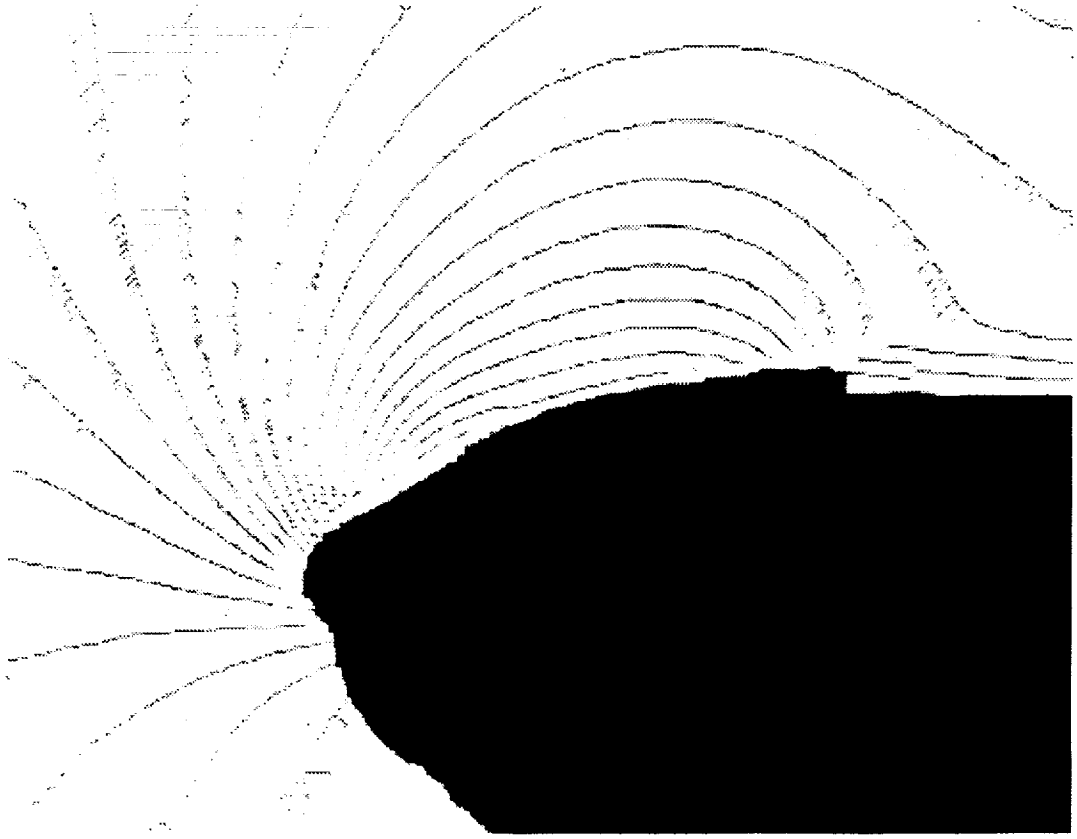

Fig. 14 Centerline Detection by Thinning Applied to Binary Image (Fig. 11).

Appendix A:

Interferometric Investigations of Compressible Dynamic Stall over a Transiently Pitching Airfoil

Interferometric Investigations of Compressible Dynamic Stall over a Transiently Pitching Airfoil

M. S. Chandrasekhara, L. W. Carr, M. C. Wilder

Reprinted from

AIAA Journal

Volume 32, Number 3, Pages 586–593

AIAA

A publication of the
American Institute of Aeronautics and Astronautics, Inc.
370 L'Enfant Promenade, SW
Washington, DC 20024-2518

AIAA JOURNAL
Vol. 32, No. 3, March 1994

Interferometric Investigations of Compressible Dynamic Stall over a Transiently Pitching Airfoil

M. S. Chandrasekhara*
Naval Postgraduate School, Monterey, California 93943
L. W. Carr†
NASA Ames Research Center, Moffett Field, California 94035
and
M. C. Wilder‡
MCAT Institute, San Jose, California 95127

The compressible dynamic stall flowfield over a NACA 0012 airfoil transiently pitching from 0 to 60 deg at a constant rate under compressible flow conditions has been studied using real-time interferometry. A quantitative description of the overall flowfield, including the finer details of dynamic stall vortex formation, growth, and the concomitant changes in the airfoil pressure distribution, has been provided by analyzing the interferograms. For Mach numbers above 0.4, small multiple shocks appear near the leading edge and are present through the initial stages of dynamic stall. Dynamic stall was found to occur coincidentally with the bursting of the separation bubble over the airfoil. Compressibility was found to confine the dynamic stall vortical structure closer to the airfoil surface. The measurements show that the peak suction pressure coefficient drops with increasing freestream Mach number, and also it lags the steady flow values at any given angle of attack. As the dynamic stall vortex is shed, an anti-clockwise vortex is induced near the trailing edge, which actively interacts with the post-stall flow.

Nomenclature

C_p = pressure coefficient
c = airfoil chord
M = free stream Mach number
Re = Reynolds number based on c and U_∞
U_∞ = freestream velocity
x,y = chordwise and vertical distance
α = angle of attack
$\dot{\alpha}$ = pitch rate, in deg/s
α^+ = nondimensional pitch rate, $\dot{\alpha}c/U_\infty$
γ = ratio of specific heats
ϵ = fringe number
ρ = density
ρ_0 = density at reference (atmospheric) conditions

I. Introduction

THE utilization of dynamic stall as a method for increasing the maneuverability and agility of aircraft has received significant attention during the past few years. Several researchers[1-6] have studied the flow over pitching airfoils using flow visualization and unsteady pressure measurements and have provided valuable information on the dynamic stall phenomenon. However, all of these studies were at low speeds. Lorber and Carta[7] have obtained measurements under compressibility conditions that showed that at higher Mach numbers the flow could not develop the suction levels observed under incompressible conditions and noted that this effectively limited the stall delay that could be achieved. The computational studies of Visbal[8] lend some support to this result. Since compressibility effects have been shown[9,10] to change the way that dynamic stall develops, a better understanding of these effects has been of interest in the development of supermaneuverable aircraft and highly agile helicopters. It is well known[9] that the effects of compressibility set in at very low freestream Mach numbers (M = 0.2–0.3) on airfoils operating at high-lift levels due to the development of extremely strong suction peaks near the leading edge, which cause acceleration of the local flow to supersonic speed. The fact that dynamic lift still persists even when compressibility effects appear[10] supports the argument that the benefits of dynamic stall can be exploited in flight systems. However, for these attempts to be successful, a better understanding of the effects of compressibility on the developing unsteady flow is needed.

Most of the events of dynamic stall onset are concentrated near the leading-edge region of an airfoil or wing executing unsteady pitch-up motion. These include occurrence of strong suction pressures, rapid movement of the stagnation point, transition of the boundary layer, possible formation of a separation bubble, production of shocks (which can interact with the boundary layer and cause separation), generation of large amounts of coherent vorticity (which becomes the dynamic stall vortex/vorticity), and initial movement of the dynamic stall vortex over the airfoil. In contrast to dynamic stall onset, the later stages of dynamic stall development require knowledge about the flow away from the surface of the airfoil. Global characteristics of the flow are needed to understand the interactions that occur as the vortex moves down the airfoil. As it moves past the trailing edge, additional events such as generation of a trailing-edge vortex, redistribution of the flowfield over the airfoil, etc., occur that need to be documented if the dynamic flow is to be controlled and utilized.

Experiments focused on these issues are ongoing in the Compressible Dynamic Stall Facility (CDSF) at the Fluid Mechanics Laboratory (FML) of NASA Ames Research Center. The primary goal of the research is to improve the understanding of these complex fluid interactions. It is also aimed at

Presented as Paper 93-0211 at the AIAA 31st Aerospace Sciences Meeting, Reno, NV, Jan. 11-14, 1993; received Feb. 9, 1993; revision received Aug. 11, 1993; accepted for publication Aug. 16, 1993.

*Associate Director and Research Associate Professor, Department of Aeronautics and Astronautics, Navy-NASA Joint Institute of Aeronautics, M.S. 260-1, NASA Ames Research Center, Moffett Field, CA 94035-1000. Associate Fellow AIAA.

†Research Scientist and Group Leader, Unsteady Viscous Flows, Aeroflightdynamics Directorate, U.S. Army ATCOM and Fluid Mechanics Laboratory Branch. Member AIAA.

‡Research Scientist.

obtaining quality experimental data to serve as a benchmark for computational studies. A simple real-time technique known as point diffraction interferometry (PDI), which was developed recently and does not have the limitations of standard interferometry methods, has been used to document the flow over an airfoil transiently pitching at a constant rate. A large number of flow interferograms have been obtained and processed to determine the pressure field to assess the role of unsteadiness in achieving stall delay and sustaining dynamic lift. Some of the results of this effort are reported in the present paper.

II. Description of the Facility, Instrumentation, and Experimental Technique

A. Facility

The CDSF is a unique experimental facility of the Navy-NASA Joint Institute of Aeronautics and is operated as part of the in-draft tunnel complex at the FML (for details see Carr and Chandrasekhara[11]). The airfoil is supported in the CDSF between two 2.54-cm-thick optical quality glass windows by small pins, permitting optical access to the complete flowfield. Thus, details of the flow at the surface near the leading edge, where the dynamic stall vortex forms, as well as the flowfield away from the airfoil can be captured.

The transient pitching motion is produced by a feedback controlled, programmable hydraulic drive system. The airfoil is pitched from 0 to 60 deg at rates of up to 3600 deg/s. To limit or isolate the effects of transients on separation, the change in angle of attack during acceleration and the time of acceleration were limited to less than 6 deg and 4 ms, respectively. The system uses both the airfoil position and velocity information in its feedback loops to properly perform the programmed maneuver. The complete details of the design are presented in Chandrasekhara and Carr.[12] The highest pitch rate used in the experiment (on a 7.62-cm-chord airfoil) corresponds to a 90 deg/s pitch rate of a 3-m-chord airplane wing at any given Mach number; thus, the rates obtainable from the study are applicable to flight conditions. It is worth pointing out that this scaling does not fully simulate the boundary-layer scales such as transition and its role on flow separation.

B. Instrumentation

The airfoil position was read by a digital optical encoder, whose output was input to the digital I/O board of a microVAX II workstation and timed with its internal clock. The data obtained showed that the airfoil angle of attack increased at a linear rate as it passed through the static stall angle. At the highest rate, the motion was completed in 18 ms.

The nondimensional pitch rates used are based on the total time for pitching from 0 to 57 deg. However, the hydraulic control system caused the airfoil to pitch 5–8% faster in the 0–10-deg range and sometimes in the 0–30-deg range. This difference is not believed to significantly affect the global results of the study.

C. Point Diffraction Interferometry Technique

The technique used in the study was point diffraction interferometry, which utilizes the ability of a point discontinuity (a pinhole) located at the image of a point source to diffract a portion of the incident light into a spherical reference wave front. In the present application, the primary optics of an existing schlieren system[13] were used with a pulsed Nd:YAG laser as the light source. The laser light was expanded through a microscope objective to fill the schlieren mirror, transmitted through the test section, and refocused by another schlieren mirror. An exposed photographic plate was placed at the focus of this second mirror (replacing the knife edge), and with no flow in the tunnel, the laser was pulsed with enough energy to burn a hole, or spot, in-situ in the emulsion located at the focal plane of the second mirror. The spot was precisely tailored to the application under investigation, automatically correcting for nonuniformities in the light source or optics. With the flow turned on, the laser was triggered externally at the desired angles of attack, and the real-time interference fringes were recorded on ASA 3000 Polaroid film. Further details about the PDI technique can be found in Refs. 13 and 14.

D. Interferogram Image Processing

Digitized (256 gray levels) interferograms were processed semi-automatically on an IRIS workstation to recover the pressure distributions using a specially developed software package. An airfoil was overlayed on the digitized image using the triangular registration markers seen in the photographs. The intersections of the fringes with the airfoil upper and lower surfaces (or the local boundary-layer edge, when detectable) were interactively picked by the user. The density along any fringe was calculated from the Gladstone-Dale equation,[15] which for the present wind tunnel and laser simplifies to

$$\rho - \rho_0 = 0.009421\epsilon$$

As usual, bright fringes have integer values and dark fringes are numbered as half-integers. Fringes from the freestream to the stagnation point have positive values. The corresponding pressure along a fringe, including that at the boundary-layer edge, was derived using isentropic flow relations as

$$C_p = \frac{[(\rho/\rho_0)^\gamma - 1]}{[(\gamma/2)M^2]}$$

This pressure at the edge of the boundary layer was used as the surface pressure invoking the boundary-layer assumptions. Typical processing time was about 3–5 min per image.

In cases where the fringe density was high or the fringes were fuzzy, the user could go into the "off-body" mode and pick fringes along a line parallel to and away from the airfoil surface where the fringes are farther apart. For this purpose, an option to superimpose two larger airfoils over the image on the screen was provided in the software. The fringe intersections on the larger airfoils were then suitably projected onto the actual airfoil surface. At angles of attack near the dynamic stall angle, the fringes near the leading-edge region were very dense, reflecting the large local density gradients. Further, in this region, optical noise introduced by the shadowgraph effect generally lowered the contrast, making it a location where the off-body mode needed to be invoked.

In the present study the entropy change in the vortical flow was ignored (for lack of a better method). Interferograms with shocks have not been processed because of this limitation.

E. Experimental Conditions

Several hundred interferograms of the dynamic stall flowfield over a 7.62-cm-chord, NACA 0012 airfoil at free-stream Mach numbers ranging from 0.2 to 0.45 were obtained at a resolution of 0.5 deg (or better if needed). The corresponding nondimensional pitch rate was varied from 0.020 to 0.040. The Reynolds number of the flow based on airfoil chord ranged from 3.6×10^5 to 8.1×10^5.

The experiments were conducted in two phases. In the first phase, the full flowfield interferograms were obtained for a range of conditions; phase II focused on the leading-edge flow details only.

III. Results and Discussion

The interferogram images will first be discussed qualitatively as flow visualization images. The quantitative pressure distributions derived from the images will be presented in the second part of the section. Although much of the paper is devoted to the leading-edge flow, when appropriate, the full flowfield is also discussed.

A. Discussion of Interferogram Images

1. *Separation Bubble and Dynamic Stall*

Figure 1 is a point diffraction interferogram of the flow at $M = 0.3$, $\alpha = 12$ deg, and $\alpha^+ = 0.03$. This image reveals some

important features of the flow. The dark closed fringe on the lower surface slightly aft of the leading edge surrounds the stagnation point. The suction pressure developed by the airfoil causes the local flow to accelerate, resulting in strong density changes, which is seen in the figure as a concentration of fringes near the leading edge on the upper surface. The close spacing of the fringes also means that the flow gradients are high. In fact, 21 dark fringes are present within about 1 mm ($x/c \approx 0.1$) in this image, indicating that the local maximum Mach number is 0.71 and the local pressure coefficient is -3.75 at $x/c = 0.01$. Downstream of this point, a steep adverse pressure gradient region develops (see Sec. III.B.3) and flow separation occurs. The separated shear layer reattaches after it makes a transition into a turbulent layer, forming a classical laminar separation bubble. In the figure, the fringes in the bubble appear as lines emanating from the leading edge that turn abruptly toward the upper surface at $x/c \approx 0.05$ and turn sharply again as the local boundary layer is encountered. Inside the bubble, the fringes run parallel to the surface locally, representing the pressure plateau normally associated with laminar separation bubbles. The accompanying pressure distribution (which will be discussed in Sec. III.B.3) obtained with the fringe analysis software shows the suction peak, the drop in suction due to the adverse pressure following it, and the laminar separation bubble, which is indicated by the plateau in the distribution. In the interferograms to be discussed, the features upstream of the bubble are nearly the same, with the exception that more fringes appear with increase in angle of attack. As dynamic stall occurs, differences evolve will be pointed out.

2. *Leading-Edge Supersonic Flow*

Chandrasekhara et al.[16] found that the airfoil leading-edge flow can become supersonic, leading to formation of multiple shocks. Figure 2 provides quantitative documentation of this. Depending on the angle of attack, a shock or multiple shocks form in the flow. Figure 2 shows a PDI image for $M = 0.45$ at $\alpha = 12.6$ deg and $\alpha^+ = 0.0313$. Fringe counting shows that the local Mach number ahead of the first shock—at a height of $y/c \approx 0.04$—is greater than 1.0 and is about 1.2 at its foot. Although the flow is only weakly supersonic, the shock causes the leading-edge laminar boundary layer to separate.[16] This separated free shear layer develops waviness, which causes the flow downstream of the shock to go through a series of accelerations and decelerations. As the flow negotiates the crests and valleys of this wavy shear layer, expansion waves and compression waves develop, causing the series of shocks. The last shock in the series appears to be the strongest, and the flow becomes subsonic downstream. The occurrence of multiple shocks is repeatable, and the shocks were found to be present over an angle-of-attack range of about 1 deg.

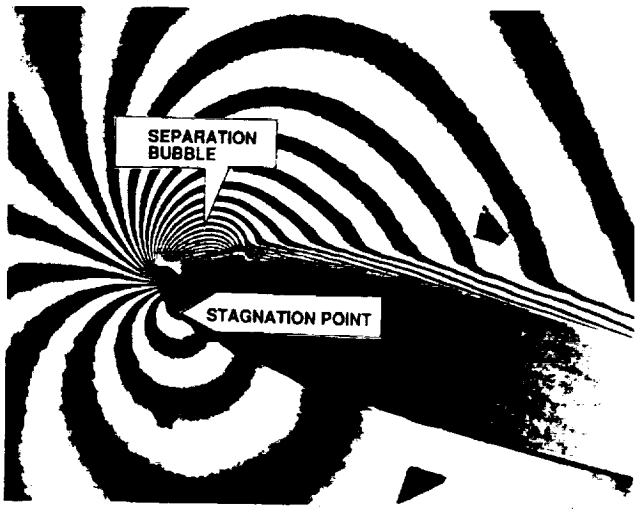

Fig. 1 Point diffraction interferogram; $M = 0.3$, $\alpha = 12$ deg, and $\alpha^+ = 0.03$.

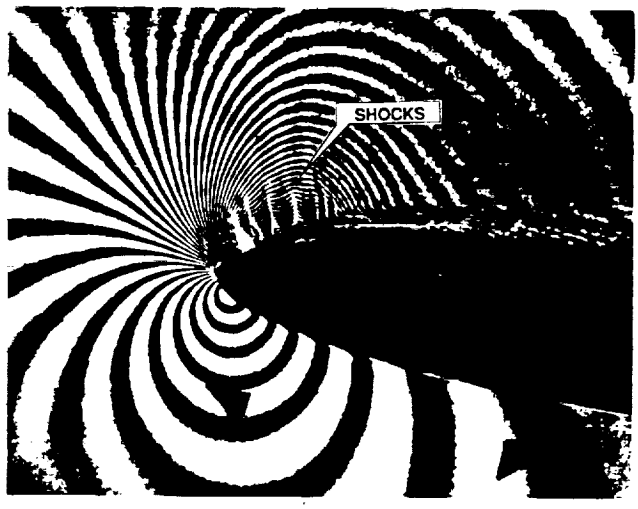

Fig. 2 Multiple shocks over a rapidly pitching airfoil; $M = 0.45$, $\alpha = 12.6$ deg, and, $\alpha^+ = 0.0313$.

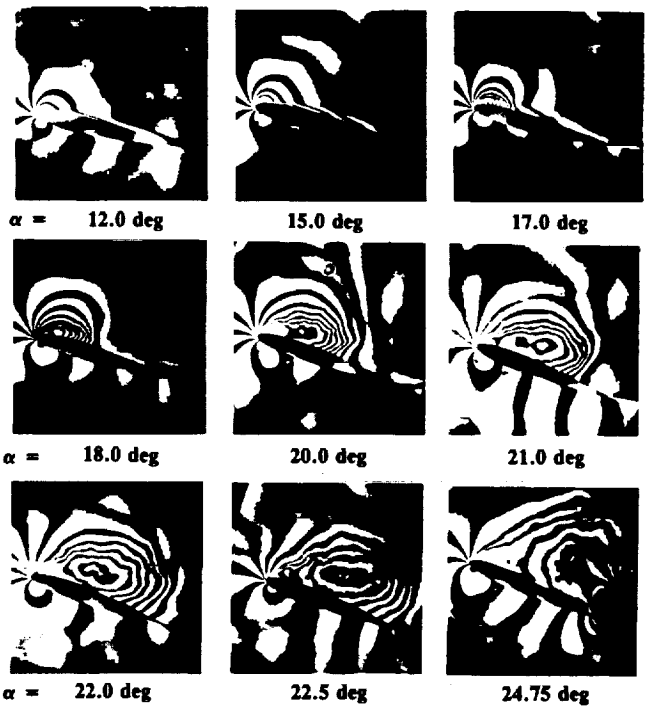

Fig. 3 Dynamic stall flow development over a transiently pitching airfoil; $M = 0.2$ and $\alpha^+ = 0.03$.

3. *Flow Description at $M = 0.2$ and $\alpha^+ = 0.03$*

Figure 3 presents a montage of interferograms for $M = 0.2$ at a nondimensional pitch rate of 0.03 for $12 \leq \alpha \leq 24.75$ deg. A separation bubble is present for $\alpha = 12$ deg; analysis of the interferograms showed that the bubble first appeared at $\alpha = 7$ deg (as opposed to about 6 deg in steady flow at $M = 0.2$). At $\alpha = 15$ deg, the upper surface fringe near the trailing edge indicates a mild local flow separation as this fringe first moves into the wake and turns sharply back toward the trailing edge. Also, the leading-edge bubble starts to open up, and the first imprint of the dynamic stall vortex becomes distinct at $\alpha = 17$ deg. As it grows, the enveloping shear layer moves downstream, and the airfoil boundary layer thickens. The growth of the vortex continues while it convects over the airfoil during the continuous ramping motion. For example, at $\alpha = 18$ deg, the center of the vortex is at $x/c = 0.1$, but the downstream

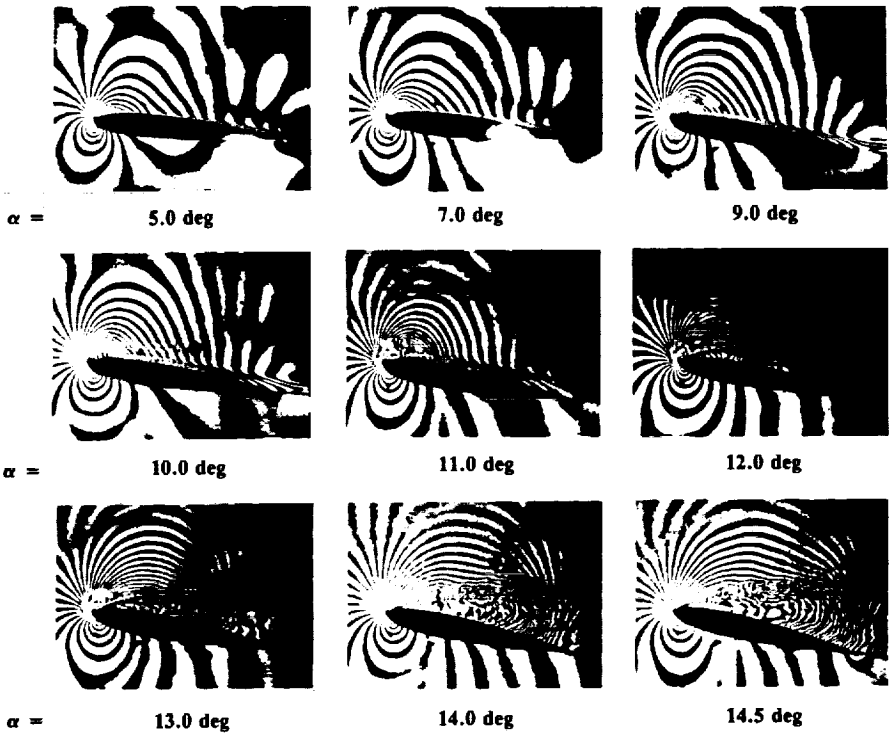

Fig. 4 Dynamic stall flow development over a transiently pitching airfoil; $M = 0.45$ and $\alpha^+ = 0.02$.

edge of the surrounding shear layer is at $x/c = 0.3$. The number of fringes is seen to increase until $\alpha = 18$ deg, demonstrating that the low-pressure region continues to grow. By $\alpha = 20$ deg, the leading-edge flow has separated, and the fluid aft of the shear layer enclosing the vortex has been convected past the trailing edge, and thus no fringes can be seen in this region. Once the vortex grows and begins to convect, the innermost fringes become circular (for example at $\alpha = 21$ and 22 deg), whereas the outer fringes still end on the surface. The number of fringes inside the vortex is now larger than that at the leading edge. This implies that the pressure in the vortex core is lower than the peak suction over the airfoil. Surface pressure measurements, however, cannot reveal this. The vortex is eventually shed by $\alpha = 24.75$ deg, and the flow reaches the deep stall state. A counterclockwise trailing-edge vortex also forms at this angle of attack. For this test condition, the vortex remains over the surface for a large angle-of-attack range of 12 deg. Similar studies on an oscillating airfoil ($\alpha = 10° + 10° \sin \omega t$) at $M = 0.2$ showed that deep stall occurred at $\alpha = 18.1$ deg. The presence of the dynamic stall vortex until $\alpha = 24.75$ deg elicits the fact that motion history plays a key role in the dynamic stall process. In this case, the transiently pitching airfoil is found to be better than oscillating airfoils in sustaining the dynamic lift generated.

4. Flow Sequence at $M = 0.45$ and $\alpha^+ = 0.02$

Figure 4 shows a similar set of interferograms for $M = 0.45$ at a nondimensional pitch rate of 0.02. At this Mach number, compressibility effects dominate.[16] The large number of fringes seen at low angles of attack is due to the larger density changes in the flow at this higher Mach number. The innermost closed fringe intersecting the lower surface near the leading edge encloses the stagnation point. There are 58 fringes (corresponding to a local Mach number of ≈ 1.2) around the leading edge in the first 1.5% of the airfoil chord at $\alpha = 9$ deg. A separation bubble forms in this case also and is seen clearly at $\alpha = 7$ deg. In steady flow at this Mach number, the bubble was first seen for $\alpha = 5$ deg. Thus, a delay is observed in its first appearance in the unsteady case. At $\alpha = 9$ deg, the first signs of the dynamic stall vortex/vortical structure are seen as a thin shear layer between the bubble and the airfoil upper surface near the leading-edge region (see also Fig. 5). Multiple shocks similar to those discussed in Fig. 2 form in this case also. The shocks remain on the surface until $\alpha = 11$ deg, even after the dynamic stall process is well under way. It is not yet clear whether the first shock-induced boundary-layer separation caused the dynamic stall vortex to form.

The vortex grows with increasing angle of attack as the shear layer enveloping it reattaches further down the airfoil toward the trailing edge. As in the low Mach number case, the fluid aft of this point has been swept away into the wake. This is a region of nearly stagnant fluid. No circular fringes are found in the vortex; instead, only half-circular fringes are seen. At $\alpha = 14.5$ deg, the shear layer has reached the trailing edge, and deep stall occurs at $\alpha = 15.5$ deg. The entire sequence lasts only 6–7 deg in angle of attack, which is considerably smaller than the 12-deg range seen for $M = 0.2$. Although the lower Mach number result discussed was obtained at a nondimensional pitch rate that was 50% higher, the range of angle of attack over which dynamic lift is sustained is nearly twice that seen at $M = 0.45$. This confirms the result obtained from the earlier schlieren studies[16] that compressibility promotes stall. These results agree with those reported in Ref. 17 for the oscillating airfoil. However, it should be noted that the two different motion histories will force differences in the details of separation. Dynamic stall of oscillating airfoils is influenced by the constantly changing pitch rate through a cycle and also by hysteresis. These affect all aspects of the flow. The transiently pitching airfoil flow is free of these effects. In addition, since the airfoil continues to pitch to 60 deg, which is well beyond the static stall angle, the development of the post-stall flow and the interactions at the trailing edge can be studied (discussed in Sec. III.A.6), which is of importance to the supermaneuverability problem. This information is also of value in comparing computed results against experiments.

The differences in the vortex size and structure also imply that the overall (global) pressure fields in the incompressible and compressible flow cases are quite different. The sustained presence of a low-pressure region over the airfoil upper surface is evidence that even in the compressible case there is increased lift generated during the dynamic stall process.

5. Leading-Edge-Flow and Stall-Vortex Formation

Carr et al.[17] found that, for an oscillating airfoil, the dynamic stall vortex formed just as the separation bubble burst. It has now been found to be true for the transiently pitching airfoil also. Figure 5 presents some interferograms that demonstrate this result for $M = 0.3$ and $\alpha^+ = 0.03$. At $\alpha = 15$ deg, the fringes enclosing the bubble at a lower angle of attack (not shown) begin to "open up," and vertical fringes (normal to the upper surface) appear near the downstream end of the bubble. This can be seen more clearly at $\alpha = 15.5$ deg. By $\alpha = 15.75$ deg, these fringes extend to about 1.5% of chord above the airfoil and nearly to $0.2c$ along it. The inflection in the fringes very close to the airfoil surface suggests that there is a very slight reverse flow. In contrast, the outer fringes (outside the bubble) proceed only in one direction, toward the trailing edge. The region of reverse flow is less than $0.005c$, and thus it is extremely difficult to detect with experimental techniques other than surface mounted gauges. By $\alpha = 16.5$ deg, the vortex has fully developed and convected to $0.2c$. This rapid succession of events in a very small angle-of-attack range is typical of the evolution of dynamic stall at compressible Mach numbers. However, the interactions between shocks and the boundary layer, along with the events of bubble bursting and vortex formation, are too complicated to be resolved from the images processed so far.

The primary issue that needs to be determined is the origin of the dynamic stall vortex. Whether it originates independently of the separation bubble and simply pushes the back end of the bubble, or the increasing angle of attack makes it no longer possible for the bubble to remain close to the leading edge and moves the reattachment point rearward, allowing the leading-edge vorticity to coalesce, is yet to be found. This is an intriguing issue, especially because the leading-edge flow has already separated, causing the bubble, at a very low angle of attack (much lower than the static stall angle). A plausible description is that the recirculation region in the bubble becomes stronger with increase of angle of attack, eventually forcing a breakdown of the leading-edge flow and leading to the vortex formation. However, a much more careful analysis is needed for clarifying the issues.

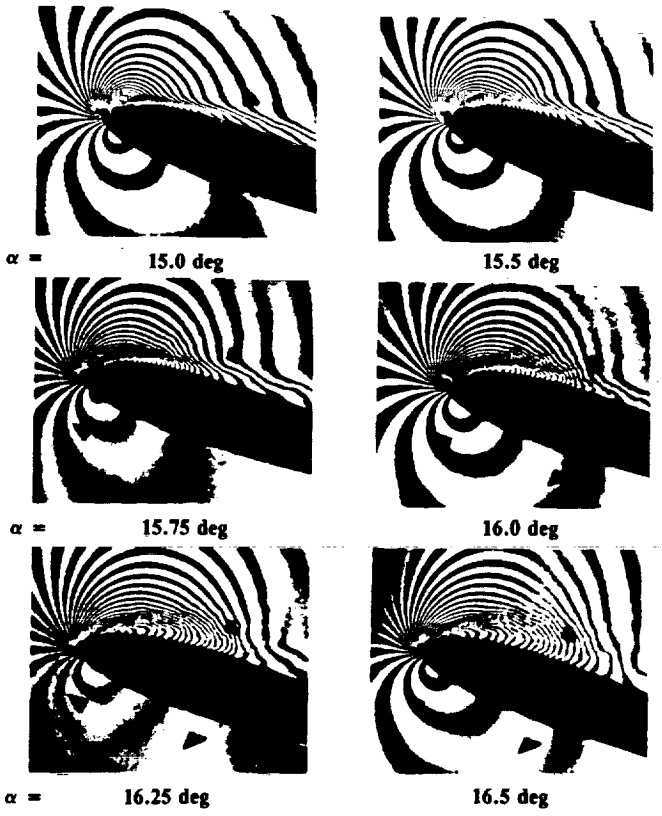

Fig. 5 Details of dynamic stall vortex development over a transiently pitching airfoil; $M = 0.3$ and $\alpha^+ = 0.03$.

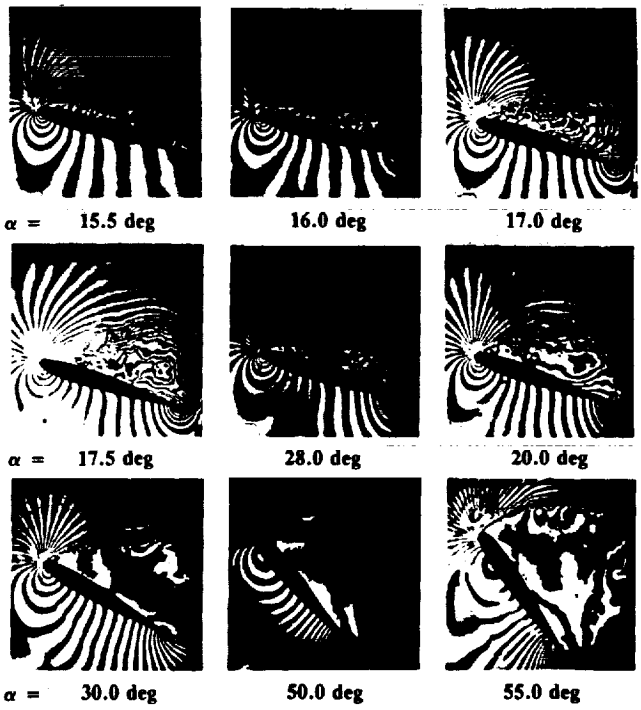

Fig. 6 Trailing-edge flow interactions with dynamic stall vortical flow over a transiently pitching airfoil; $M = 0.45$ and $\alpha^+ = 0.025$.

The formation of a separation bubble indicates that the airfoil leading-edge boundary-layer transition plays a critical role in dynamic stall occurrence. If the boundary layer is modified to transition before the adverse pressure gradient is encountered, it is to be expected that dynamic stall and the associated events occur in a very different manner. This includes stall onset, the details of the vortex formation, and the duration of dynamic lift in the pitching cycle. This is a further aspect that merits a more detailed study.

6. Trailing-Edge Flow Beyond Deep Stall

The flow continues to show interesting features even after deep stall has occurred and the dynamic stall vortex is shed. In Fig. 6, the complete flowfield is shown for just one experimental flow condition ($M = 0.45$ and $\alpha^+ = 0.025$). For this case, the dynamic stall angle of attack (when the dynamic stall vortex leaves the airfoil) is 17 deg; however, the airfoil continues to pitch at a constant rate until $\alpha = 60$ deg. An immediate consequence of vortex shedding under these conditions is an increase in suction pressure at the trailing edge on the lower surface of the airfoil. The trailing-edge suction gradually increases during the dynamic stall process as the airfoil pitches (from $C_p \approx 0.0$ at $\alpha = 0$ deg to $C_p = -0.504$ at $\alpha = 17$ deg). However, at $\alpha = 17.5$ deg, the suction pressure coefficient jumps to -1.04. Also, a counterclockwise vortex begins to form in the near wake at $\alpha = 18$ deg. The birth/growth of this vortex pushes outward the shear layer separating from the leading edge. At $\alpha = 20$ deg, this vortex is shed, and by $\alpha = 30$ deg, only the separated flow can be seen over the upper surface. The same number of fringes (26, corresponding to $C_p = -1.08$), measured from the stagnation point to the lowest velocity point on the upper and lower surface shear layers, seems to indicate that the pressure over the upper surface is nearly constant. However, since the field of view is limited in the facility, the role of the wake and the interaction of the two shear layers cannot be determined to ascertain this fully. As the pitch up continues, shear layer instabilities develop, which roll up into vortices, which appear at $\alpha = 50$ or 55 deg. A large

trailing edge vortex appears from the lower surface at $\alpha = 50$ deg, which rolls up toward the leading-edge shear layer. The peak suction increases slightly with angle of attack, even though the airfoil is in the deep stall state. The stagnation point moves to 0.25 chord point at $\alpha = 55$ deg. Similar features were found for other Mach numbers as well. However, this picture is significantly different from the low Reynolds number and low Mach number results of Walker et al.,[5] who observed two large vortices coexisting on the airfoil suction surface as dynamic stall progressed. This led to a much different airfoil surface pressure distribution than found here. For all of the cases studied here, the trailing-edge vortex was induced as the dynamic stall vortex was shed. At times the leading-edge separated shear layer instabilities produced a large vortex, resulting in a double vortex pattern resembling a vortex street.

B. Quantitative Pressure Field

One of the main advantages of PDI is its truly nonintrusive way of yielding the pressure field. To obtain the average surface pressure distribution by standard techniques in a rapidly changing flow such as the ramping airfoil motion under consideration requires several realizations of the flow, i.e., several pitch-up motions. The PDI technique provides not only the surface pressure map but also the global pressure field instantaneously in one picture, unaffected by history effects. Since a large number of interferograms were obtained at close intervals in angle of attack, a finer set of instantaneous pressure data is in hand now when compared with what can be obtained for an airfoil with a fixed set of pressure taps. The data to be reported are the first global mapping of pressure coefficients that have been obtained for a transiently pitching airfoil under compressibility conditions using PDI.

1. Effect of Mach Number on Peak Suction Pressure

Figure 7 shows the peak suction pressure coefficient obtained over the airfoil at different Mach numbers for different pitch rates. The absolute value of C_p in steady flow is lower than in unsteady flows for all Mach numbers tested. Of significance is the relative independence of the peak suction pressure coefficient from the pitch rate for all Mach numbers. It is possible that the formation of the bubble and the strong local compressible conditions have both affected the viscous/inviscid interactions in the flow and thus limited the suction pressure from increasing as the pitch rate is increased. Also, the peak suction decreases dramatically with increasing Mach number. For the lowest Mach number of 0.2, the value of $C_p = -7.1$ corresponds to a local Mach number of 0.58, indicating that compressibility conditions play a role in the process. At $M = 0.45$, the sonic limit is $C_p = -2.78$, and with the suction peak at $C_p = -3.6$, the local flow is supersonic and thus is strongly compressible.

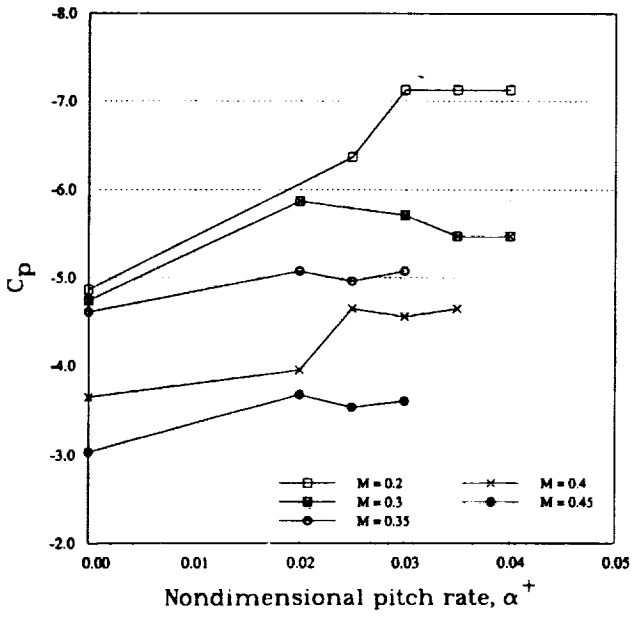

Fig. 7 Transiently pitching airfoil peak suction pressure coefficient at stall vortex formation.

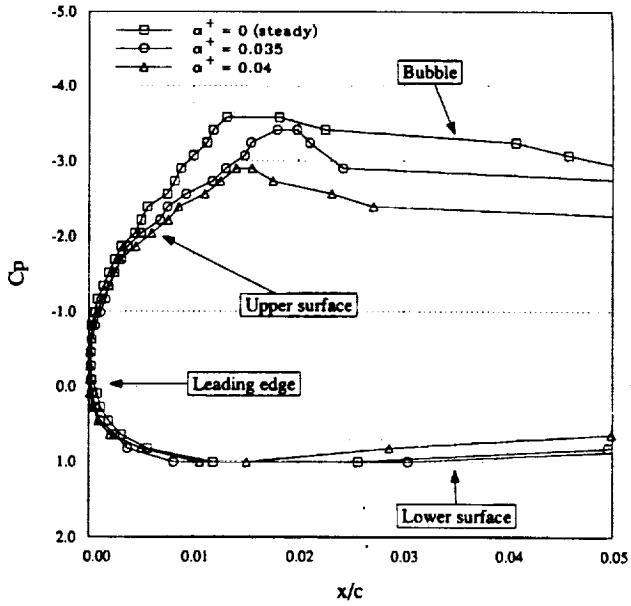

Fig. 8 Effect of pitch rate on pressure development over a transiently pitching airfoil; $M = 0.3$ and $\alpha = 10$ deg.

2. Effect of Pitch Rate

In Figure 8, the development of the leading edge-pressure distribution over the first 5% of airfoil chord is compared for $M = 0.3$ for steady flow, $\alpha^+ = 0.035$ and $\alpha^+ = 0.04$ at $\alpha = 10$ deg. It is clear that steady flow develops a stronger suction peak than the unsteady flow cases, with a maximum C_p of -3.6; the suction peak is located at $x/c = 0.012$. The adverse pressure gradient is slower to develop at the higher pitch rates; in fact, the suction level has reached only a value of $C_p = -2.95$ at 10 deg for $\alpha^+ = 0.04$. The pressure distribution for the unsteady cases is less steep than that seen for steady flow. Even though all three cases show a separation bubble, the effect of increasing pitch rate is clearly to delay the flow development over the leading edge, which consequently leads to delay in dynamic stall occurrence.

Figure 9 shows the maximum suction pressure coefficient at different angles of attack for $M = 0.4$. In it, steady flow and unsteady flows at $\alpha^+ = 0.02$ and $\alpha^+ = 0.035$ are compared. The steady flow stalls at $\alpha = 10.8$ deg; at higher angles the leading-edge suction falls rapidly. At $\alpha^+ = 0.02$ the effect of unsteadiness in causing the peak suction pressure coefficient to lag the steady flow values is seen at all angles of attack; the suction levels for $\alpha^+ = 0.035$ lag those of even $\alpha^+ = 0.02$. The rounding of the curves at the top corresponds to the situation when the dynamic stall vortex is in the formative stages. During this stage ($\alpha = 12$–13 deg for $\alpha^+ = 0.02$ and $\alpha = 13$–13.5 deg for $\alpha^+ = 0.035$), the airfoil suction is the maximum. Once the vortex begins to convect, the leading-edge flow slows down, and the suction is steadily lost, even though the angle of attack is still increasing. Despite experimental scatter, it is clear that dynamically pitching airfoils can withstand larger suction peaks than steady airfoils before stall and hence withstand higher flow gradients before dynamic stall occurrence. It is also of value to note that the loss of suction peak in the dynamic case does not mean loss of lift but only the initiation of the dynamic stall vortex.

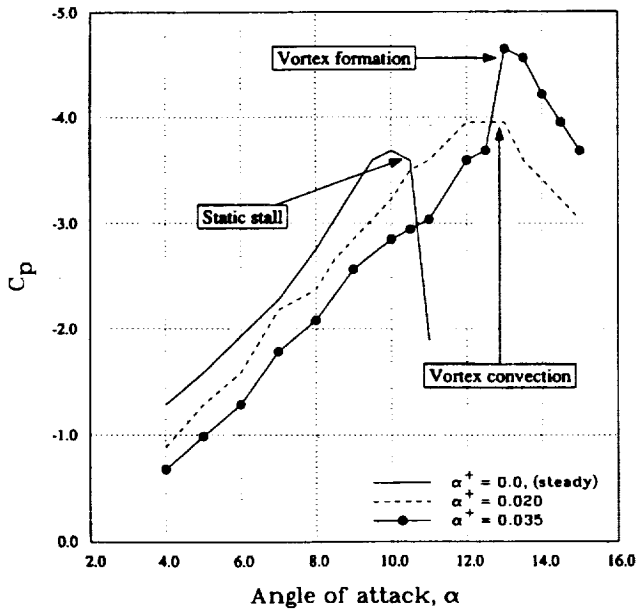

Fig. 9 Effect of pitch rate on peak suction pressure coefficient over a transiently pitching airfoil; $M = 0.4$.

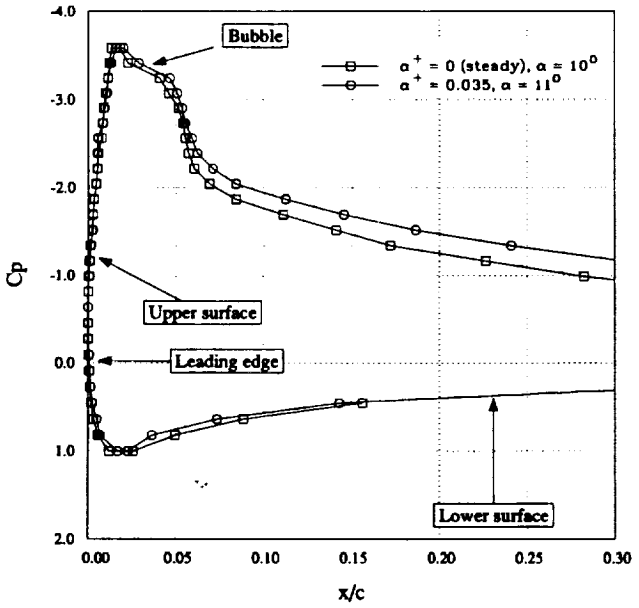

Fig. 10 Comparison of steady and unsteady flows; $M = 0.3$.

Figure 10 shows the pressure distribution at $M = 0.3$ at $\alpha = 10$ deg in steady flow and $\alpha = 11$ deg in unsteady flow at $\alpha^+ = 0.035$. The nearly identical pressure distributions suggest that unsteadiness essentially has introduced a 1-deg lag in the effective angle of attack, including the formation of the separation bubble (see next section), supporting the conclusions drawn from Figs. 8 and 9. As much as 2 deg of decrease in the effective angle of attack for oscillating airfoils was observed by Carr et al.[17] However, as can be expected, the amount of this benefit is determined by the experimental conditions, especially the pitch rate and Mach number.

3. *Airfoil Pressure Distributions*

Airfoil pressure distributions were obtained for different Mach numbers and pitch rates using the method described earlier. A typical case is discussed here for $M = 0.3$ and $\alpha^+ = 0.035$ at different angles of attack in Fig. 11. For this case, Fig. 11a shows that, at $\alpha = 5$ deg, the pressure distribution is smooth, with the suction peak of $C_p = -1.69$ at $x/c = 0.025$. As the airfoil pitches to 7 deg, C_p increases to -2.21. This is accompanied by the upstream movement of the suction peak to $x/c = 0.015$. Along with this, the stagnation point moves from $x/c = 0.01$ to 0.025. As the airfoil pitches to higher angles of attack, further movement of the stagnation point is difficult to detect, until larger angles are reached. At $\alpha = 8$ deg, a separation bubble forms. The pressure plateau following the steep drop in the pressure distribution immediately after the suction peak at $\alpha = 9$ deg confirms this. The bubble extends to $x/c \approx 0.05$. The suction level and the adverse pressure gradient both continue to increase as the airfoil angle of attack is increased. However, Fig. 11b shows that the pressure distributions at $\alpha = 13$ and 14 deg are different from those at $\alpha = 12$ deg only near the suction peak, indicating that the lift and thus the circulation over the airfoil have not changed significantly in this range of pitching. It is also the range when the dynamic stall vortex is initiated as determined by visual analysis of the interferogram images. The suction peak, however, increases with angle of attack and reaches its maximum value of -5.8 when the first imprint of dynamic stall is clearly discernible in the images. At this instant, it appears that the vortex becomes fully organized, and then it begins to convect. The movement of the vortex results in a

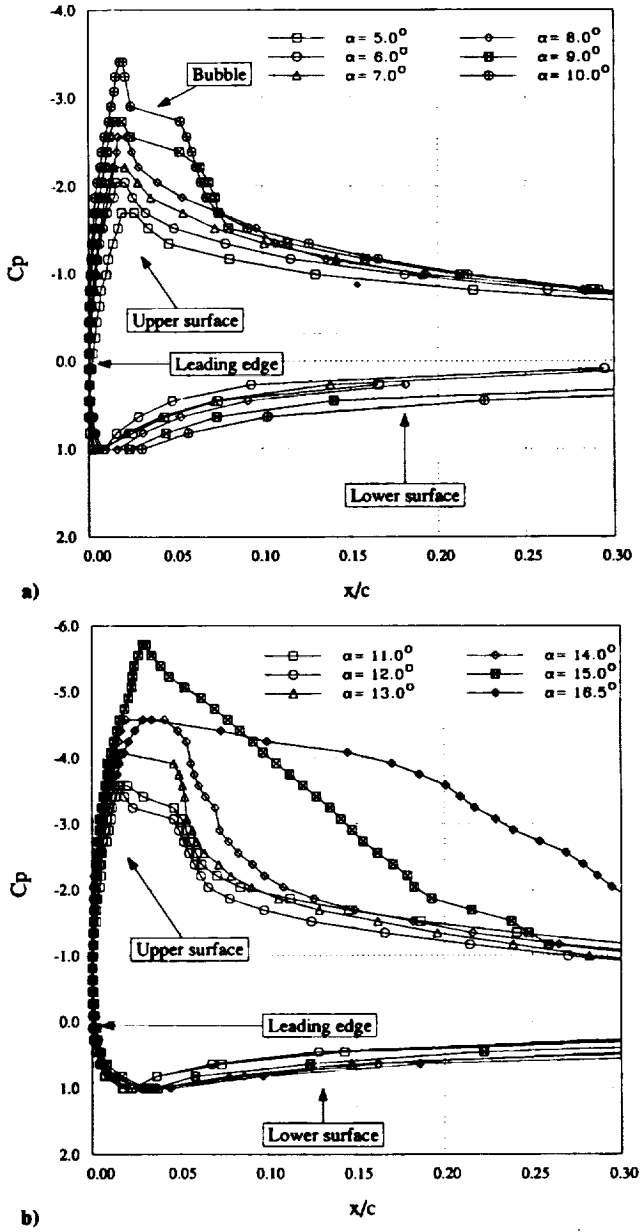

Fig. 11 Pressure distribution over a transiently pitching airfoil; $M = 0.3$ and $\alpha^+ = 0.35$: a) $\alpha = 5$–10 deg, b) $\alpha = 11$–16.5 deg.

slight drop of airfoil suction. However, the pressure distribution changes to the nearly flat-top shape that extends to about $x/c = 0.3$. This increasing region of low pressure over the upper surface is the cause of the vortical lift seen in the flow. Further pitching of the airfoil continues to decrease the suction levels, while spreading the extent of the vortex more over the airfoil, until it is shed past the trailing edge.

IV. Concluding Remarks

A nonintrusive study of the compressibility effects on dynamic stall of a transiently pitching airfoil has been conducted. The study shows the following.

1) Multiple shocks form over the airfoil and are present through the early stages of dynamic stall for a freestream Mach number of 0.4 and higher.

2) Detailed instantaneous pressure distributions show that dynamic stall onset and bursting of the separation bubble occur simultaneously.

3) Flow interferograms and hence the corresponding pressure distributions show that compressibility causes the dynamic stall vorticity to be retained closer to the airfoil surface. The vortical structure in the compressible case is very different than that in the incompressible case.

Acknowledgments

The project was supported by an Air Force Office of Scientific Research Grant MIPR-92-0004 to the Naval Postgraduate School and was monitored by D. B. Fant. Additional support was received from Army Research Office Grant MIPR-130-92, monitored by T. L. Doligalski. The work was carried out in the Fluid Mechanics Laboratory Branch of NASA Ames Research Center. The steady encouragement of S. S. Davis, chief, FML Branch, the support of J. D. Loomis in the conduct of experiments, and the interferogram processing software development effort of P. J. Trosin, Sterling Federal Systems, Inc., are greatly appreciated.

References

[1]Acharya, M., and Metwally, M. H., "Evolution of the Unsteady Pressure Field and Vorticity Production at the Surface of a Pitching Airfoil," AIAA Paper 90-1472, June 1990.

[2]Francis, M. S., and Keese, J. E., "Airfoil Dynamic Stall Performance with Large-Amplitude Motions," *AIAA Journal*, Vol. 23, No. 11, 1985, pp. 1653–1659.

[3]Aihara, Y., Koyama, H., and Murashige, A., "Transient Aerodynamic Characteristics of a Two-Dimensional Airfoil During Stepwise Incidence Variation," *Journal of Aircraft*, Vol. 2, No. 8, 1985, pp. 661–668.

[4]Albertson, J. A., Troutt, T. R., and Kedzie, C. R., "Unsteady Aerodynamic Forces at Low Airfoil Pitching Rates," *Proceedings of the 1st National Fluid Dynamics Conference*, Vol. 1, AIAA, Washington, DC, 1988, pp. 454–462.

[5]Walker, J. M., Helin, H. E., and Strickland, J. H., "An Experimental Investigation of an Airfoil Undergoing Large-Amplitude Pitching Motions," *AIAA Journal*, Vol. 23, No. 8, 1985, pp. 1141, 1142.

[6]Jumper, E. J., Shreck, S. J., and Dimmick, R. L., "Lift-Curve Characteristics for an Airfoil Pitching at Constant Rate," *Journal of Aircraft*, Vol. 24, No. 10, 1987, pp. 680–687.

[7]Lorber, P. F., and Carta, F. O., "Airfoil Dynamic Stall at Constant Pitch Rate and High Reynolds Number," *Journal of Aircraft*, Vol. 25, No. 6, 1988, pp. 548–556.

[8]Visbal, M. R., "Dynamic Stall of a Constant Rate Pitching Airfoil," *Journal of Aircraft*, Vol. 27, No. 5, 1990, pp. 400–407.

[9]Chandrasekhara, M. S., and Carr, L. W., "Flow Visualization Studies of the Mach Number Effects on the Dynamic Stall of an Oscillating Airfoil," *Journal of Aircraft*, Vol. 27, No. 6, 1990, pp. 516–522.

[10]Chandrasekhara, M. S., Carr, L. W., and Ahmed, S., "Comparison of Pitch Rate History on Dynamic Stall," *Proceedings NASA/AFOSR/ARO Workshop on Physics of Forced Unsteady Separation*, NASA-CP-3144, April 1990.

[11]Carr, L. W., and Chandrasekhara, M. S., "Design and Development of a Compressible Dynamic Stall Facility," *Journal of Aircraft*, Vol. 29, No. 3, 1992, pp. 314–318.

[12]Chandrasekhara, M. S., and Carr, L. W., "Design and Development of a Facility for Compressible Dynamic Stall Studies of a Rapidly Pitching Airfoil," *ICIASF'89 RECORD*, IEEE Publication 89CH2762-3, IEEE, New York, 1989, pp. 29–37.

[13]Carr, L. W., Chandrasekhara, M. S., Ahmed, S., and Brock, N. J., "A Study of Dynamic Stall Using Real Time Interferometry," AIAA Paper 91-0007, Jan. 1991.

[14]Brock, N. J., Chandrasekhara, M. S., and Carr, L. W., "A Real Time Interferometry System for Unsteady Flow Measurements," *ICIASF'91 RECORD*, IEEE Publication 91CH3028-8, IEEE, New York, 1991, pp. 423–430.

[15]Goldstein, R. J., "Optical Systems for Flow Measurement: Shadowgraph, Schlieren, and Interferometric Techniques," *Fluid Mechanics Measurements*, Hemisphere, New York, 1985, pp. 377–422.

[16]Chandrasekhara, M. S., Ahmed, S., and Carr, L. W., "Schlieren Studies of Compressibility Effects on Dynamic Stall of Transiently Pitching Airfoils," *Journal of Aircraft*, Vol. 30, No. 2, 1993, pp. 213–220.

[17]Carr, L. W., Chandrasekhara, M. S., and Brock, N. J., "A Quantitative Study of Unsteady Compressible Flow over an Oscillating Airfoil," AIAA Paper 91-1683, June 1991.

Appendix B:

Transition Effects on Compressible Dynamic Stall of Transiently Pitching Airfoils

AIAA-93-2978

Transition Effects on Compressible Dynamic Stall of Transiently Pitching Airfoils

M.C.Wilder, MCAT Institute, San Jose, CA;
M.S.Chandrasekhara, Naval Postgraduate School, Monterey, CA; and
L.W.Carr, U.S.Army ATCOM,
NASA Ames Research Center,
Moffett Field, CA

AIAA 24th
Fluid Dynamics Conference
July 6-9, 1993 / Orlando, FL

Transition Effects on Compressible Dynamic Stall of Transiently Pitching Airfoils

M.C. Wilder[1]
Navy-NASA Joint Institute of Aeronautics and
MCAT Institute, San Jose, CA

M.S. Chandrasekhara[2,*]
Navy-NASA Joint Institute of Aeronautics
Department of Aeronautics and Astronautics
Naval Postgraduate School, Monterey, CA 93943

and
L.W. Carr[3]
U.S.Army ATCOM and Fluid Mechanics Laboratory Branch
NASA Ames Research Center, Moffett Field, CA 94035-1000

Abstract

Experimental results and analysis of the effects of boundary layer tripping on dynamic stall of a transiently pitching airfoil are presented. At low Mach numbers, the tripped airfoil exhibits qualitative similarity with the behavior of the untripped airfoil. However, the local supersonic flow at Mach numbers greater than 0.3 is significantly modified by the trip leading to vastly different shock/boundary layer interactions, dynamic stall onset and vortex formation angles. The formation of the laminar separation bubble is found to have a favorable influence in delaying dynamic stall on the untripped airfoil flow. In both Mach number regimes, the tripped flow actually stalls at slightly lower angles of attack. Further experimentation with three trips on an oscillating airfoil showed that the dynamic stall process is very sensitive to the state of the turbulence in the boundary layer. This sensitivity points to a need for finer turbulence modeling techniques for use in dynamic stall computations.

Nomenclature

C_p	pressure coefficient
c	airfoil chord
D_g	grit size
K	constant based on wind tunnel turbulence level
M	free stream Mach number
R	unit Reynolds number
Re	Reynolds number based on c and U_∞
U_∞	free stream velocity
x,y	chordwise and vertical distance
α	angle of attack
$\dot{\alpha}$	pitch rate in deg/sec
α^+	nondimensional pitch rate, $\frac{\dot{\alpha}c}{U_\infty}$

1. Introduction

Dynamic stall is a problem of great interest to aerodynamicists since it offers the potential for enhancing the maneuverability and agility of aircraft. This potential is significantly affected by the onset of compressibility effects in flows over pitching airfoils. A sizeable data base[1,2] now confirms that above a free stream Mach number of 0.3, compressibility dominates the flow. Firstly, compressibility promotes premature stall. Additionally, the large flow acceleration can cause locally supersonic flows and induce a series of shocks[2,3] introducing other flow interactions. Available laboratory experiments on compressible dynamic stall have been conducted at low Reynolds numbers (300,000 to 1,000,000 - with the exception of McCroskey et al[4] and Lorber and Carta[5]). These low Reynolds number experiments have revealed that dynamic stall originates rapidly over a very small angle of attack range[3,6] as the laminar separation bubble that forms over the airfoil bursts. Further, most of the events of dynamic stall are concentrated near the leading edge region of the airfoil executing the rapid pitch-up motion. The formation of the separation bubble clearly indicates that the flow was laminar initially and then transitioned to reattach as a turbulent shear layer. Flow reattachment generally occurs[3] between x/c = 0.05 - 0.08 for the angle of attack range (6 -13 degrees) of interest in dynamic stall. The exact location depends upon where transition occurs and how the transition length is affected by the local flow conditions, in particular by the adverse pressure gradient. Gostelow et al[7] point out that the transition length is reduced considerably by large adverse pressure gradients. Thus, it should be expected that the transi-

[1] *Research Scientist*

[2] *Associate Director and Research Associate Professor, Assoc. Fellow AIAA,*

***Mailing Address: M.S. 260-1, NASA Ames Research Center, Moffett Field, CA 94035-1000**

[3] *Research Scientist and Group Leader, Unsteady Viscous Flows, Aeroflightdynamics Directorate, Member AIAA*

tion process varies as the airfoil pitches up. Since low Reynolds number dynamic stall is intricately coupled to the bursting of the separation bubble, the process is also influenced by the transition process. To some extent, even high Reynolds number studies could be affected by this problem since the boundary layer is laminar near the stagnation point. Only when transition occurs before reaching the suction peak could one expect the bubble not to play a major role.

The experimental quantification of the role of transition on the details of the dynamic stall process is a daunting task. However, it is also an important task because the experimental data is needed for estimation of high Reynolds number behavior based on low Reynolds number experiments as well as, for computational code validation effort. It is worthwhile noting here that owing to the complex nature of the flow and a lack of the understanding of the physical processes, contemporary computational fluid dynamicists either ignore transition and perform a fully turbulent calculation[8] or arbitrarily fix[9] transition at a certain x/c location and invoke a turbulence model from this location in the computations. Thus, the usefulness of the computational results becomes severely limited for quantitative comparisons. Also, extrapolation of laboratory results to prototype or flight situations is also of limited value until this issue is addressed. In any case, validation of the computed data needs experimental results, which were hitherto not available.

The present paper reports some experimental results on compressible dynamic stall obtained by tripping the boundary layer with a three dimensional roughness. Most of the results will address the behavior of dynamic stall over a transiently pitching airfoil, which were obtained with a roughness height of about $175\mu m$. Subsequently, more measurements were performed to investigate the flow over an oscillating airfoil with this and two other roughness elements; these will be compared when appropriate. A real time point diffraction interferometry (PDI) technique was used to obtain the global as well as surface density fields. The images were processed to yield pressure distributions to compare the various cases quantitatively. The results clearly demonstrate the need for proper tripping of the boundary layer in these complicated flows.

2. Experimental Facility and Techniques

2.1. Facility Description

The results to be presented in this paper are part of an ongoing dynamic stall research program in the Navy-NASA Joint Institute of Aeronautics. The experiments were conducted in the *Compressible Dynamic Stall Facility (CDSF)* in the Fluid Mechanics Laboratory(FML) of NASA Ames Research Center. The facility permits study of dynamic stall over a range of Mach numbers, using non-intrusive optical flow diagnostic techniques. It is operated as a part of the in-draft tunnel complex at the FML (for details see Carr and Chandrasekhara[10]). In the CDSF, the airfoil is supported between two 2.54cm thick optical quality glass windows by pins. Since the pins are smaller than the local airfoil thickness, unobstructed optical access is available to the entire flow field. Thus it is possible to study the flow at the surface near the leading edge, where the dynamic stall vortex forms, as well as the flow field away from the airfoil.

The transient pitching motion was produced by a custom designed hydraulic system. Ref. 11 provides the details of the drive and these are briefly given below.

angle of attack, α:	0-60°
pitch rate, $\dot{\alpha}$:	0-3600 °/sec
maximum acceleration rate:	600,000 $°/sec^2$
change in α during acceleration:	$\leq 6°$ of pitch
minimum acceleration time:	4 ms
free stream Mach number:	0.1-0.5
airfoil chord:	7.62cm
Reynolds number:	$2x10^5$ - $9x10^5$

The angle of attack range and the highest pitch rate of 3600 °/sec on the 7.62 cm chord airfoil corresponds to a 90°/sec pitch rate of a 3m chord airplane wing at any given Mach number; thus, the rates obtainable from the design are directly applicable to flight conditions. The system controls are such that no effects of the system transients on flow separation are noticeable. The system uses both the airfoil position and velocity information in its feed back loops to properly execute any pre-programmed maneuver. The change in angle of attack during acceleration and the acceleration time itself are limited to less than 6° and 4 ms, respectively.

A digital optical encoder provided the instantaneous airfoil position. It was recorded from the digital I/O board of a microVAX II workstation and the pitch rate was timed with the computer internal clock. The pitch rate was constant to within 1% over the angle of attack range of interest at the highest pitch rates since it was specifically tuned for such rates. At slower rates, a mild change (less than 2%) was noticed at $\alpha = 15^0$. But, since this angle was considerably higher than the static stall or the dynamic stall onset angle, it is believed to have no effects on the results.

2.2. The Trip

Transition was fixed by applying a strip of randomly placed roughness elements along the upper surface of the airfoil, near the leading edge. A formula given in Ref. 13 was used to estimate the minimum size of the roughness elements required to trip the boundary layer. The formula is

$$D_g = \frac{12K}{R}$$

where D_g is the grit size in inches, R is the Reynolds number per foot of length for the free stream flow, and K is a constant which depends on tunnel turbulence level and may be assumed to be 400. This formula indicated a grit size diameter of $D_g = 56 - 89\mu m$ (0.0022 - 0.0035 in) for the Mach number range $0.2 \leq M \leq 0.3$.

Number 220 polishing grit with a size range of 74 - 89 μm (0.0029 - 0.0035 in) was selected for the construction of the boundary-layer trip. The grit was

glued to the airfoil surface with a water soluble adhesive (Polaroid print coating material). The region of airfoil surface around the intended trip location was masked off with tape, the glue was brushed on to the exposed surface, and then the grit was applied with an air brush to insure an even distribution of the roughness elements. The trip stretched the entire span of the airfoil and extended from x/c = 0.005 to x/c = 0.03 along the upper surface. A schematic is presented in Fig. 1 indicating the location and thickness of the trip. The profile was obtained from a digitized photograph of the airfoil under no-flow conditions and indicates that the maximum thickness of the trip was $175\mu m$. The added thickness was attributable to the adhesive base.

The results presented in this paper were obtained for a transiently pitching airfoil equipped with the trip described above. Subsequent experiments were performed on the flow over an oscillating airfoil with this and two other trips. The oscillating airfoil data are still being analyzed, but some preliminary results will be discussed where relevant. A spray-on enamel lacquer replaced the Polaroid coating as the bonding medium for the grit. The lacquer could be applied in a thiner coat and had a longer curing time, which facilitated applying the grit uniformly. The second trip was a thin version of the first trip with a maximum thickness of $\sim 100\mu m$, extending from x/c = 0.005 to x/c = 0.03. The third trip extended from x/c = 0.05 on the lower surface near the stagnation point and around the leading edge to x/c = 0.03 on the upper surface; the thickness was $\sim 130\mu m$.

2.3. Point Diffraction Interferometry Technique

The point diffraction interferometry technique used in this study utilized a point discontinuity (in the form of a pin-hole) located at the image of a point light source to diffract a portion of the incident light into a spherical reference wave front. In the present application, the primary optics of an existing schlieren system were used (see Ref. 12 for details), with a pulsed Nd:YAG laser replacing the conventional spark as the light source, and a specially created point diffractor replacing the usual knife edge. The laser light was expanded through a microscope objective to fill the schlieren mirror, transmitted through the test section, and refocused by another schlieren mirror. The exposed photographic plate used to create the point-diffraction spot was placed at the focus of this second mirror, and the laser was pulsed with enough energy to burn a hole, or spot, in the emulsion. The spot was created *in situ* by passing light through the test section at under no-flow condition. It was also precisely tailored to the application under investigation, automatically correcting for nonuniformities in the light source or optics. The tunnel was turned on and the real-time interference fringes were recorded on Polaroid film(ASA 3000), and were available for immediate viewing.

The analysis of the interferograms was conducted using a package developed in-house for the purpose. The PDI images were digitized and the images processed on an IRIS Work Station to obtain the fringe intersections with the airfoil contour. Using isentropic flow relations, the fringe numbers and hence, the fluid densities were converted to pressure coefficients. This assumption was made even through the boundary layer and the vortex, for lack of better flow relations. However, it is not believed to introduce substantial errors in the pressure field, since the entropy change is generally small, until deep stall occurs.

2.4. Experimental Conditions

The experiments were conducted on a 7.62 cm chord, NACA 0012 airfoil. The following conditions were chosen for the tripped airfoil studies. (The corresponding data for the untripped airfoil was already available[3]).

M	α^+					
	0	0.02	0.025	0.03	0.035	0.04
0.2	X		X	X		X
0.3	X	X	X	X	X	X
0.45	X	X	X	X		

The chord Reynolds number ranged from 360,000 at M = 0.2 to 810,000 at M = 0.45. The airfoil was pitched from 0 - 60^0 about the $\frac{1}{4}c$ point. The interferograms were obtained at the desired instantaneous angles of attack during separate pitch-up motions (one picture/pitch-up) for 0 - 20^0 angle of attack by strobing the laser externally. The laser pulse was $\approx$ 60 nanoseconds. There was no delay between the selected angle of attack and the angle of attack at which the laser pulse was actually seen, which was detected by a photodetector that latched the encoder display when the laser pulsed.

2.5. Experimental Uncertainties

The following are the estimated uncertainties in the various quantities:

Mach number:	± 0.005
angle of attack:	0.1 degrees
normalized pitch rate:	$\pm 0.5\%$ at rates $> 2000^0/sec$
	$\pm 1\%$ at rates $< 2000^0/sec$
C_p:	at M = 0.2, $\pm$ 0.225
	at M = 0.3, $\pm$ 0.075
	at M = 0.45, $\pm$ 0.0375
$\frac{dC_p}{d(x/c)}$	± 10

The uncertainty in C_p is estimated to be 1 fringe for the flow in general with about 3 fringes possibly undetectable for the peak suction pressure coefficient.

3. Results and Discussion

The pressure distributions derived from an analysis of the interferogram images will first be presented along with a qualitative discussion of representative images used as flow visualization. A discussion of the leading-edge pressure gradients calculated from the pressure distributions will follow. Comparisons will

be made between results obtained on an untripped and a tripped airfoil.

3.1. Interferogram Images and Pressure Distributions

Analysis of untripped airfoil[3] steady - and unsteady - flow[3] interferograms of the airfoil flow field while the airfoil rapidly pitches from 0 to 60 degrees angle of attack has shown that a leading-edge laminar separation bubble forms in both steady and unsteady flows for all Reynolds numbers of the experiment. Furthermore, for the low Mach numbers studied in the untripped case, the dynamic stall vortex originated just as the bubble burst; the vortex then grew and convected. Tripping the boundary layer ensured that the flow was turbulent from the origin of the trip, which means that a laminar separation bubble could not form. The result of tripping the boundary layer is illustrated in Fig. 2 for the conditions M = 0.3, $\alpha = 11^0$ and a nondimensional pitch rate of $\alpha^+ = 0.04$. Enlarged interferogram images of the leading-edge region for the untripped and tripped cases are presented in Figs. 2a and 2b, respectively. The instantaneous pressure coefficient distributions which were derived from these images are given in Fig. 2c. For both cases a peak suction pressure coefficient of $C_p = -3.4$ was measured, with the location of the suction peak in the tripped case shifted slightly downstream of the location of the peak in the untripped case (from x/c = 0.013 to x/c = 0.018). The laminar separation bubble appears in the untripped airfoil data as a plateau in the pressure coefficient plot which extends from $x/c \approx 0.025$ to $x/c \approx 0.055$.

The evolution of the dynamic stall vortex was greatly affected by the trip, as is illustrated in Fig. 3. Again for the conditions M = 0.3, $\alpha^+ = 0.04$, the earliest stage of dynamic stall vortex development began for the untripped airfoil as the airfoil passed instantaneously through the angle $\alpha = 15^0$, as can be seen in the interferogram shown in Fig. 3a. Here, the early stages of vortex development on the untripped airfoil is indicated by the opening of the separation bubble, which is made evident by the change in curvature of the fringes at the downstream end of the bubble (compared to Fig. 2a, where the fringes of the closed bubble meet the airfoil normal to the surface). In contrast, however, as the tripped airfoil passed this angle (Fig. 3b) the vortex had already grown considerably and covered the first 25% of the airfoil chord. The growth of the vortex can also be seen in the pressure coefficient distributions shown in Fig. 3c. As the vortex forms, the pressure coefficient distribution begins to 'lift' up along the suction surface, and as the vortex grows in extent and convects downstream, the increased region of suction along the upper surface results in the vortex lift of dynamic stall.

The development of the pressure coefficient distribution over the angle of attack range of $\alpha = 7^0$ to $\alpha = 17^0$ is shown in Fig. 4 for both the untripped and tripped airfoils for the conditions M = 0.3 and $\alpha^+ = 0.03$. The separation bubble, which began to develop at $\alpha \approx 9^0$ on the untripped airfoil (Fig. 4a), is clearly absent on the tripped airfoil (Fig. 4b). Further, for angles of 13 degrees and above (Fig. 4c and 4d) the untripped airfoil has developed a stronger suction, while the tripped airfoil stalled at approximately one degree lower angle of attack than the untripped airfoil (14^0 *vs* 15^0) as can be seen clearly by comparing Figs. 4c and 4d. In addition, the location of the suction peak moved slightly downstream for the tripped airfoil with increasing angle of attack, unlike that for the untripped case, where it moved towards the leading edge.

At higher subsonic free stream Mach numbers the leading-edge flow can become locally supersonic. In the case of the untripped airfoil it was shown[2,3] that multiple λ−shocks formed near the leading edge over the suction surface for freestream Mach numbers above $M \approx 0.4$. In contrast however, at most only two shocks were observed on the tripped airfoil at M = 0.45, indicating that forcing transition has dramatically altered the boundary layer/shock interaction physics. Interferograms of the untripped and tripped flows are shown in Fig. 5a and 5b, respectively, for the conditions of M = 0.45, $\alpha = 11^0$ and a nondimensional pitch rate of $\alpha^+ = 0.025$. A total of five shocks formed on the untripped airfoil for these conditions with the final shock occurring at nearly 10% of the chord from the leading edge. Only two shocks occurred in the tripped flow, with the final shock located near the downstream end of the trip at about the 3% chord point. Fringe counting showed that for the untripped flow, the local Mach number was supersonic until a height of about 2% chord above the airfoil surface, and the maximum Mach number was about 1.25. On the other hand, the supersonic region for the tripped airfoil extended to 1% chord above the airfoil and the Mach number was also lower at about 1.1. In both cases, the supersonic flow transitioned to the outer subsonic flow through a compression wave, through which the interference fringes were found to bend. The Mach number where this bending effect was masked was about 0.85. The location of the shocks in relation to the trip is illustrated more clearly in Fig. 5c, a composite of data obtained from digitized images of the trip and of the interferogram shown in Fig. 5b. The bold lines in this figure represent the supersonic flow and the dashed lines, the remainder of the compression waves.

Another striking feature seen in both the interferograms of Fig. 5 is the appearance of the vertical fringes following the last shock. In Ref. 3, this was shown to be associated with the first indication of the onset of dynamic stall. The studies reported in Ref. 3 also showed that even after the dynamic stall vortex formed (near the end of the bubble), the leading edge pressure coefficient remained large, until the influence of the vortex was felt near the leading edge. After this event, the pressure coefficient dropped rapidly as the vortex began to convect. In the higher Reynolds number experiments of McAlister et al[14], dynamic stall onset was said to correlate with the loss of the suction peak. However, the present interferometry studies seem to define stall onset more precisely. Fig. 5b shows the presence of the vertical fringes clearly and a slight reversed flow[3] is seen for $0.03 \leq x/c \leq 0.06$. Fringes pointing upstream in a thin layer of fluid below the separated shear layer are evidence of the locally reversed flow. This leads one to infer that that the dynamic stall process is under way - even though

there is a shock still present above the shear layer. On the other hand, although the vertical fringes are seen for the same experimental conditions of M = 0.45 and $\alpha = 11^0$ for the untripped flow, dynamic stall has just been initiated, since the region of reversed flow is still not easily discernible. Because the dynamic stall vortex originates at x/c $\approx$ 0.1, a definite delay exists between when the vortex forms (either because of the bursting of the laminar separation bubble or due to shock induced separation) and when its influence reaches the leading edge. During this time, the airfoil could continue to develop suction as the angle of attack is increased. This difference in the dynamic stall onset location between the two flows explains why the tripped airfoil flow stalls at a slightly lower angle of attack than when it is not tripped.

3.2. The Peak Suction Pressure

As mentioned earlier, the suction pressure reaches a maximum value just prior to dynamic stall onset; during the period while the dynamic stall vortex is growing, the suction remains high and then drops sharply once the vortex begins to convect. The peak suction pressure coefficient reached is shown in Fig. 6 for different nondimensional pitch rates and Mach numbers. Plotted for comparison on the same graph are the results obtained previously[3] for the untripped airfoil. In both cases, the peak suction pressure coefficient decreased dramatically with increasing Mach number, due to the increasing compressibility effects on the flow. This effect is seen in Fig. 6 for the tripped airfoil as a generally monotonic increase in the peak suction pressure coefficient with increasing nondimensional pitch rate. For the untripped airfoil, however, the peak suction pressure coefficient tended to be relatively independent of nondimensional pitch rate for $\alpha^+ > 0.03 (> 0.02$ for M = 0.45). This independence of the peak C_p on nondimensional pitch rate (for high pitch rates) in the untripped flow was presumably due to the presence of the separation bubble; the change in the shape of the enveloping streamline due to the presence of the bubble altered the inviscid/viscous interaction, and eventually limited the growth of the suction peak so that increasing the pitch rate further had no effect on the peak suction level reached.

The peak C_p tended to be less for the tripped airfoil than for the untripped airfoil for the same experimental parameters at Mach numbers $\geq$ 0.3. At the low Mach number of 0.2 the difference is represented by a single fringe in the interferograms; therefore, within the accuracy of the image analysis the peak C_p value was unaffected by the trip for this case. For the higher Mach number flows, where compressibility effects dominated, the difference was significant; five or more fringes for M = 0.3 which corresponded to $\Delta C_p > 0.81$, and four or more fringes for M = 0.45, or $\Delta C_p > 0.28$. The differences in the behavior seen for the different Mach numbers are typical of this flow since compressibility effects set in at M = 0.3[2].

3.3. The Adverse Pressure Gradient

The nondimensional adverse pressure gradient following the leading-edge suction peak was determined from the pressure coefficient distributions obtained from the analysis of the interferogram images by performing a linear least squares fit to the first three or four data points following the highest pressure coefficient value measured. As an example, Figs. 7a and 7b show the leading-edge instantaneous C_p distributions on the suction surface of the untripped and tripped airfoils, respectively, for the angles $\alpha = 12^0$, 13^0, and 13.5^0 at M = 0.3 and $\alpha^+ = 0.03$. Indicated on each curve is the straight line segment used to estimate the value of the pressure gradient $\frac{dC_p}{d(x/c)}$. No fit was performed for the $\alpha = 13.5^0$ data of the untripped case since only two fringes were detected in the adverse pressure gradient upstream of the separation bubble; often at higher angles no fringes are detectable in the suction peak. For the tripped airfoil flow (Fig. 7b), the dramatic change in the pressure distribution and the gradient which occurred between the angles $\alpha = 13^0$ and $\alpha = 13.5^0$ was a result of the formation and convection of the dynamic stall vortex.

The flattening of the distributions at the top must be commented on since, in general, the pressure coefficient distribution is a smooth and continuous function with a well defined peak. Inherent to the interferometry technique are in-plane deflections of the light rays due to the steep density gradients found at high angles of attack (for example at $\alpha = 12^0$) which have been shown to deflect the image of the beam into the airfoil surface[15], resulting in a reduction of the number of fringes visible. These 'missing fringes' cause the flat distribution and result in an under estimation of the value of C_p at the suction peak. It is also possible that the trip physically obscured some fringes very close to the surface.

The leading-edge adverse pressure gradients for the tripped and untripped airfoils are compared in Fig. 8a for the nondimensional pitch rate of $\alpha^+ = 0.03$, and M = 0.2. Also shown for comparison in Fig. 8b are the peak suction pressure coefficients for each angle of attack. Until the separation bubble formed (at $\alpha \approx 10^0$), the magnitude of the C_p gradient was similar for both the tripped and untripped airfoils. After the bubble formed the value of the gradient rose sharply in the untripped case. For both cases the gradient attained a maximum value about two degrees (of angle of attack) prior to the onset of dynamic stall and remained relatively constant until the onset of stall. As the dynamic stall vortex began to form, the magnitude of the gradient dropped sharply. This sudden drop in the magnitude of the adverse pressure gradient coincided with the initial development of the dynamic stall vortex and the appearance of the vertical fringes in the interferogram images. The drop occurred at $\alpha = 14^0$ for the tripped airfoil and $\alpha = 15^0$ for the untripped airfoil. Two degrees later the leading-edge suction pressure dropped in magnitude (Fig. 8b) and the dynamic stall vortex began to convect downstream.

This general trend, where the magnitude of the gradient stops growing approximately two degrees prior to the onset of stall and then drops sharply as the vortex begins to form, appears to be independent of both Mach number (Fig. 9) and nondimensional pitch rate (Fig. 10) until the local flow becomes supersonic. Figure 9 shows the pressure gradient as a

function of angle of attack for the Mach numbers M = 0.2, 0.3, and 0.45 and the nondimensional pitch rate of 0.03, while Fig. 10 shows the results for several pitch rates at M = 0.3. It is seen in these two figures that the magnitude of the adverse pressure gradient from which the flow can recover increases with increasing unsteadiness and decreases with increasing Mach number. This is consistent with the pitch rate and Mach number effects on the development of compressible dynamic stall which have been reported elsewhere[2,3]. The lack of data for the untripped airfoil at higher angles of attack for M $\geq$ 0.3 was a result of the PDI image distortions (i.e., the 'missing fringes') discussed earlier in this section. The character of the pressure gradient at M = 0.45 is of particular interest. Fig. 9a shows the untripped airfoil results, where the maximum $\frac{dC_p}{d(x/c)}$ experienced a *decrease* with angle of attack, at most, this $\frac{dC_p}{d(x/c)}$ remains constant for the tripped airfoil (Fig. 9b). This result clearly demonstrates the strong influence of compressibility on the flow development, reflecting the impact of the multiple shocks that have been observed at these conditions.

For all the parameters investigated, when the local flow remained subsonic, the untripped airfoil was found to be capable of withstanding a stronger adverse pressure gradient before dynamic stall onset than the tripped airfoil. Likewise, the peak suction pressure at stall was higher on the untripped airfoil than on the tripped airfoil (refer to Fig. 6). It appears that the formation of the separation bubble had a beneficial effect on stall for the conditions of the experiments. Evidence for this conclusion is based largely on the data shown in Fig. 8a, which clearly shows a similar development in the pressure gradient for both tripped and untripped flows at M = 0.2. Moreover, the appearance of the vertical fringes (which signify the onset of stall) coincides with the drop in the magnitude of the pressure gradient where data were available, and occurs two degrees before the drop in peak C_p (which occurs as the vortex convects downstream) for the cases studied. This would indicate that the mechanism of the dynamic stall vortex development was unaffected by the separation bubble at low Mach numbers. The picture is considerably different at higher Mach numbers as discussed in relation to Fig. 5.

3.4. Discussion of the Experimental Observations

The results presented in this paper briefly describe the first effort in assessing the role of transition on the compressibility effects on dynamic stall of pitching airfoils. It was originally presumed that use of a transition trip would render the local boundary layer turbulent and hence, a dramatically different sequence of events of dynamic stall would occur and improved stall characteristics for the airfoil would result. But, contrary to the expected results, a detailed analysis of the interferogram images revealed that the trip for which the data are presented actually caused dynamic stall at lower angles of attack than for the untripped airfoil.

It is to be noted that as shown in Fig. 8a at M = 0.2 and $\alpha^+ = 0.03$, the pressure gradient when the untripped flow first stalls and forms a bubble is about 100, whereas the pressure gradient for the tripped flow at first stall (which is dynamic stall) is about 200. These levels confirm what is expected of the ability of the tripped flow to withstand a larger adverse pressure gradient. In this context, the value of 350 for the pressure gradient at dynamic stall vortex formation for the untripped case seems apparently inconsistent. However, this may not be the case, since the untripped flow originally stalled at a pressure gradient of 100 forming the laminar bubble which changed the pressure distribution over the airfoil. Dynamic stall in this case arose out of the 'failure' of the laminar separation to reattach, thus bursting the bubble[3]. The local pressure gradient at the downstream edge of the bubble was also found to be about 100. Once the stall vortex formed, the gradient dropped sharply. It appears that after the bubble forms, the pressure gradient could still increase, because the separated shear layer could reattach until a certain higher angle of attack. The pressure gradient at stall decreases with increasing Mach number, but the above trend is still valid. At M = 0.45, the vortex forms at a very low value of $\frac{dC_p}{d(x/c)} = 25$ in the tripped flow. Data could not be processed in the untripped flow because of a larger region of the supersonic flow and the more complicated multiple shocks/compression waves interactions affecting the process.

Fig. 10a and 10b show that in steady flow, the tripped airfoil stalls at a lower angle of attack than the untripped airfoil. (Similar effects have been observed elsewhere, cf: the results for the NLR1 airfoil[14] where the tripped airfoil stall is 1 degree lower than the untripped airfoil stall angle) However, even for steady flow, the values of the adverse pressure gradient when the laminar separation bubble forms and when the tripped airfoil stalls are very close (70-100). One factor that could affect this number is the thickness of the trip used. As stated earlier, at 175μm, it was considerably more than the estimated boundary layer thickness of about 60 μm. The trip height was based on recommendations generally given for a flat plate boundary layer. The challenge of finding the 'right trip' for an unsteady flow with a large adverse pressure gradient, locally supersonic flow and in which the transition point moves considerably, is formidable. Further, standard recommendations on trip selection seem to be based on the fact that the boundary layer eventually reaches the equilibrium state. When leading edge separation occurs as in the present dynamic stall flow, this criterion is obviously not satisfied. Also, the stall process is significantly affected by the 'age' of the turbulence in the tripped boundary layer. If the turbulence is 'young' as in the present experiments, major differences could be found for each trip that is used. In fact, the experiments were repeated for an oscillating airfoil with three different trips. Preliminary evaluation of the data showed trends similar to those described in this paper, although the pitch angle was varied in a sinusoidal manner. Further analysis is on-going. A typical plot of C_p *vs.* α for these trips is shown in Fig. 11, in which changes in C_p near stall onset caused by the various trips are clear. This also brings out the extreme sensitivity of the dynamic

stall process to the local flow details. This conclusion will be of great significance in computational modeling of the flow, especially when selecting a turbulence model. Until the computational fluid dynamics models include these complex physical effects, it appears to be unreasonable to expect quantitative agreement between experiments and computations.

4. Concluding Remarks

A study of the role of boundary layer tripping on dynamic stall of a transiently pitching airfoil has been conducted. The following conclusions are drawn from the study.

1. The laminar separation bubble present in the untripped flow was found to have a beneficial effect on dynamic stall delay.

2. Dynamic stall onset moves closer to the leading edge in the presence of a trip, which eventually leads to stall at lower angles of attack (by about 1 - 1.5 degrees) than observed in untripped airfoil dynamic stall.

3. The leading-edge adverse pressure gradient and the peak suction pressure coefficient were lower in value on the tripped airfoil.

4. The behavior of the flow is grossly different under compressibility conditions with a trip. The shock/boundary layer interactions are modified by the trip, as also is the leading edge pressure gradient.

5. The sensitivity of the flow to the state of the boundary layer turbulence points to a need for highly refined computational flow modeling.

Acknowledgements

The project was supported by an AFOSR grant (MIPR-93-0003) to the Naval Postgraduate School and was monitored by Maj. D.B. Fant. Additional support was received by ARO-MIPR-125-93, monitored by Dr. T.L. Doligalski. The work was carried out in the Fluid Mechanics Laboratory Branch of NASA Ames Research Center. The steady encouragement of Dr. S.S. Davis, Chief, FML Branch, the support of Mr. J.D. Loomis in the conduct of experiments and the interferogram processing software development effort of Mr. P.J. Trosin, Sterling Federal Systems, Inc., are greatly appreciated.

5. References

[1]Chandrasekhara, M.S. and Carr, L.W., "Flow Visualization Studies of the Mach Number Effects on the Dynamic Stall of an Oscillating Airfoil", *Journal of Aircraft*, Vol. 27, No. 6, pp. 516-522.

[2]Chandrasekhara, M.S., Ahmed , S. and Carr, L.W., "Schlieren Studies of Compressibility Effects on Dynamic Stall of Airfoils in Transient Pitching Motion", *Journal of Aircraft*, Vol. 30, No. 2, pp. 213-220.

[3]Chandrasekhara, M.S. and Carr, L.W., and Wilder, M.C., "Interferometric Investigations of Compressible Dynamic Stall Over a Transiently Pitching Airfoil", *AIAA Paper 93-0211*, Accepted for publication in *AIAA Journal*

[4]McCroskey, W.J., McAlister, K.W., Carr, L.W., Pucci, S.L., Lambert, O., and Indergrand, R.F., "Dynamic Stall on Advanced Airfoil Sections", *Journal of American Helicopters Society*, Vol. 26, No. 3, pp. 40-50.

[5]Lorber, P.F. and Carta, F.O., "Unsteady Stall Penetration Experiments at High Reynolds Number", AFOSR-TR-87-1202, April 1987.

[6]Carr, L.W., Chandrasekhara, M.S., Ahmed, S., and Brock, N.J., "A Study of Dynamic Stall Using Real Time Interferometry", *AIAA Paper 91-0007*, Accepted for publication in *Journal of Aircraft*.

[7]Gostelow, J.P., Blunden, A.R., and Walker, G.J., "Effects of Free-Stream Turbulence and Adverse Pressure Gradients on Boundary Layer Transition", *ASME Paper No. 92-GT-380*, presented at the International gas Turbine and Aero Engine Congress and Exposition, Cologne, Germany, June 1-4, 1992.

[8]Visbal, M.R., "Effect of Compressibility on Dynamic Stall of a Pitching Airfoil", AIAA Paper No. 88-0132, Jan. 1988.

[9]Chandrasekhara, M.S., Carr, L.W., Ekaterinaris, J.A., and Platzer, M.F., "Interferometry and Computational Studies of an Oscillating Airfoil Compressible Dynamic Stall", Proceedings of *The 5th Asian Congress of Fluid Mechanics*, Vol. 2, pp. 1047-1050, Ed. K.S. Chang and D.H. Choi, Aug. 1992.

[10]Carr, L.W., and Chandrasekhara, M.S., "Design and Development of a Compressible Dynamic Stall Facility", *Journal of Aircraft*, Vol. 29, No. 3, pp. 314-318.

[11]Chandrasekhara M.S., and Carr, L.W., "Design and Development of a Facility for Compressible Dynamic Stall Studies of a Rapidly Pitching Airfoil", *ICIASF'89 RECORD*, IEEE Publication 89-CH2762-3, pp. 29-37.

[12]Brock, N.J., Chandrasekhara, M.S., and Carr, L.W., "A Real Time Interferometry System for Unsteady Flow Measurements", *ICIASF'91 RECORD*, IEEE Publication 91-CH3028-8, pp. 423-430.

[13]Pope, A., and Goin, K.L., *High Speed Wind Tunnel Testing*, Kraeger Publishing Company, New York, NY, 1978.

[14]McAlister, K.W, Pucci, S.L., McCroskey, W.J., and Carr, L.W., "An Experimental Study of Dynamic Stall of Advanced Airfoil Sections, Volume 2, Pressure and Force Data", NASA TM 84245, Sept. 1992.

[15]Cho, Y.C., Carr, L.W., and Chandrasekhara, M.S., "Correction to Fringe Distortion due to Flow Density Gradients in Optical Interferometry" *AIAA Paper No. 93-0631*, presented at the 31st Aerospace Sciences Meeting and Exhibit, Reno, NV, Jan, 11-14, 1993.

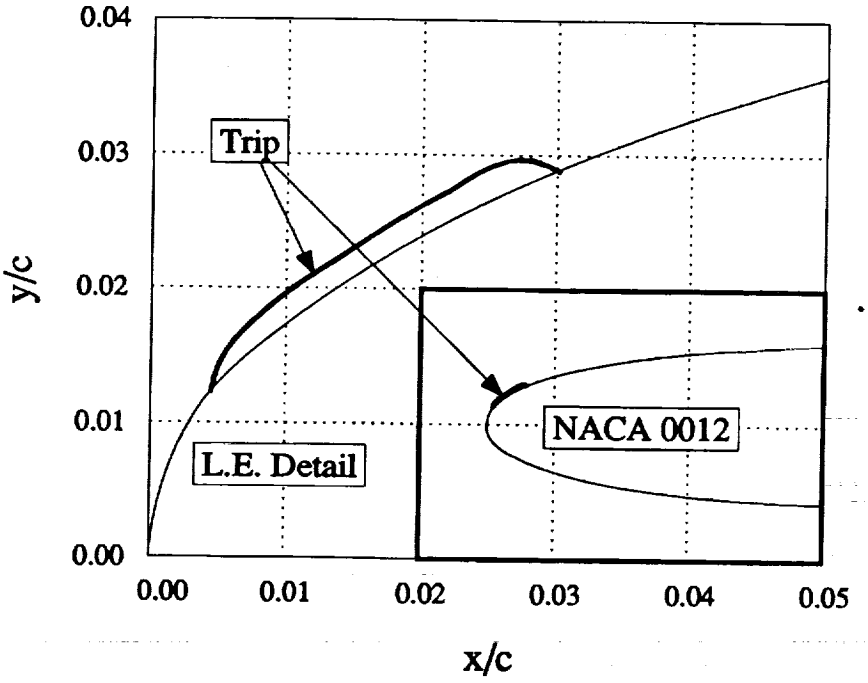

Figure 1. Profile View of the Boundary-Layer Trip. Inset Shows the Leading 25% of the Chord.

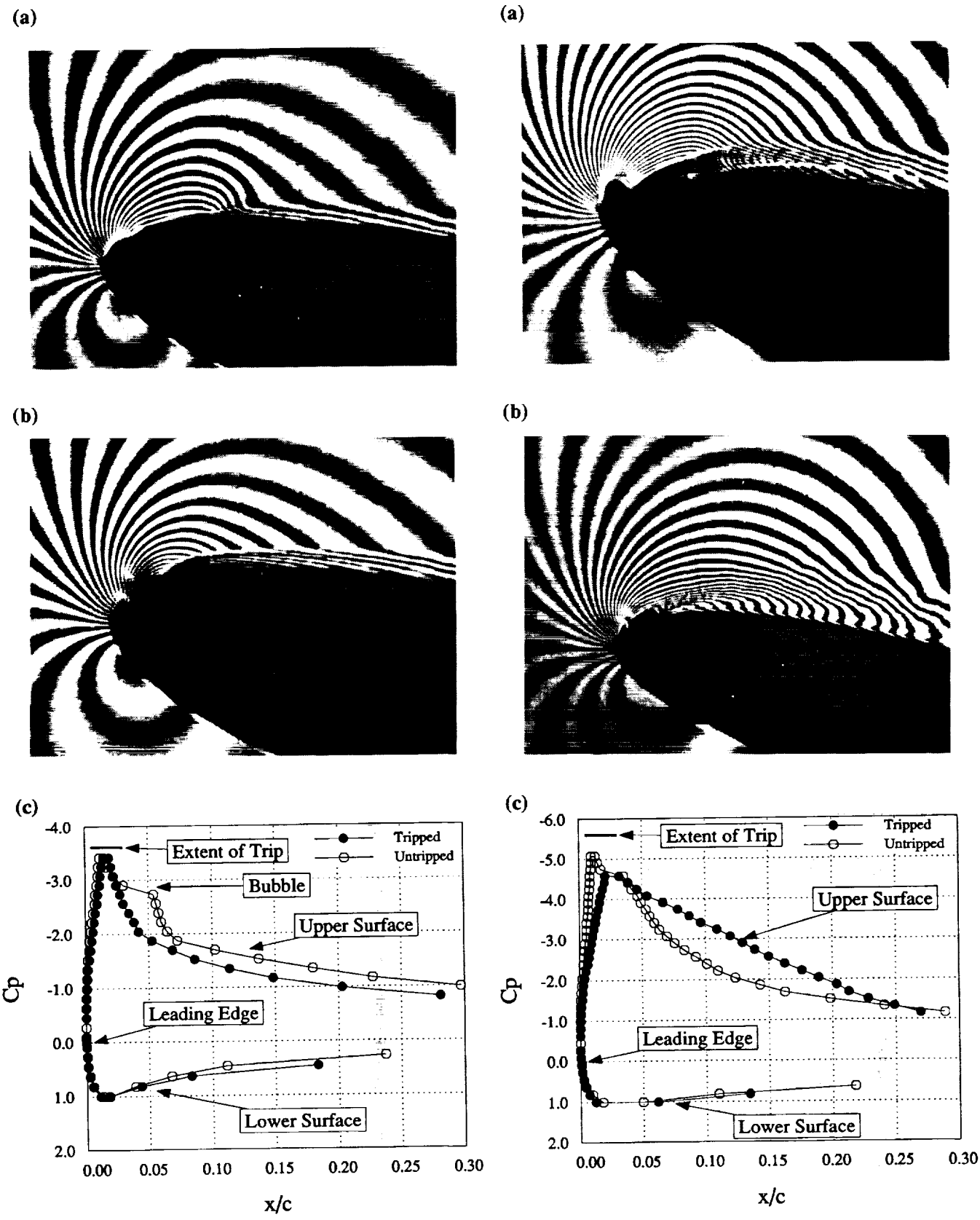

Figure 2. Comparison of Untripped and Tripped Flows, M = 0.3, $\alpha^+ = 0.04$, $\alpha = 11^0$; (a) Untripped Flow Over the First 18% Chord, (b) Tripped Flow Over the First 15% Chord, (c) Pressure Distributions Corresponding to (a) and (b).

Figure 3. Comparison of Untripped and Tripped Flows, M = 0.3, $\alpha^+ = 0.04$, $\alpha = 15^0$; (a) Untripped Flow Over the First 16% Chord, (b) Tripped Flow Over the First 27% Chord, (c) Pressure Distributions Corresponding to (a) and (b).

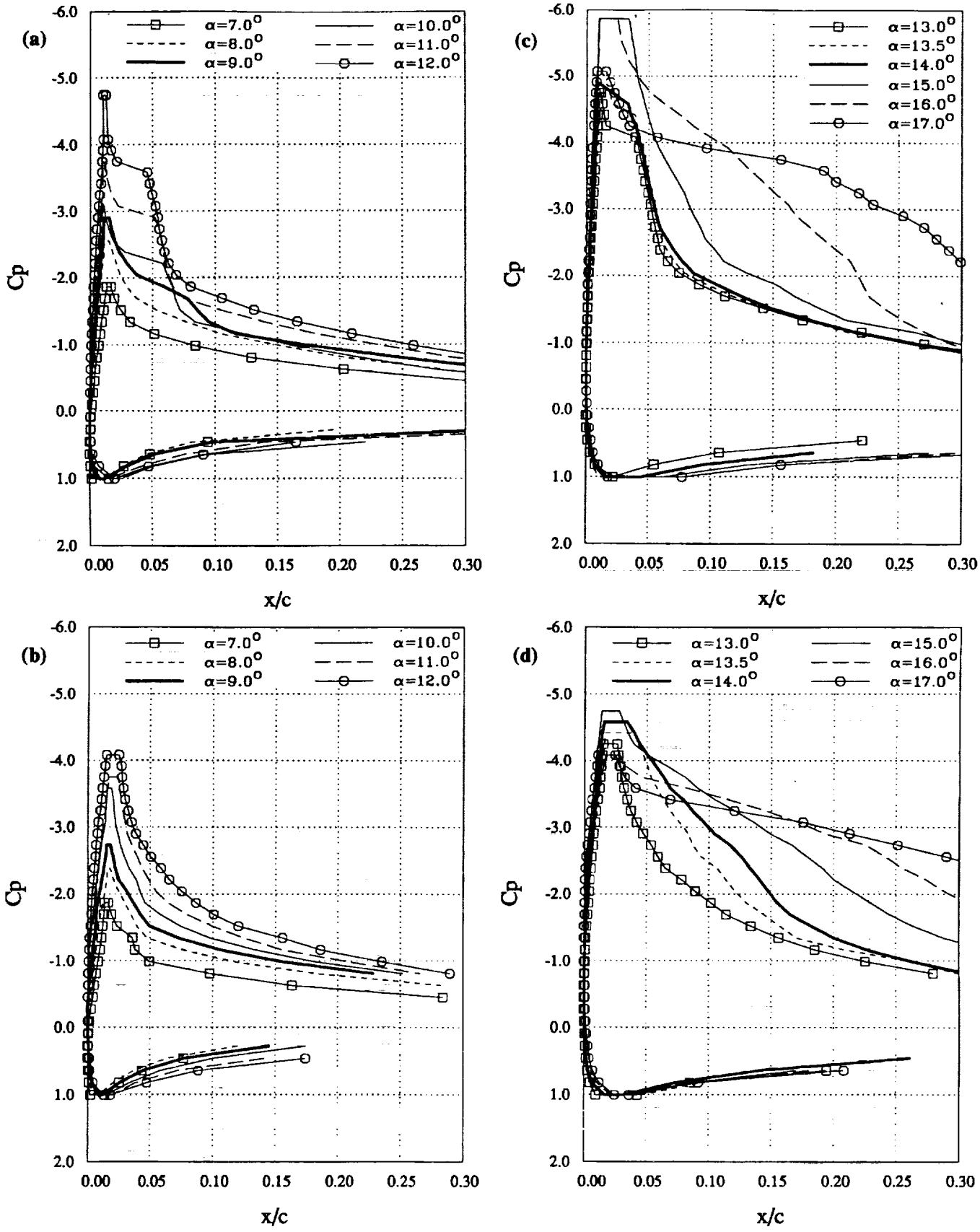

Figure 4. Pressure Distributions over a Transiently Pitching Airfoil, M = 0.3, $\alpha^+ = 0.03$; (a) Untripped, $\alpha = 7^0$ to 12^0, (b) Tripped, $\alpha = 7^0$ to 12^0, (c) Untripped, $\alpha = 13^0$ to 17^0, and (d) Tripped, $\alpha = 13^0$ to 17^0

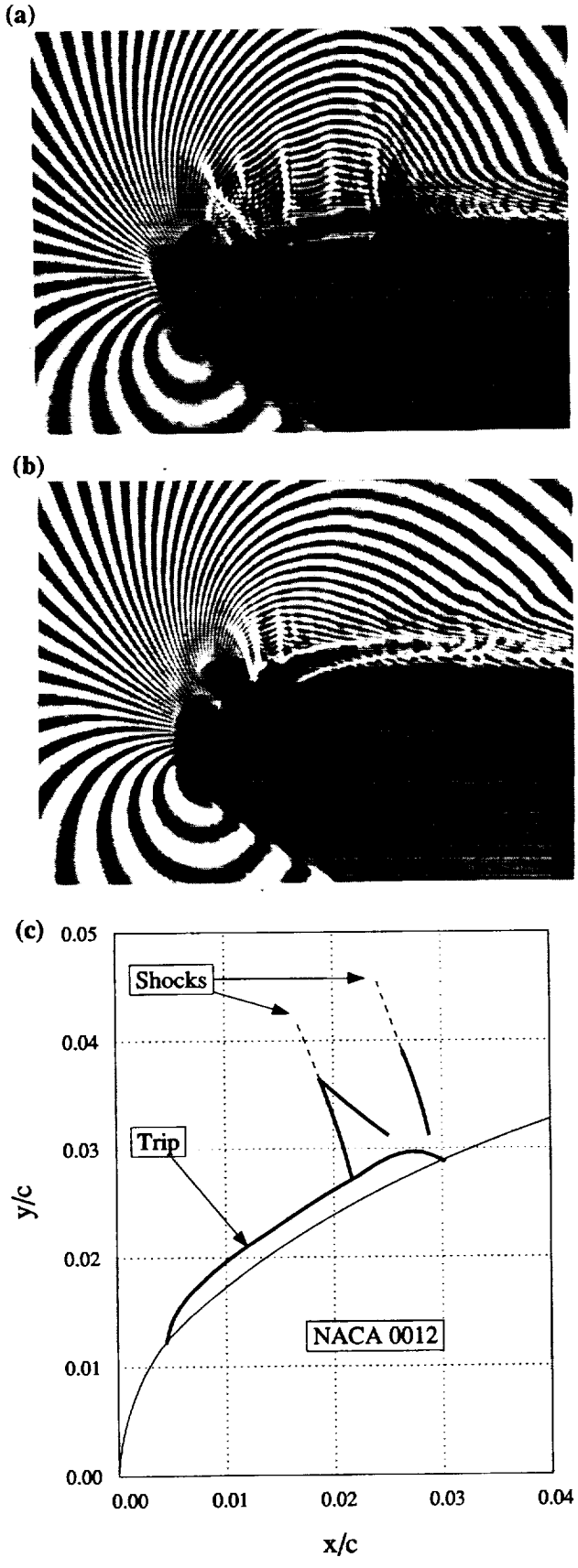

Figure 5. Comparison of Tripped and Untripped Flows Over the First 15% Chord, M = 0.45, $\alpha^+ = 0.025$, $\alpha = 11^0$; (a) Untripped Flow, (b) Tripped Flow, (c) Shock Location Relative to the Trip, Corresponding to Fig. (b).

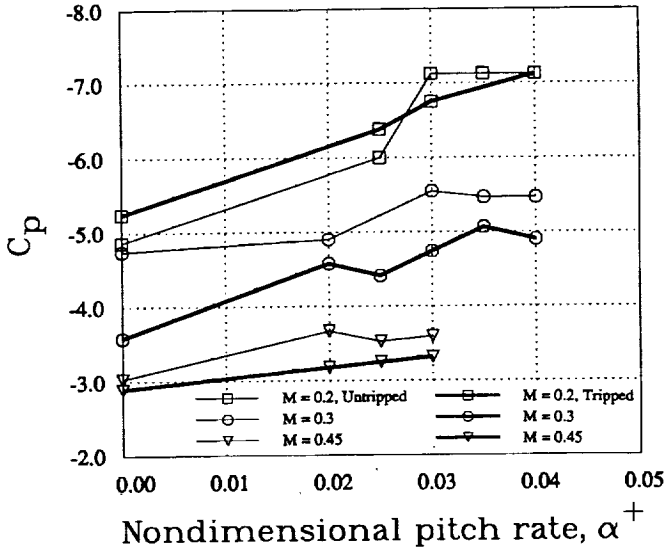

Figure 6. Transiently Pitching Airfoil Peak Suction Pressure Coefficient at Stall Vortex Formation.

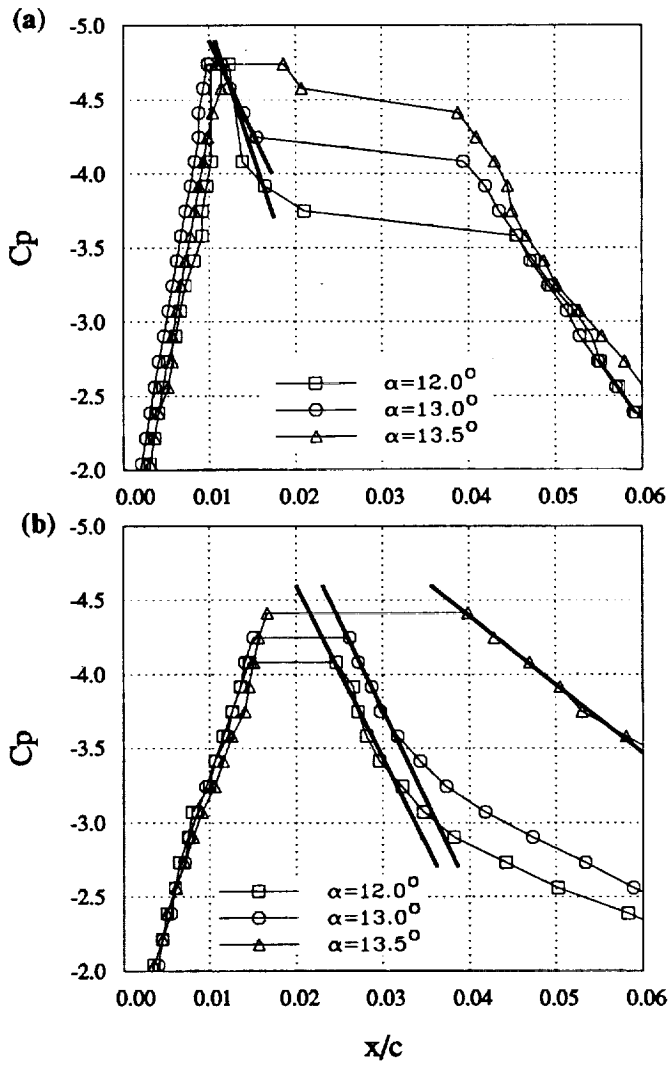

Figure 7. Leading Edge Suction Pressure Distributions, M = 0.3, $\alpha^+ = 0.03$. Slope of Solid Lines Indicates Magnitude of Adverse Pressure Gradient; (a) Untripped, (b) Tripped.

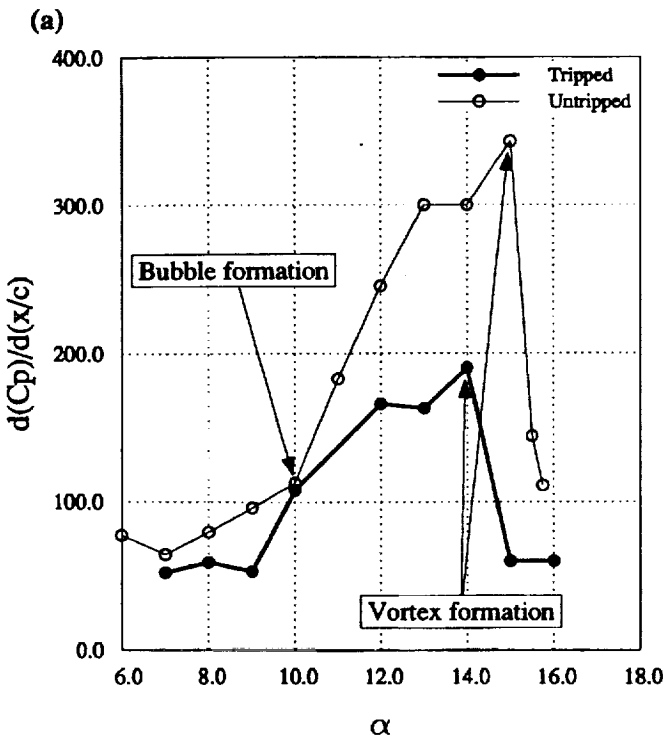

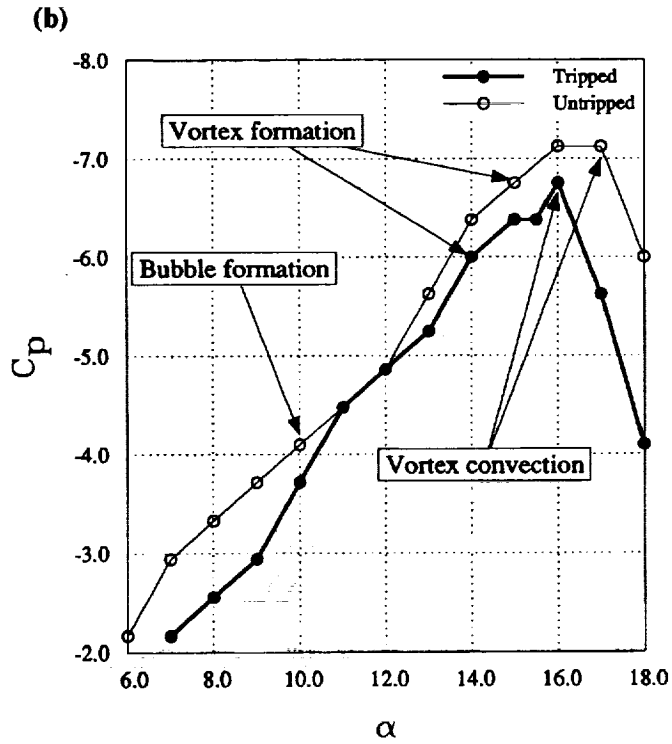

Figure 8. (a) The Development of the Leading-Edge Adverse Pressure Gradient; (b) The Development of the Peak Pressure Coefficient, M = 0.2, $\alpha^+ = 0.03$.

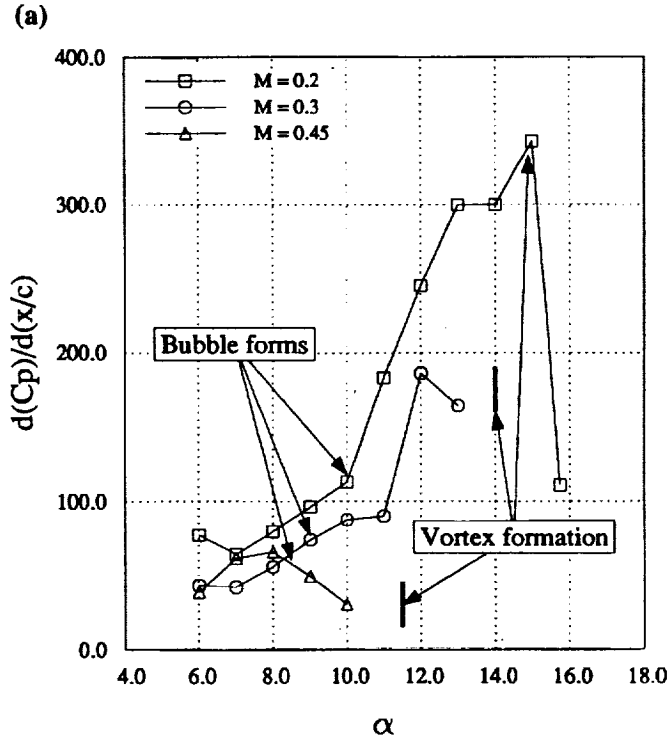

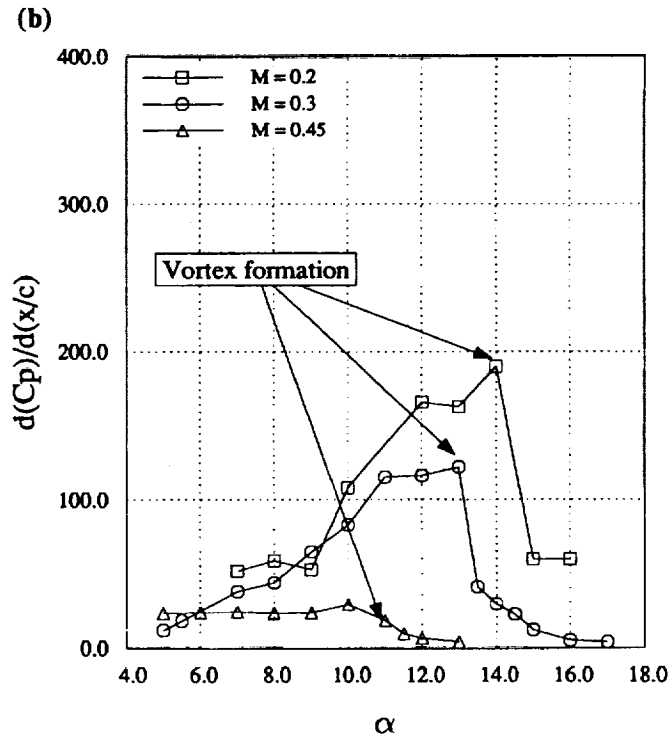

Figure 9. Effect of Mach Number on the Adverse Pressure Gradient Development, $\alpha^+ = 0.03$; (a) Untripped Flow, (b) Tripped Flow.

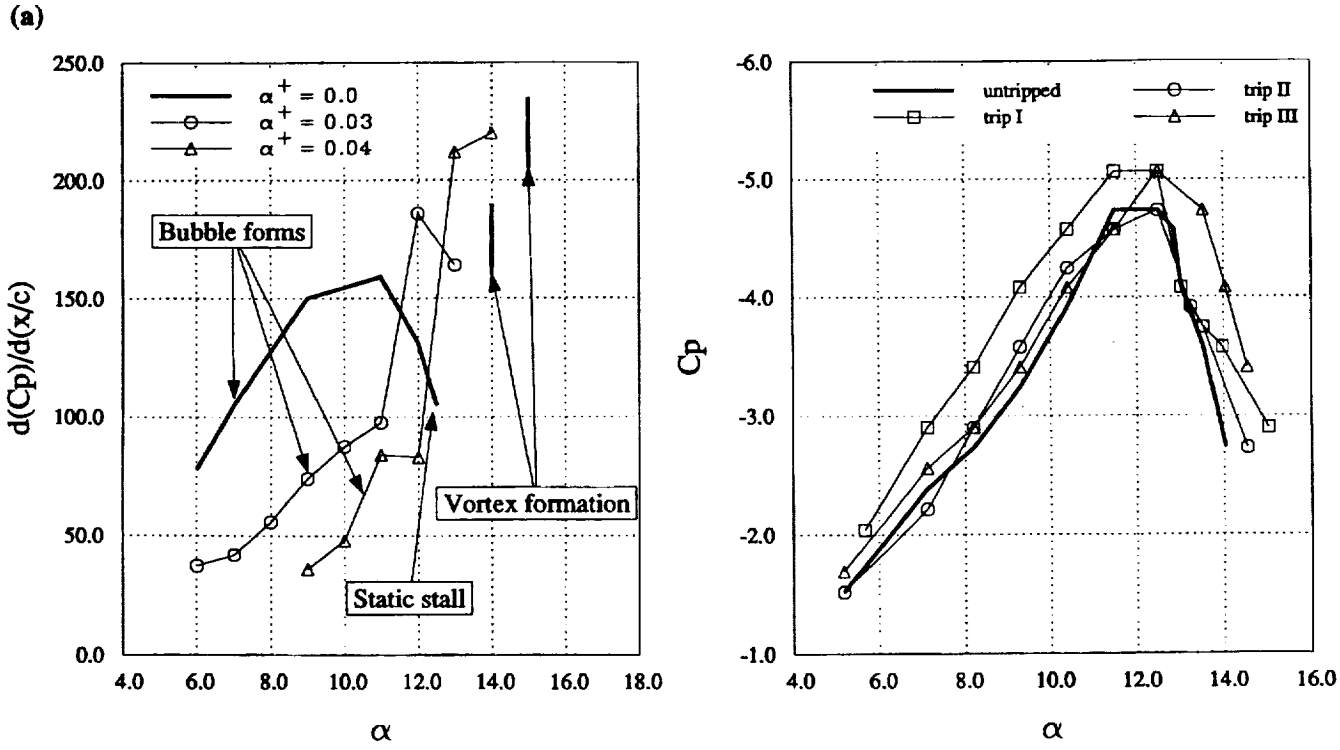

Figure 11. Peak Suction Pressure Coefficient Development over an Oscillating NACA 0012 Airfoil for Various Boundary Layer Trips. M = 0.3, $k = \frac{\pi fc}{U_\infty}$, $\alpha = 10^0 + 10^0 sin\ 2\pi ft$.

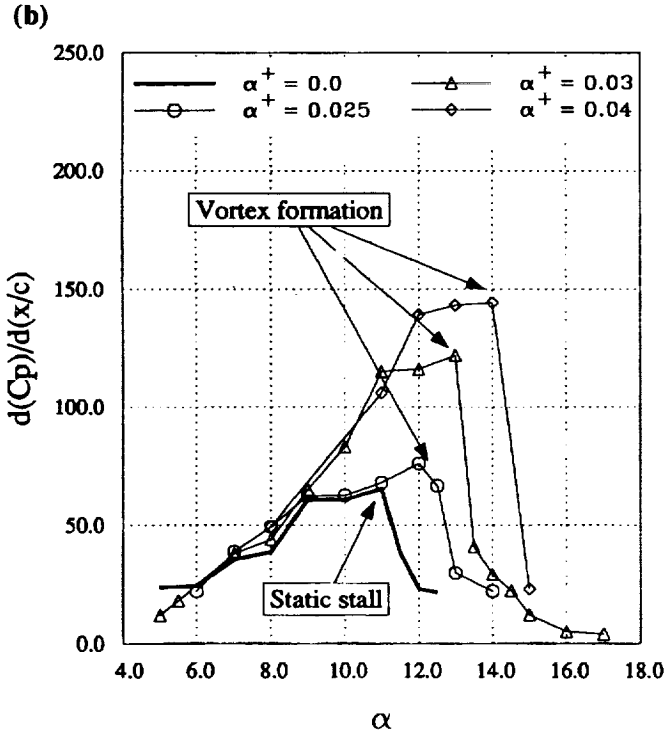

Figure 10. Effect of Pitch Rate on the Adverse Pressure Gradient Development, M =0.3; (a) Untripped Flow, (b) Tripped Flow.

Appendix C:

Boundary Layer Tripping Studies of Compressible Dynamic Stall Flow

AIAA-94-2340
Boundary Layer Tripping Studies of Compressible Dynamic Stall Flow

M.S.Chandrasekhara, Naval Postgraduate School, Monterey, CA;
M.C.Wilder, MCAT Institute, San Jose, CA; and
L.W.Carr, U.S.Army ATCOM, NASA Ames Research Center, Moffett Field, CA

25th AIAA Fluid Dynamics Conference
June 20-23, 1994 / Colorado Springs, CO

Boundary Layer Tripping Studies of Compressible Dynamic Stall Flow

M.S. Chandrasekhara[1,*]
Navy-NASA Joint Institute of Aeronautics
Department of Aeronautics and Astronautics
Naval Postgraduate School, Monterey, CA 93943

M.C. Wilder[2]
Navy-NASA Joint Institute of Aeronautics and
MCAT Institute, San Jose, CA

and

L.W. Carr [3]
Aeroflightdynamics Directorate, U.S.Army ATCOM and,
Fluid Mechanics Laboratory Branch
NASA Ames Research Center, Moffett Field, CA 94035-1000

Abstract

The challenging task of "properly" tripping the boundary layer near the leading edge of an airfoil experiencing compressible dynamic stall has been addressed. Real-time interferometry studies have been conducted on an oscillating airfoil undergoing compressible dynamic stall at free stream Mach numbers of 0.3 and 0.45, by separately placing five different trips of varying sizes. The trip heights ranged from $40\mu m$ to $175\mu m$; the estimated boundary layer thickness was $60\mu m$ at the point of flow separation at a Mach number of 0.3. Quantitative analysis of the interferograms showed that the laminar separation bubble characteristic of low Reynolds number airfoil flows was still present with the smallest trip and premature dynamic stall occurred with the largest trip. A roughness element extending between 0.5% chord to 4% chord from the leading edge and of a height comparable to the boundary layer thickness at the point where the dynamic stall vortex forms was found to be the "right" trip.

Nomenclature

C_p	pressure coefficient
$C_{p_{min}}$	peak suction pressure coefficient
c	airfoil chord
f	frequency of oscillation, Hz
k	reduced frequency $= \frac{\pi fc}{U_\infty}$
M	free stream Mach number
U_∞	free stream velocity
x,y	chordwise and vertical distance
α	angle of attack
α_0	mean angle of attack
α_m	amplitude of oscillation
ω	circular frequency, radians/sec

[1] *Associate Director and Research Associate Professor, Assoc. Fellow AIAA,*

***Mailing Address: M.S. 260-1, NASA Ames Research Center, Moffett Field, CA 94035-1000**

[2] *Research Scientist*

[3] *Research Scientist and Group Leader, Unsteady Viscous Flows, Aeroflightdynamics Directorate, Member AIAA*

1. Introduction

Lift enhancement by unsteady airfoil motion through the production of coherent vorticity is a problem of both fundamental and practical interest. The potential benefits of dynamically delaying stall of an airfoil offers possibilities for expanding the flight envelope of full scale aircraft systems. However, the onset of compressibility effects at even low forward flight speeds complicates the problem of dynamic stall. In addition to introducing some basic fluid physics issues, compressibility promotes stall. The various factors affecting the problem are such that hitherto only wind tunnel experiments have been conducted and flight tests are extremely difficult to perform. With the exception of McCroskey et al [1] and Lorber and Carta[2], the available experiments have been at low Reynolds numbers. The ongoing dynamic stall research in the Navy-NASA Joint Institute of Aeronautics [3,4] is at Reynolds numbers ranging from 360,000 to 840,000. This has shown that dynamic stall of an oscillating (or a transiently pitching) airfoil originates from the failure of the laminar separated flow to reattach as the angle of attack increases, resulting in the formation of the dynamic stall vortex from the bursting of a separation bubble. Since the separation bubble is a consequence of transition of the laminar separated shear layer, it can be concluded that transition physics plays a major role in the dynamic stall process. The ability of a boundary layer to overcome the strong adverse pressure gradient that follows the airfoil suction peak or of a layer of coherent vorticity to remain such without coalescing into vortical structures (flow separation), can be expected to depend on the state of the nascent turbulence in this transitional shear layer. Also the time scales of viscous (vorticity) diffusion and unsteadiness play an important role in the process. Additional complexity is introduced by

the ever changing transition behavior such as reduction of the transition length with increasing pressure gradient[5] (as the airfoil pitches to a higher angle of attack). Thus, it is desirable to remove the effects of transition by pre-determining the transition point and fixing it so that the effects of compressibility due to the large local fluid velocities around the leading edge can be clearly isolated.

Traditionally, fluid dynamicists have tripped the boundary layer in the hope of achieving Reynolds number similarity and remove it as a parameter in low Reynolds number studies. Jones and Williams,[6] after an extensive study of NACA 0012 and RAF 34 airfoils, concluded that at low speeds, these airfoils could be tripped in the same way pipe flows are tripped. However, the stall behavior of a NACA 0012 airfoil changes from that of trailing-edge stall to leading-edge stall when compressibility effects set-in at M = 0.3, making this approach not applicable. The challenge is of course, finding the "right" trip which works satisfactorily over the range of flow conditions of interest. Much of the prior recommendations about the right trips have been based on estimates of the drag coefficient and its behavior[7,8]. Generally, a trip size (height and length) that produces no significant additional drag, but which would still produce a fully developed turbulent boundary layer over the flow surface is chosen. In a way, this approach assumes that the flow attains equilibrium some distance downstream of the trip. However, the choice is not clear when leading-edge stalling airfoils, or flows in which stall originates near the trip location, are to be investigated. This is especially the case for the dynamic stall flow, which is often a leading edge type stall occurring just downstream of the suction peak. Furthermore, a stall vortex develops rapidly over a small angle of attack range with strength depending upon the degree of unsteadiness; thus, the flow is never is in equilibrium. In addition, transition significantly affects the intricate details of the dynamic stall process such as the peak suction development, the maximum adverse pressure gradient before vortex formation, the type of shock/boundary layer interaction in the locally supersonic flow, etc. Preston[9] recommends that any device used for achieving transition close to the leading edge must be considered in terms of both its drag producing and disturbance producing abilities. This is because the effectiveness of the device depends upon the momentum thickness Reynolds number in the laminar boundary layer at the point of tripping. Since there is a minimum value[9] for the momentum thickness Reynolds number for a turbulent boundary layer, the effectiveness of a trip could change with changes in the momentum thickness Reynolds number due to variations in unsteadiness and airfoil angle of attack. Hence, it is not surprising that there is no satisfactory tripping technique to be found in the literature for unsteady flow.

This paper attempts to quantify the dynamic stall process with five different trips and recommends a trip that seems to be the most appropriate for the problem. Experimental results of the flow over a steady and an oscillating NACA 0012 airfoil, obtained using the real-time technique of point diffraction interferometry(PDI) are presented. The flow Mach number was 0.3 and 0.45; the reduced frequency, $k = \frac{\pi f c}{U_\infty}$ was 0.0(steady), 0.05 and 0.1. Measurements of both local and global pressures (density) have been obtained for each trip over the airfoil. The data for the tripped flows have been compared with each other and with that for the untripped airfoil flow. The results are presented in terms of the flow field description as interpreted from the interferograms, the pressure distributions including the variation of the peak suction pressure coefficient, and the pressure gradients. It is hoped that the experimental data produced by this study will serve as bench mark data and help computationalists develop codes incorporating correct dynamic stall physics.

2. Description of the Experiment

A. Facility

The experiments were conducted in the Compressible Dynamic Stall Facility (CDSF) located in the Fluid Mechanics Laboratory (FML) of NASA Ames Research Center. The CDSF is an indraft wind tunnel with a 35cm. X 25cm. test section. The tunnel is connected to a 240,000 CFM, 9,000 HP evacuation compressor that allows continuous running at all flow speeds. The oscillatory motion is produced by a drive system located on top of the test section. It is connected to the test section windows by connecting rods on either side. The windows are mounted in bearings and the airfoil is supported between the windows by small pins providing optical access down to the airfoil surface. A sinusoidal motion of the windows results in a sinusoidal variation of the airfoil angle of attack. Triangular registration markers are placed on the windows such that the line joining the vertical sides of the markers above and below the airfoil surface passes through the 25% chord point.

The drive is equipped with an incremental position encoder which provides instantaneous angle of attack and frequency/phase angle of oscillation of the airfoil. An absolute position encoder indicates the mean angle of attack which can be set from 0 to 15 degrees. The amplitude of oscillation ranges from 2 to 10 degrees and the oscillation frequency from 0 to 100 Hz. The nondimensional flow parameters that can be obtained in the CDSF correspond to those of a helicopter in forward flight and the Reynolds number corresponds to that of a $\frac{1}{7}$th scale model rotor, whose test results are directly applicable to a helicopter rotor. Additional details of the system can be found in Carr and Chandrasekhara[10].

B. Description of The Trips

A review of literature [7,8] was conducted to obtain the first estimate of the required trip size. The leading-edge-stalling NACA 0012 airfoil flow bears considerable qualitative similarity to the flow over a circular cylinder. Therefore, it was decided to use a roughness strip as the tripping device following the recommendations of Nakamura and Tomonari[7]. A formula given in Ref. 8 was used to arrive at the minimum size of the trip for the boundary layer. As reported in Wider et al[11], this formula indicated a grit size diameter of 56 - 89μm (0.0022 - 0.0035in.)

for $0.2 \leq M \leq 0.3$. Boundary layer transition trips were formed by bonding three-dimensional roughness elements in a span-wise strip of height $170\mu m$ along the surface of the airfoil. Wind tunnel tests were performed with this trip in place. The results indicated premature stall,[11] attributable to the large trip height resulting from the fabrication process used. Thus, it became necessary to conduct a systematic investigation and perform tests with different trip heights to identify a trip that yielded acceptable results. A total of five trip configurations having the following characteristics were tested:

Trip 1. 74 - 89 μm diameter carborundum grains (number 220 polishing grit) were bonded to the airfoil surface using a water-soluble-adhesive (Polaroid print-coating material). The strip was located on the upper surface for $0.005 \leq x/c \leq 0.03$. The average height of the trip was 170 μm.

Trip 2. A repeat of trip number 1 using a spray-on enamel lacquer adhesive. The average height of this trip was 100 μm. The lacquer was used for all subsequent trips.

Trip 3. Made of the same materials as trip number 2, this strip covered the entire leading edge starting on the lower surface at $x/c = 0.05$ (near the mean stagnation point) and extending to the upper surface at $x/c = 0.03$. The average height was approximately 130 μm.

Trip 4. A smaller grit material, 22 - 36 μm aluminum oxide particles, was used for trips 4 and 5. Trip number 4 was located on the upper surface, $0.005 \leq x/c \leq 0.03$, like trips 1 and 2. The trip was estimated to be no higher than 43 μm.

Trip 5. The last trip extended from $x/c = 0.05$ on the lower surface around the leading edge to $x/c = 0.05$ on the upper surface. The trip height was approximately 40 - 50 μm.

The trip heights were estimated from digitized airfoil images taken under no-flow conditions by magnifying and scaling the images on an IRIS workstation. The uncertainty in the estimated trip heights is $\pm 10\mu m$. The boundary layer height was estimated to be about $60\mu m$ at the point of flow separation ($x/c = 0.02$ to 0.04).

C. The Point Diffraction Interferometry (PDI) Technique

PDI is a real-time interferometry technique that uses fluid density changes to produce flow interferograms. Fig. 1 shows the schematic of the optical arrangement used. It is similar to a standard schlieren system, with the light source replaced by a pulsed Nd-YAG laser and a predeveloped photographic plate located at the knife edge plane. The principle has been detailed in Ref. 12 and is only briefly described here. A pinhole was created (burned) *in-situ* in the photographic plate by increasing the laser energy, with no flow in the wind tunnel. This served as the point diffraction source for producing spherical reference waves. When the flow was turned on, the cylinder of light passing through the test section experienced phase shifts depending upon the local flow conditions and the beam exiting the tunnel window focused to a slightly larger spot around the pinhole. Since light passing through the pinhole loses all the phase information introduced by the flow due to the spatial filtering characteristics of the pinhole, a reference wave is created in the light beam passing beyond the pinhole. This reference wave subsequently interfered with light that was transmitted around the pinhole through the photographic plate, producing interference fringes in real time at the image plane of the optics system. In operation, the laser was triggered stroboscopically, in a manner similar to that used in schlieren studies. No delays could be detected between the events of triggering the laser and the resulting laser light flash even at the highest frequency of oscillation tested.

D. Image Processing

The analysis of the interferograms was conducted with software developed in-house for the purpose. The surface pressure distributions were obtained by determining the fringe intersections with the airfoil contour. The pressure field was obtained by mapping the fringes in the images. For both, digitized PDI images are required as input. Using isentropic flow relations, the fringe numbers and hence, the fluid densities were converted to pressure coefficients. This assumption was used even for the boundary layer and through the dynamic stall vortex. However, it is believed that substantial errors are not introduced in the pressure field, since the entropy change is generally small, until deep dynamic stall occurs.

E. Experimental Conditions

The experiments were conducted on a 7.62cm chord NACA 0012 airfoil. Results will be presented here for flow Mach numbers of 0.3 and 0.45. The corresponding Reynolds numbers were 540,000 and 810,000 respectively. In addition to steady flow data, unsteady flow data was obtained for $k = 0.05$ and 0.1 at $M = 0.3$ and for $k = 0.05$ at $M = 0.45$, for the untripped airfoil and for each of the tripped airfoils. The airfoil was oscillated about the 25% chord point, with its angle of attack varying as $\alpha = 10^\circ - 10^\circ \sin \omega t$. A large number of interferograms were obtained at close intervals depending on the event being imaged. The interval was less than 0.1 degrees (one encoder count) during initiation of the dynamic stall process.

F. Experimental Uncertainties

The estimated uncertainties are as follows:

Mach number:	± 0.005
angle of attack:	0.05 degrees
reduced frequency:	0.005
$C_{p_{min}}$:	$\pm$ 0.075 at M = 0.3
	$\pm$ 0.0375 at M = 0.45
$\frac{dC_p}{d(x/c)}$	± 15

The uncertainty in C_p depends on the fringe number under consideration and is estimated to be 1 fringe for the flow in general with about 3 fringes possibly undetectable near the suction peak.

3. Results and Discussion

A large number of interferograms were obtained and analyzed. Only typical photographic images will

be presented here; the results from the others have been included in graphs to be discussed in this section.

A. Qualitative Flow Description

Figure 2 presents the PDI images at $\alpha = 10^0$ for the untripped airfoil and for trips 3, 4 and 5 for M = 0.3 and k = 0.05. The fringes seen are constant density contours. In all images, the stagnation point is enveloped by the fringe closing around itself near the leading edge on the lower surface. Near the leading edge, the rapid fluid acceleration causes a large density change resulting in a large number of fringes which radiate outward. For the untripped case, Fig. 2a, some of these fringes become parallel to the upper surface immediately after the suction peak and then turn sharply towards the surface. Based on past studies[13] this fringe pattern indicates a laminar separation bubble. The fringes turn sharply again as they merge with the redeveloping boundary layer. In Fig. 2b and 2c, the above mentioned pattern is not seen; the conclusion is that no laminar separation bubble is present in these cases since the fringes merge gradually with the boundary layer. The pressure distributions corresponding to these images (to be discussed in Sec. 3.B.3) show a plateau for the untripped case which is absent in those for trip 4, pointing to the absence of the bubble with trip 4. Elimination of the bubble confirms the functional effectiveness of trip 4. Fringes in Fig. 2d for trip 5 exhibit a pattern indicative of the presence of the bubble although its length is clearly smaller compared to that seen in Fig. 2a.

Figure 3 shows the flow details at $\alpha = 14^0$ when the dynamic stall process is in its beginning stages for the tripped cases. For the case of the untripped flow (Fig. 3a), the dynamic stall process is well under way by this angle and the center of the dynamic stall vortex has moved to about 25% chord location (its downstream edge has reached the 50% chord location). On the other hand, in case of trip 3 (Fig. 3b), the process appears to have only just been initiated. This is indicated by the appearance of vertical fringes near the leading edge (Ref. 14). The outer fringes take a sharp turn towards the trailing edge at around x/c = 0.35, but the inner fringes are normal to the surface close to the leading edge. Beyond x/c = 0.05 they are oriented towards the trailing edge in general. For the case of trip 4 (Fig. 3c), this turn in the outer fringes occurs at x/c = 0.25 and the inner fringes still show a gradual variation in their orientation. A close examination reveals that only a few fringes have become vertical and hence, the dynamic stall process is still beginning. Trip 5 (Fig. 3d) shows an evolution which is midway between that of trips 3 and 4.

B. Quantitative Flow Analysis

1. Comparison of Trip Performance

Figure 4a shows the airfoil peak suction pressure coefficient, plotted vs. angle of attack, for the untripped airfoil and for trips 2, 3, 4, and 5 in steady flow at M = 0.3. The untripped airfoil experiences abrupt leading-edge stall at $\alpha = 12$ deg. as seen by the abrupt loss of leading-edge suction. The airfoil with trip 2 or trip 3 is unable to develop the high levels of suction expected of a "turbulent" flow. Also, the peak suction level reaches a maximum value at $\alpha = 10$ deg. and then falls gradually, indicating a very different type of stall; resembling that of a trailing-edge-stalling airfoil. This radical change in steady stall behavior demonstrates the sensitivity of the flow to the design of the tripping mechanism and points to the need for properly tripping the airfoil. The performance of the airfoil with trip 4, as measured by the production of higher suction peaks as a function of angle of attack, is distinctly superior relative to its untripped counterpart. Eventually, at $\alpha = 11.6$ deg., the highest value of C_p = -5.2 is reached, (slightly higher than the $C_{p_{min}} = -4.9$ obtained with the untripped airfoil) before the airfoil experiences abrupt leading-edge stall. The performance for trip 5 is worse than that of the untripped airfoil. Since a separation bubble still forms in this case, trip 5 is deemed not to have worked for the purpose. It is very interesting to note that this trip does not suppress the bubble, even though it was in place starting at the stagnation point. It appears from this figure that the flow over the airfoil with trip 4 experiences a slightly greater acceleration, more like what is expected of turbulent flow. Still the increase is marginal and it is difficult to draw definitive conclusions from the information presented in this plot alone.

Figure 4b provides similar information when the airfoil is oscillating at a reduced frequency of 0.1 for the airfoil with no trip, and with trips 2, 3 and 4. It is clear that with trip 4, the airfoil develops suction peaks which are much higher than for the other cases plotted. Trips 2 and 3 cause the airfoil performance to be worse than without the trips until dynamic stall develops. In the case of trip 4, the $C_{p_{min}}$ values continue to increase to about -6.3 at $\alpha = 13.5$ deg. when the dynamic stall process begins. The suction peak remains at this level during the process of dynamic stall vortex formation[14] and drops only after the vortex begins to convect. For the untripped airfoil, the vortex forms at slightly lower angles of attack (approximately 12.5 deg.) and at a much lower suction peak of -5.4. Thus, a delay of stall and an increase of suction level are both achieved with trip 4 on the airfoil leading to the conclusion that the boundary layer was successfully tripped.

Trip 4 was successful even at M = 0.45. The unsteady flow peak suction pressures plotted in Fig. 5 for a reduced frequency of 0.05 show that the airfoil with trip 4 consistently produced higher levels of suction than the untripped or trip 5 airfoils. Beyond an angle of attack of 8.5 deg. trip 5 showed a small bubble. It is further interesting to note that all three flows attained values of $C_{p_{min}}$ larger than the critical C_p value of -2.7 for M = 0.45; thus, the flow was locally supersonic in all three cases. But, the highest $C_{p_{min}}$ value was found with trip 4 and thus, the supersonic velocities were the largest in this case.

2. Airfoil Pressure Distributions

The pressure distributions over the airfoil for M = 0.3 and k = 0.05, obtained by image processing of the interferograms, are plotted in Fig. 6a; where the surface C_p for untripped flow and for trip 4 at $\alpha = 10.65^0$ are shown. The plateau seen for the un-

tripped flow is caused by the presence of the bubble. The distribution for trip 4 shows a higher peak of C_p = -4.5 and a gradual fall from the peak. This is consistent with the observations made while discussing Fig. 2 and 3 and with Ref. 11. Interestingly, the suction peak shifts slightly downstream when a trip is present, an indication that the outer potential flow is somewhat modified, even though the trip is physically very small. The most dramatic differences are seen between the leading edge and x/c = 0.1. Fig. 6b is drawn for M = 0.45 and k = 0.05 at α = 7.97 deg. Once again, the presence of the bubble is clearly seen for the untripped flow, and it is absent in the case of the airfoil with trip 4 on it. The larger differences in this higher Mach number flow imply that the viscous/inviscid interactions are considerably affected by the presence of the bubble, reducing its ability to generate higher levels of suction and thus, dynamic lift.

3. Role of Adverse Pressure Gradient

Separation in both steady and unsteady flows is influenced by the state of the boundary layer and the magnitude of the adverse pressure gradient to which the boundary layer is subjected. In order to study the flow in greater detail, the adverse pressure gradients for each flow condition was determined by fitting a curve to the measured pressure distributions and obtaining an average pressure gradient over several points. (See Wilder et al [11] for full details of the procedure). It should be noted that any method of adverse pressure gradient determination inherently yields noisy data with large uncertainty, since numerical differentiation is involved. Furthermore, it is difficult to precisely detect the origin of the fringes on the airfoil surface due to the presence of the trip itself and the locally high fringe density. Thus, small changes in the streamwise location of the fringes could produce large differences in the pressure gradient, despite the care taken during the process. However, this process, while subjective, is internally consistent and hence the results are useful.

The nondimensionalized adverse pressure gradient is plotted against angle of attack for the untripped airfoil and for the trip 4 flow at M = 0.3. Similar data are available for the other trip flows as well. Since trip 4 was found to be the most satisfactory, the comparison of only the results for this trip with that of the untripped airfoil flow are presented. For the steady flow data shown in Fig. 7a, a laminar separation first occurs at α = 6 deg. when the local adverse pressure gradient is about 30. The flow reattaches by natural transition and static stall develops at α = 12 deg. when the pressure gradient reaches a value of about 170. With trip 4 on the airfoil, static stall occurs when the pressure gradient becomes about 125, somewhat below the value for the untripped airfoil case. In the untripped unsteady flow at k = 0.05, Fig. 7b, laminar separation occurs at around α = 8 deg. and dynamic stall occurs at α = 12.5 deg. The trip 4 flow appears to sustain higher adverse pressure gradients throughout the range of angles of attack considered and dynamic stall eventually sets in when the pressure gradient value is about 150 at α = 13.5 deg. At k = 0.1, the results in Fig. 7c show a trend similar to that observed in Fig. 7a; the pressure gradient at laminar separation is about 40 and dynamic stall pressure gradient is about 140 for the untripped airfoil flow. For the trip 4 flow, the pressure gradient at stall is about 110 and a definite stall delay is observed. Although at first the untripped airfoil may appear to be better in withstanding higher pressure gradients than the tripped airfoil, it should be noted that the untripped airfoil experienced laminar separation at a very low pressure gradient (of around 30-40) in laminar flow. The resulting bubble due to transition occurring naturally altered the overall pressure distribution. The reattachment in the back end of the bubble also resulted in a different state of turbulence for this case. Thus, it appears that the formation of the bubble may in fact have a beneficial effect and is fortuitous to the flow. The drag introduced by the placement of any trip increases the momentum thickness (Preston[9]), reduces the energy available to overcome the adverse pressure gradient, possibly resulting in separation at lower values of the pressure gradient. In the comparison of the trips, it was found that although the separation pressure gradient was a little lower than that for the untripped flow, trip 4 seems to be the best in simulating higher Reynolds number, since the most improvement in suction levels, and hence lift, was achieved with it. This analysis demonstrates that when selecting a proper trip for the purpose, in the absence of other information such as turbulence and wall shear data, the elimination of the bubble and evaluation of the pressure gradient could be used to assess the effectiveness of the trips. The differences between even similar roughness trips (for example trips 4 and 5) demonstrate that the state of turbulence is a major factor in providing the boundary layer the ability to overcome the forces causing unsteady flow separation.

4. Global Pressure Distributions

Figures 8a and 8b present the global pressure data obtained by fringe tracing at α = 14 deg. for k = 0.05 and M = 0.3 for the untripped airfoil and for trip 4 corresponding to the interferograms in Fig. 3. The results are a quantification of the statements made in Sec. 3.A. In addition to the differences in the peak value of the suction pressure coefficient (-3.89 for untripped and -5.9 for trip 4) the entire flow field is very different. This can be seen by following the highlighted lines in the figures. As stated earlier, these differences can be attributed to the different state of turbulence in the *initial or early* "turbulent" boundary layer in the two cases.

Fig. 9 compares the pressure fields at α = 10 deg. for M = 0.45 and k = 0.05 for the cases when the interferograms showed multiple shocks. The long sequence of multiple shocks (shown by dotted lines nearly normal to the airfoil upper surface) characteristic of laminar flow untripped airfoil dynamic stall[14] was not found for the trip 4 flow. Although a closer examination of Fig. 9b reveals two shocks (discontinuities in the fringe contours), they do not appear to be strong despite the larger Mach number (C_p = -3.84) closer to the airfoil. Fig. 9c clearly shows that the flow has not fully transitioned with trip 5, since the fringe pattern compares reasonably with that of

the untripped airfoil flow. The supersonic region for the untripped airfoil is much flatter than that for the trip 4 flow. The isentropic flow assumptions used limit quantifying the flow details locally between the shocks, but it is clear that despite the larger suction levels in case of trip 4 flow, the shocks seen in the supersonic flow region have not induced flow separation. This flow behavior indicates that the flow is more akin to turbulent flow and is similar to the turbulent flow dynamic stall computational results of Visbal[15], and Ekaterinaris[16]. These results affirm that the state of the turbulence in the "turbulent" boundary layer plays a very definite role in affecting the dynamic stall process.

4. Concluding Remarks

1. A systematic investigation of the effects of tripping an airfoil boundary layer has been conducted to determine an effective trip for leading-edge stalling compressible dynamic stall flows.

2. The study shows that a trip that is made up of small scale roughness, distributed over a height comparable to the boundary layer height at the point of separation, seems to be the optimum in these complicated flows.

3. Furthermore, the state of turbulence influences the unsteady separation process considerably.

Acknowledgements

The project was supported by ARO-MIPR-125-93 to the Naval Postgraduate School and was monitored by Dr. T.L. Doligalski. Additional support was received by AFOSR-MIPR-93-0003 which was monitored by Maj. D.B. Fant. The work was carried out in the Fluid Mechanics Laboratory Branch of NASA Ames Research Center. The steady encouragement of Dr. S.S. Davis, Chief, FML Branch, the support of Mr. J.D. Loomis in the conduct of experiments and the interferogram image processing support of Ms. S. Nado are greatly appreciated.

5. References

[1]McCroskey, W.J., McAlister, K.W., Carr, L.W., Pucci, S.L., Lambert, O., and Indergrand, R.F., "Dynamic Stall on Advanced Airfoil Sections", *Journal of American Helicopters Society*, Vol. 26, No. 3, 1985, pp. 40-50.

[2]Lorber, P.F. and Carta, F.O., "Unsteady Stall Penetration Experiments at High Reynolds Number", AFOSR-TR-87-1202, April 1987.

[3]Chandrasekhara, M.S. and Carr, L.W., "Flow Visualization Studies of the Mach Number Effects on the Dynamic Stall of an Oscillating Airfoil", *Journal of Aircraft*, Vol. 27, No. 6, 1990, pp. 516-522.

[4]Chandrasekhara, M.S., Ahmed , S. and Carr, L.W., "Schlieren Studies of Compressibility Effects on Dynamic Stall of Airfoils in Transient Pitching Motion", *Journal of Aircraft*, Vol. 30, No. 2, 1993, pp. 213-220.

[5]Gostelow, J.P., Blunden, A.R., and Walker, G.J., "Effects of Free-Stream Turbulence and Adverse Pressure Gradients on Boundary Layer Transition", *ASME Paper No. 92-GT-380*, presented at the International Gas Turbine and Aero Engine Congress and Exposition, Cologne, Germany, June, 1992.

[6]Jones, R., and Williams, D.H., "The Effect of Surface Roughness on the Characteristics of the Aerofoils N.A.C.A. 0012 and R.A.F. 34". *Reports and Memoranda No. 1708*, National Physical Laboratory, U.K., Feb. 1936.

[7]Nakamura, Y., and Tomonari, Y., "The Effects of Roughness on the Flow Past Circular Cylinders at High Reynolds Numbers", *Journal of Fluid Mechanics*, Vol. 123, 1982, pp. 363-378.

[8]Pope, A., and Goin, K.L., *High Speed Wind Tunnel Testing*, Kraeger Publishing Company, New York, NY, 1978.

[9]Preston, J.H., "The Minimum Reynolds Number for a Turbulent Boundary Layer and the Selection of a Transition Device", *Journal of Fluid Mechanics*, No. 3, Part 4, 1958, pp. 373-384.

[10]Carr, L.W., and Chandrasekhara, M.S., "Design and Development of a Compressible Dynamic Stall Facility", *Journal of Aircraft*, Vol. 29, No. 3, 1992, pp. 314-318.

[11]Wilder, M.C., Chandrasekhara, M.S., and Carr, L.W., "Transition Effects on Compressible Dynamic Stall of Transiently Pitching Airfoils", AIAA Paper 93-2978, July, 1993.

[12]Brock, N.J., Chandrasekhara, M.S., and Carr, L.W., "A Real Time Interferometry System for Unsteady Flow Measurements", *ICIASF'91 RECORD*, IEEE Publication 91-CH3028-8, pp. 423-430.

[13]Carr, L.W., Chandrasekhara, M.S., and Brock, N.J., "A Quantitative Study of Compressible Flow on an Oscillating Airfoil", AIAA Paper 91-1683, To appear in *Journal of Aircraft*

[14]Chandrasekhara, M.S., Carr, L.W., and Wilder, M.C., "Interferometric Investigations of Compressible Dynamic Stall Over a Transiently Pitching Airfoil", *AIAA Journal*, Vol. 32, No. 3, 1994, pp. 586-593.

[15]Visbal, M.R., "Effect of Compressibility on Dynamic Stall of a Pitching Airfoil", AIAA Paper 88-0132, Jan. 1988.

[16]Ekaterinaris, J.A., "Compressible Studies of Dynamic Stall", AIAA Paper 89-0024, Jan., 1989.

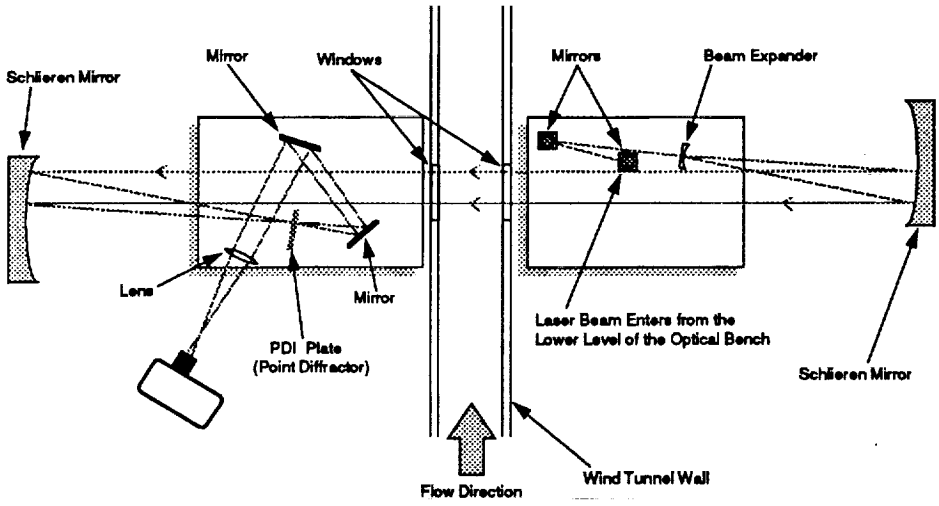

Fig. 1. Schematic of the PDI Optical Arrangement.

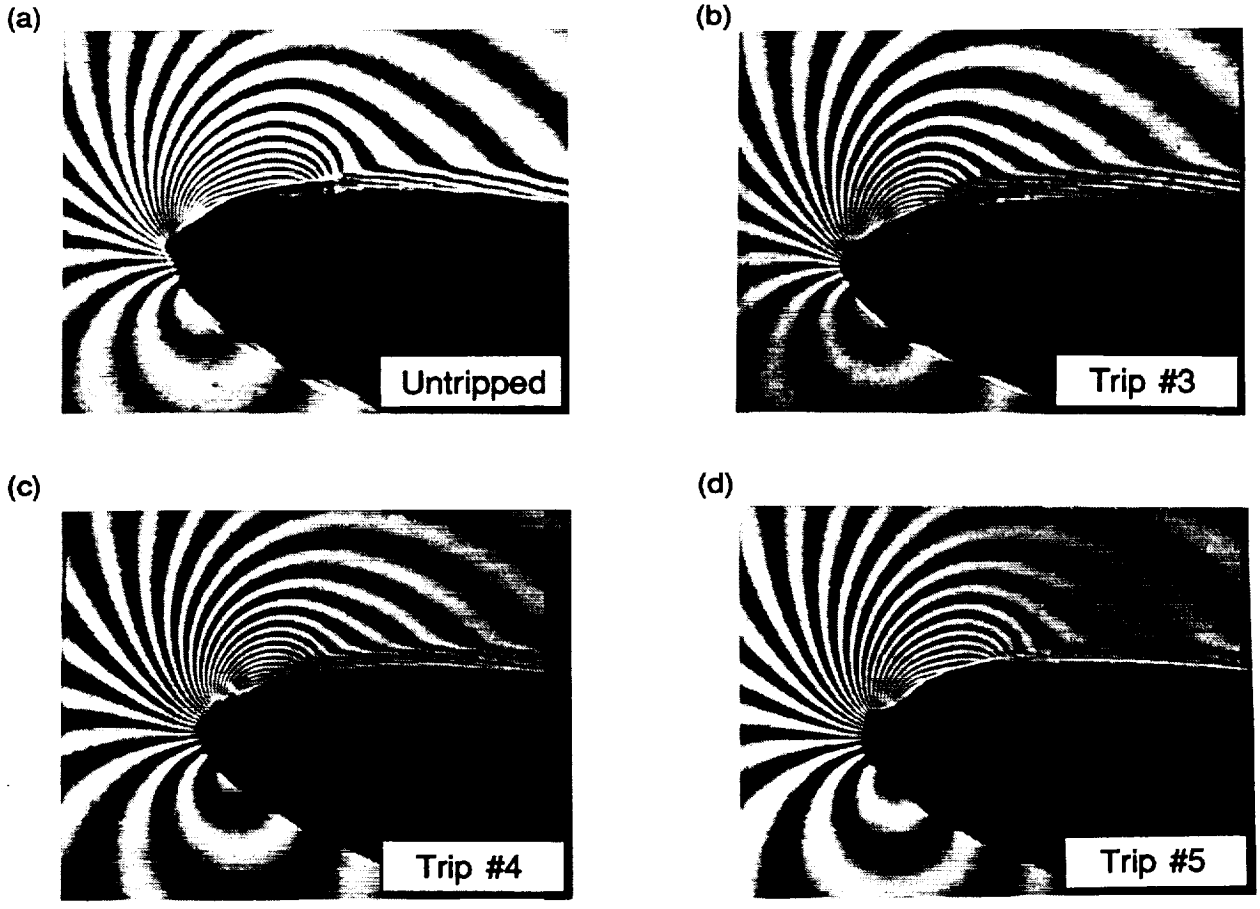

Fig. 2. PDI Images of Untripped and Tripped Flows for M = 0.3, k = 0.05, $\alpha = 10.0^{o}$.
(a) Untripped, (b) Trip #3, (c) Trip #4, (d) Trip #5.

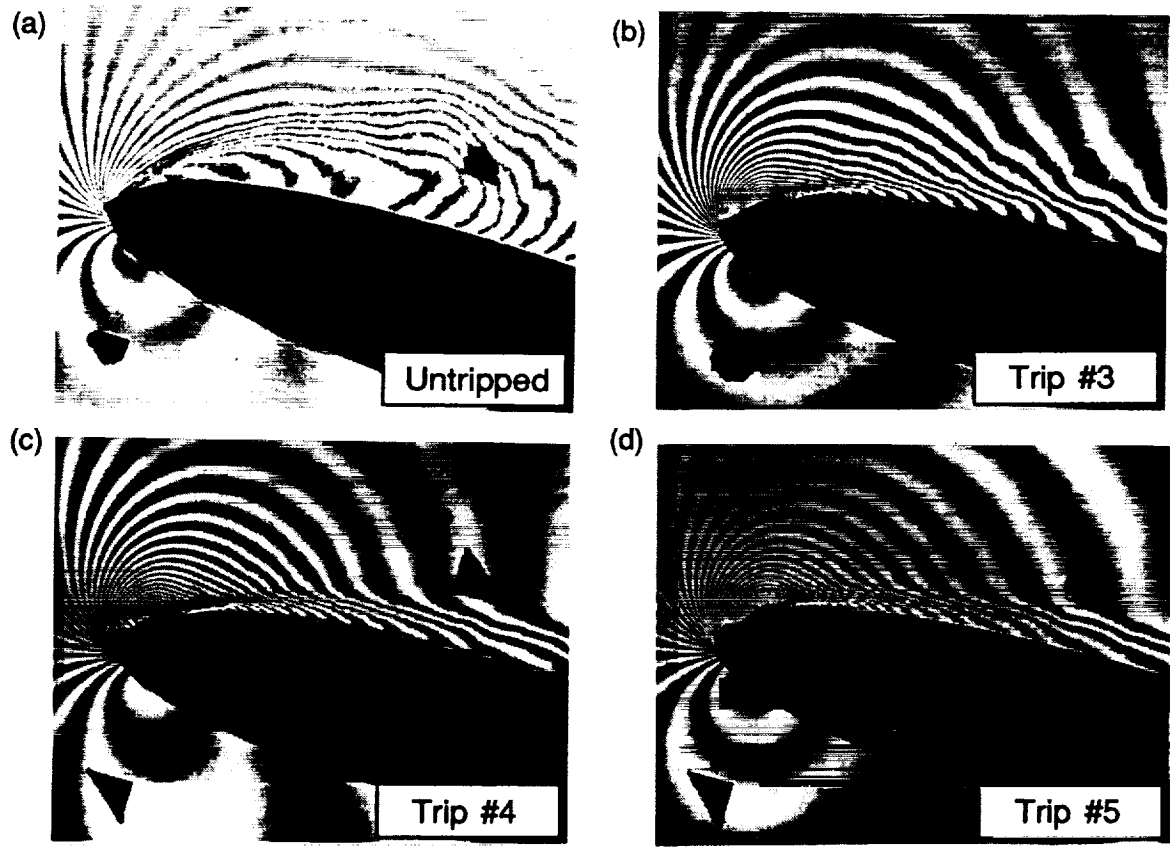

Fig. 3. PDI Images of Untripped and Tripped Flows for M = 0.3, k = 0.05, α = 13.99°.
(a) Untripped, (b) Trip #3, (c) Trip #4, (d) Trip #5.

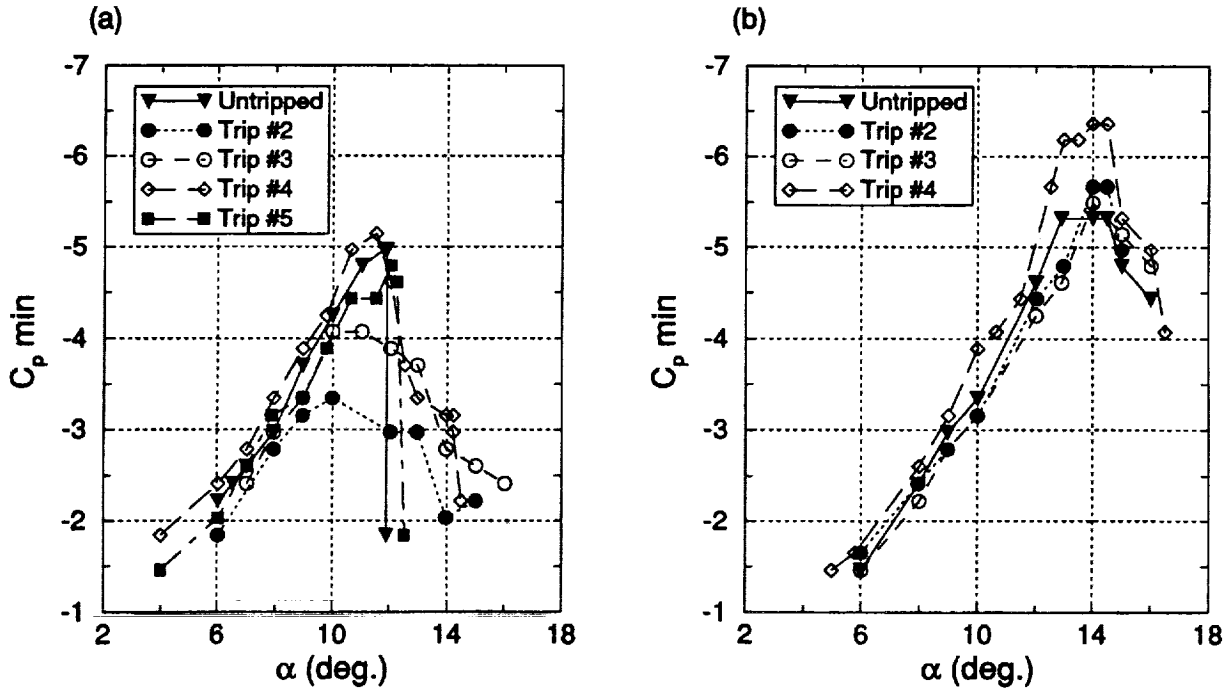

Fig. 4. The Effect of Tripping on the Development of the Minimum C_p for M = 0.3. (a) k = 0, (b) k = 0.1.

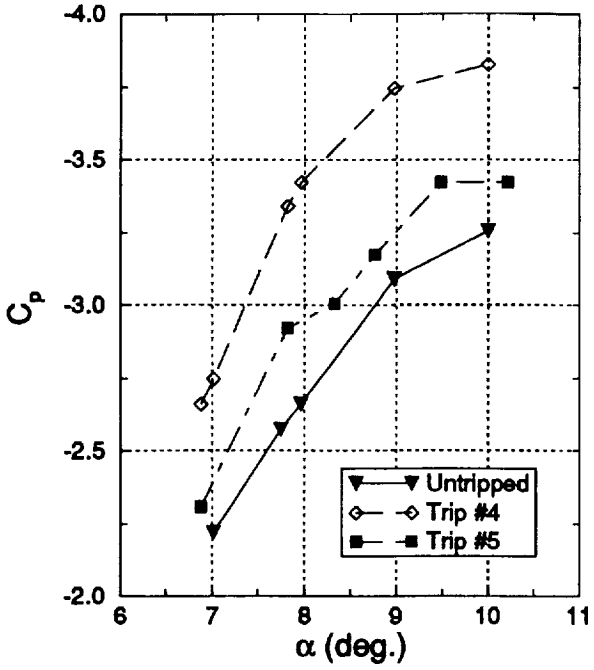

Fig. 5. The Effect of Tripping on the Development of the Minimum C_p for M = 0.45, k = 0.05.

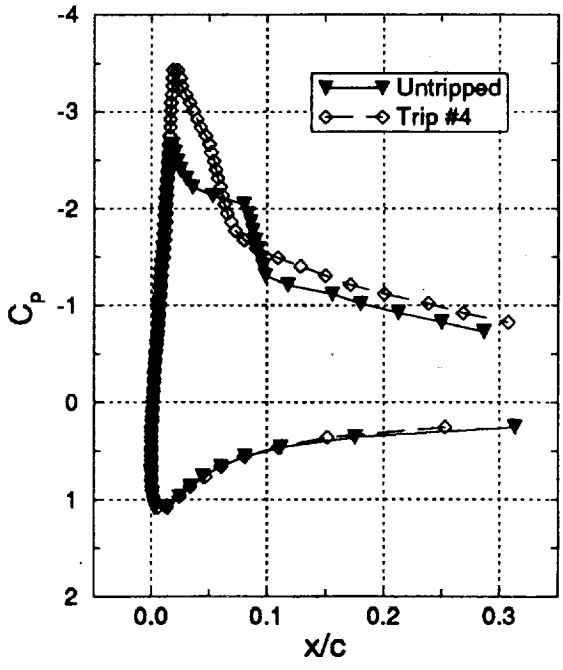

Fig. 6b. Surface Pressure Distribution for Untripped and Tripped Flows for M = 0.45, k = 0.05, α = 7.97°.

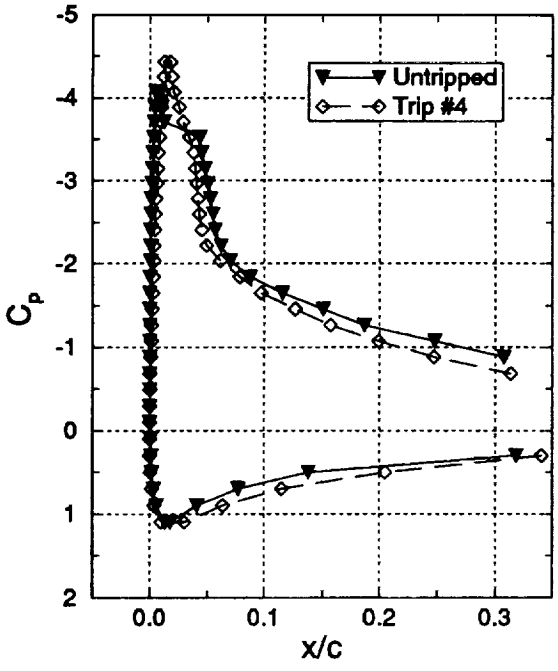

Fig. 6a. Surface Pressure Distribution for Untripped and Tripped Flows for M = 0.3, k = 0.05, α = 10.65°.

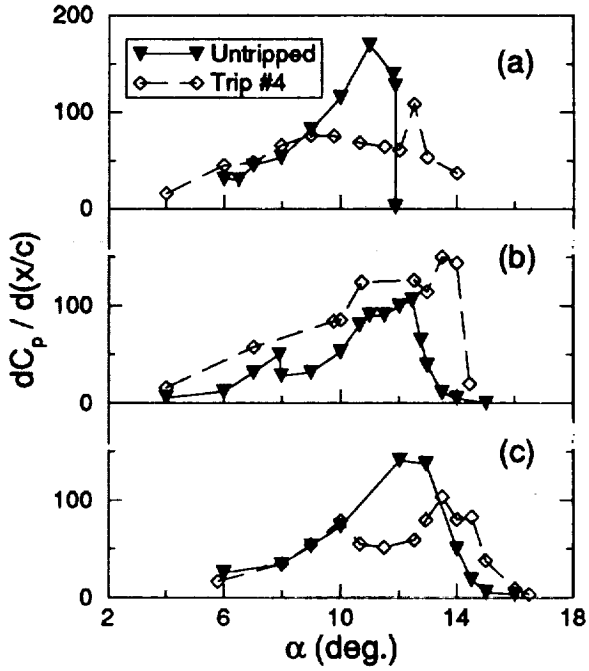

Fig. 7. Leading-Edge Adverse Pressure Gradient Development for M = 0.3. (a) k = 0, (b) k = 0.05, (c) k = 0.1.

(a)

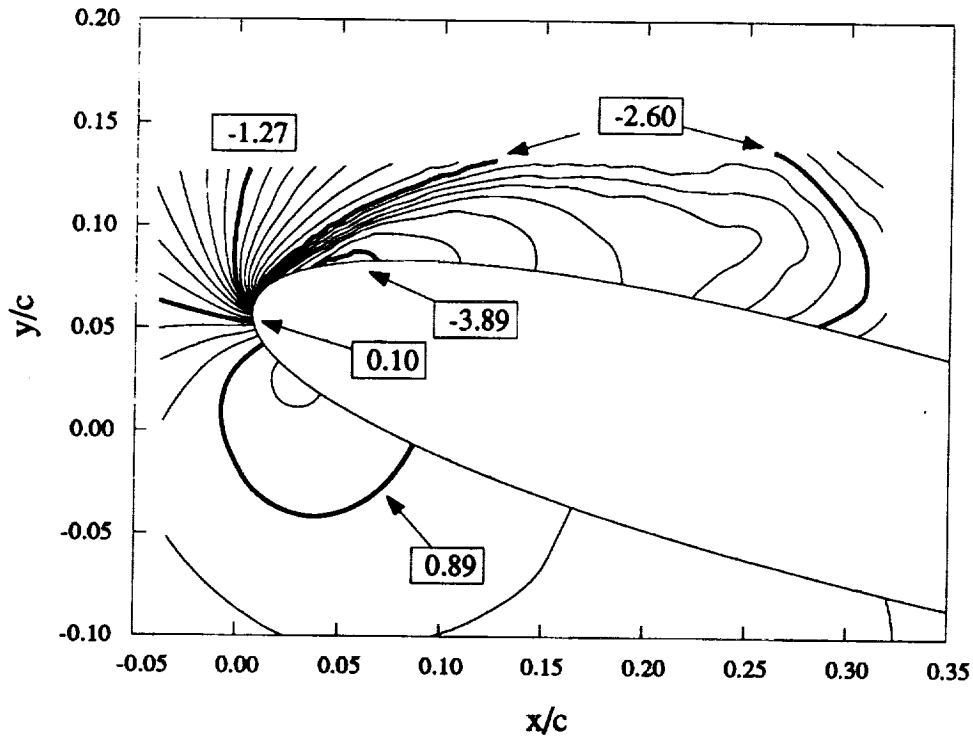

(b)

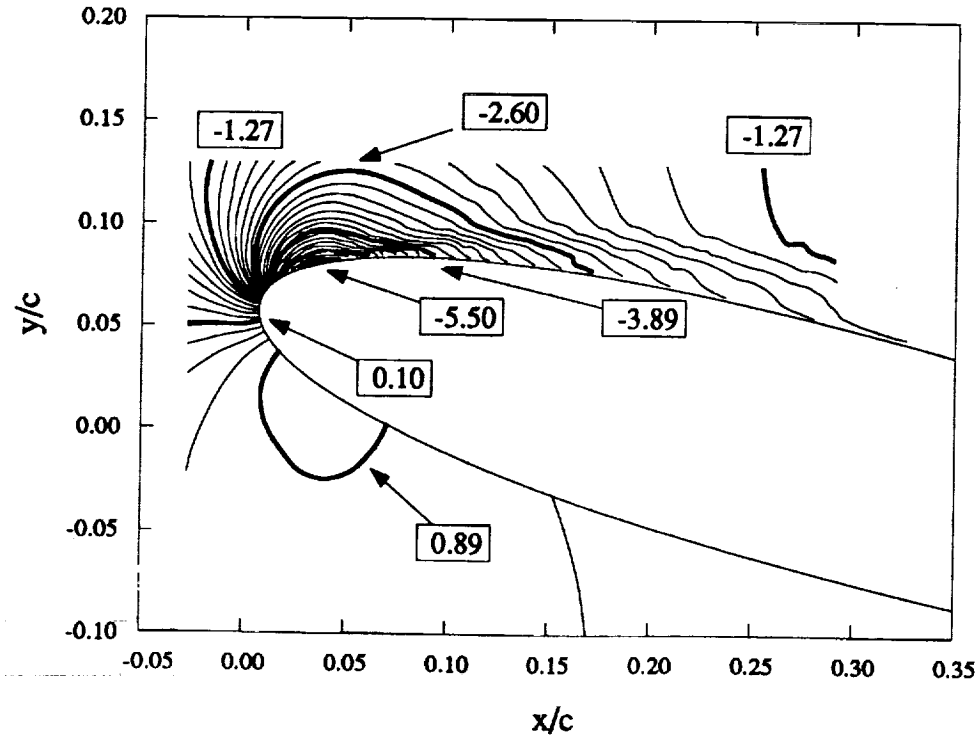

Fig. 8. Global Pressure Coefficient Field at M = 0.3, k = 0.05, $\alpha = 13.99^{o}$. (a) Untripped, (b) Trip #4.

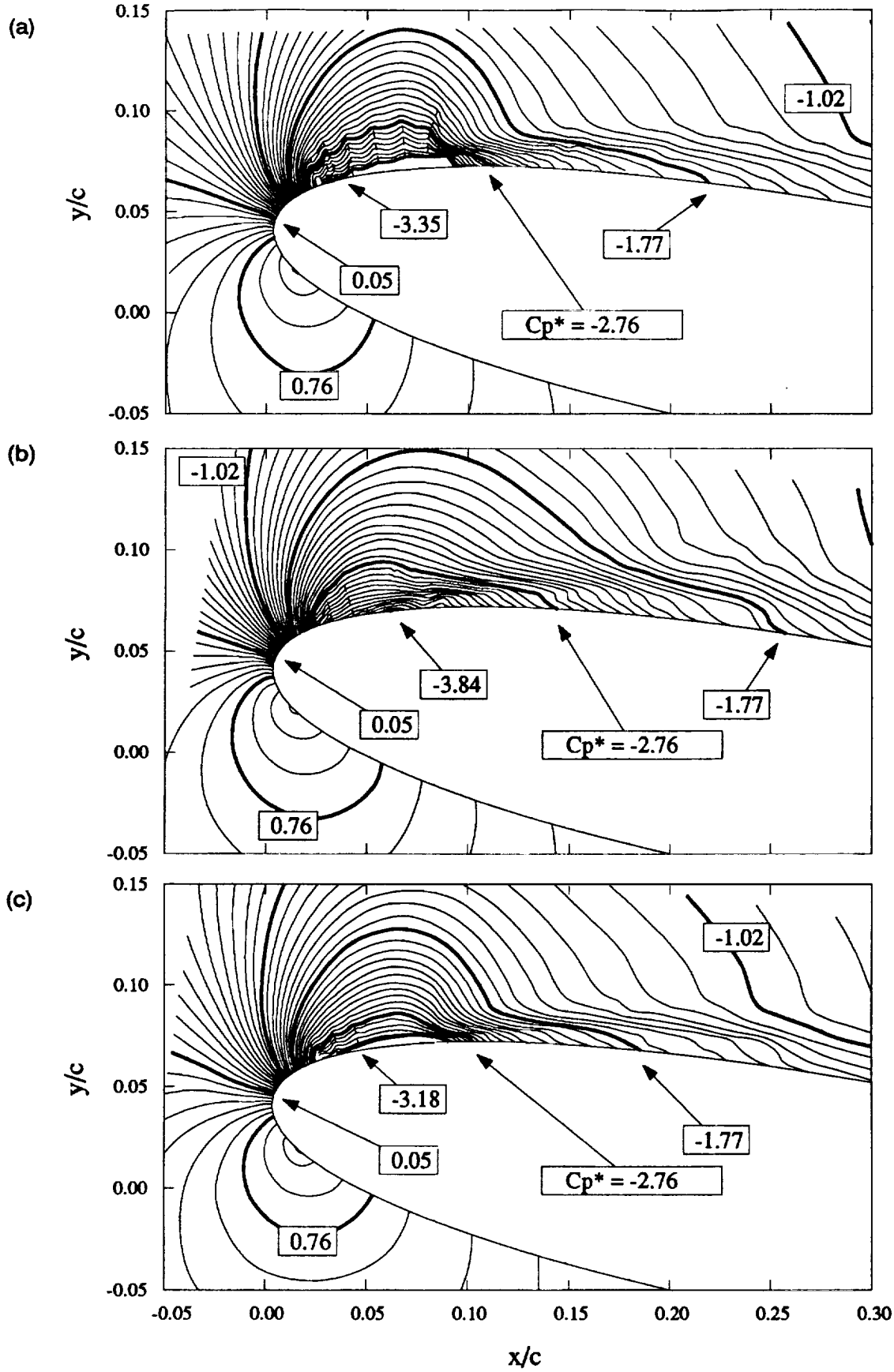

Fig. 9. Global Pressure Coefficient Field at M = 0.45, k = 0.05, $\alpha = 10.0^{o}$. (a) Untripped, (b) Trip #4, (c) Trip #5.

Appendix D:

A Phase-Locked High-Speed Real-Time Interferometry System for Large Amplitude Unsteady Flows

A Phase-Locked High-Speed Real-Time Interferometry System For Large Amplitude Unsteady Flows

M.S.Chandrasekhara, Naval Postgraduate School, Monterey, CA;
D.D.Squires, Sverdrup Technology Inc., Moffett Field, CA;
M.C.Wilder, MCAT Institute, San Jose, CA;
and
L.W.Carr, U.S.Army ATCOM, NASA Ames Research Center, Moffett Field, CA

7th International Symposium on Applications of Laser Techniques to Fluid Mechanics
July 11-14, 1994
Lisbon, Portugal

A PHASE-LOCKED HIGH-SPEED REAL-TIME INTERFEROMETRY SYSTEM FOR LARGE AMPLITUDE UNSTEADY FLOWS

M.S. Chandrasekhara
Navy-NASA Joint Institute of Aeronautics
Department of Aeronautics and Astronautics
Naval Postgraduate School, Monterey, CA 93943, U.S.A.

D.D.Squires
Sverdrup Technology Inc., Moffett Field, CA 94035, U.S.A.

M.C. Wilder
Navy-NASA Joint Institute of Aeronautics and
MCAT Institute, San Jose, CA 95127, U.S.A.

and

L.W. Carr
Aeroflightdynamics Directorate, U.S.Army ATCOM and,
Fluid Dynamics Research Branch
NASA Ames Research Center, Moffett Field, CA 94035-1000, U.S.A.

ABSTRACT

A high-speed phase-locked interferometry system has been designed and developed for real-time measurements of the dynamic stall flow over a pitching airfoil. Point diffraction interferograms of incipient flow separation over a sinusoidally oscillating airfoil have been obtained at framing rates of up to 20 KHz and for free stream Mach numbers of 0.3 and 0.45. The images were recorded on 35mm ASA 125 and ASA 400 films using a drum camera. Special electronic timing and synchronizing circuits were developed to trigger the laser light source from the camera and to initiate acquisition of the interferogram sequence from any desired phase angle of oscillation. The airfoil instantaneous angle of attack data provided by an optical encoder was recorded via a FIFO data buffer into a microcomputer. The interferograms have been analyzed using software developed in-house to get quantitative flow density and pressure distributions.

1. INTRODUCTION

Research on compressibility effects on dynamic stall of pitching airfoils is on-going at the U.S. Navy-NASA Joint Institute of Aeronautics and is being conducted in the Fluid Mechanics Laboratory of NASA Ames Research Center. The phenomenon of dynamic stall pertains to the production of lift at angles of attack well beyond the static stall angle of attack by rapidly pitching an airfoil. The problem is of importance to helicopters and fighter aircraft. Dynamic stall occurs on the retreating blade of a helicopter as it is pitched to high angles of attack during the portion of the blade revolution when it is moving with the wind. A fighter aircraft performing a rapid maneuver also experiences dynamic stall. The process is characterized by the formation of a large vortex at the leading edge (known as the dynamic stall vortex) whose vorticity is responsible for the enhanced lift. However, its convection over the airfoil upper surface needs to be avoided since it produces strong pitching moment variations, which are destructive to the aircraft. The current lack of understanding of the full flow details needed to prevent these undesirable effects has been responsible for the phenomenon remaining unexploited thus far. Another characteristic feature of the flow is the large flow accelerations around the leading edge, resulting in the onset of compressibility effects at a very low free stream Mach number of 0.2, [McCroskey(1981)]. The local flow could become supersonic and form a series of shocks. [Chandrasekhara et al(1994)]. The various fine scale events of the flow that are present for the different flow conditions need to be properly understood before an effective means of controlling the flow can be devised.

As part of this study, a real-time interferometry method known as point diffraction interferometry(PDI) has been developed, [Brock et al (1991), Carr et al (1991)] to map the instantaneous global flow details. This effort has been successful in delivering sharp, high-contrast interferograms of the flow for all conditions of the experiment. The interferograms are obtained as conditionally sampled images and have provided the first insight into the the origination of dynamic stall from the bursting of the laminar separation bubble, flow field pressure distribution and other critical flow details. However, capturing the full flow sequence takes several cycles of motion. The rapid changes that occur in the flow, especially the details of the dynamic stall vortex formation and the shock/boundary layer interactions leading to possible premature flow separation, do not repeat perfectly from cycle to cycle because of the influence of the slight variations in the pitching history for each cycle. Thus, there is a need to obtain the flow details in just one pitching cycle, as they occur. It is this need that prompted the design and development of the very high-speed interferogram recording system being presented in this paper.

2. DESIGN SPECIFICATIONS

The studies are being conducted on a NACA 0012 airfoil with a chord length of 7.62cm in the Compressible Dynamic Stall Facility(CDSF). Two different drive systems could be used in the CDSF to produce either an oscillatory pitching motion or a constant rate transient pitching motion of the airfoil. The angle of attack variation in the former case is given by $\alpha = \alpha_0 + \alpha_m \sin \omega t$ with the mean angle of attack α_0 and the amplitude α_m variable from $0^0 - 15^0$ and $2^0 - 10^0$, respectively. The maximum frequency of oscillation is 100 Hz. The constant rate pitch drive produces a rapid change of angle of attack from $0^0 - 60^0$ at rates as high as 3600 degrees/sec and the motion is completed in 15 millisec. Earlier work by Carr et al (1991) has shown that the events of dynamic stall onset occur rapidly over a small angle of attack range

of about 0.5 to 1.0 degree. Thus, in order to have a resolution of 0.1 degree or better at the limits of operation of either drive system, a camera speed of 36 KHz or more is necessary.

The very large flow acceleration (and concomitant density variations around the airfoil leading edge which could create as many as 60 fringes/millimeter at the airfoil) and the rapidity of the development of the dynamic stall vortex or the shock induced flow events, result in interference fringes that evolve and move at very high frequency ($\approx$ KHz). This necessitates the use of extremely short light pulse duration, typically nanoseconds. These challenges require the use of a laser that produces the necessary energy for each exposure and is externally controllable at the high pulse rates.

The high framing rates, the short duration of the light pulse, and the low light levels preclude the use of video cameras or similar recording devices, limiting the choice to film cameras. Possible blurring of the images due to flow changes eliminates choices such as streak cameras.

It is also necessary to record the airfoil angle of attack corresponding to each frame on the film. Further, the system should be controllable in order to generate an interferogram sequence starting at any desired angle of attack.

3. DETAILS OF THE CAMERA, LASER CONTROL AND RECORDING SYSTEMS

A Qunatronix Series 100 CW/pumped Nd:YAG laser, capable of operating from DC to 50KHz was used in the experiments. It can be externally triggered without any detectable delay at all rates. The pulse duration and the energy output varied nonlinearly from 85ns and 0.14mJ at 500Hz, 420ns and 25μJ at 40KHz and 100ns and 11μJ at 50KHz. At the rates used for the high-speed interferometry experiments being reported, the corresponding numbers were: 140ns and 65μJ at 10KHz and 240ns and 17μJ at 20KHz, at nearly full current settings. The energy density in the laser light pulse at 10 KHz rate was adequate to give proper exposure on ASA 100 T-MAX film; ASA 400 film was necessary at 20 KHz.

A 35 mm, variable speed Cordin drum camera (DYNAFAX Model 350) was used for image recording. A rotating 8-faceted mirror in the camera reflects the incoming light beam onto the film which is rotating in the same direction in the camera drum. Effective shutter times of 1.35μsec can be achieved at 40 KHz framing rate. At 20 KHz, this time was 2.7μsec. The camera recorded two rows of 16mm images images on the film strip, with subsequent exposures being recorded alternately in each row, but displaced 16 frames. A maximum of 224 frames can be recorded at any framing speed.

The laser was triggered by TTL pulses emitted by custom built (in-house) circuitry installed on the camera. Tuning the camera required aligning the mirror facet with the incident light beam. In order to sense the position of the mirror, an infrared (IR) emitter and detector were installed in the camera (see Fig. 1) to "see" the mirror facets as they pass. The IR detection beam was not in the optical path of the camera and the selected film was not sensitive to the 940nm IR wavelength. Each mirror facet accounted for two photo images. To obtain an image in each frame, two delayed pulses were generated from the passing of each mirror facet. Fast rise-time (1nsec) photodiodes were selected to ensure adequate signal level as the center of each mirror facet passed the detector. To aid in synchronizing the laser pulses, two additional photo detectors were placed in the camera, one at each frame position. The trigger pulse from the mirror face detection event started a delay sequence which synchronized laser pulsing to subsequent frame positions as shown in Fig. 1. Tuning of the laser-firing pulse train occurred in a circuit attached to the camera. The tuning procedure involved adjusting two delay times with the camera running: T_1, the delay between detecting a mirror facet and emitting the first TTL pulse (the trigger pulse to the laser and for data collection) and T_2, the time between the two TTL pulses. The delay times T_1 and T_2 were adjusted to maximize the laser light detected by the frame photo detectors. Once tuning was properly completed, the photo detectors were moved from the field of view to permit laser light to reach the film plane. The short effective shutter times (of 1.35 μsec at the maximum camera speed)and the high framing speeds required a careful design of the electronic system that included schemes for proper attenuation of noise.

A Nikon 55mm macro, f/2.8 lens was used on the camera. Aligning the camera along the optical axis of the interferometry system required very accurate adjustment.

Both unsteady motion producing drives referred to in section 2 are equipped with an optical encoder that produces 800 counts/cycle of motion (one oscillation cycle or one pitch-up from 0-60 degrees). It is an incremental encoder outputting a quadrature pulse train which is in turn processed by an Oscillating Airfoil Position Interface(OAPI) for phase locking and recording by the data acquisition system. The OAPI could be preset to produce a TTL event pulse (or pulse repetitively) at any desired phase angle by a series of front panel BCD switches. The TTL output pulse was used to trigger the opening of a laser safety shutter and also to initiate encoder data transfer to memory as shown in Fig. 2. The laser is enabled by the first TTL pulse from the OAPI. However, recording the encoder outputs was enabled subsequently when the system was ready. The data was recorded for each camera pulse in a 512 word first-in-first-out(FIFO) buffer. The number of frames acquired by the camera could be controlled from 0 to 224 (camera maximum) by the external electronics built for enabling the handshake between the various devices. Typically, 200 frames of point diffraction interferograms were obtained and the phase angles corresponding for each of the frames were recorded into the FIFO and later downloaded into a microVAX II computer.

4. OPERATION

The interframe pulse delay was tuned to the desired rate and the actual rate of the camera was measured using a frequency counter. The data to be reported were obtained at 11.56 KHz. Interferograms have also been obtained at 19.62KHz. The desired initial phase angle for the interferogram sequence was set using BCD switches on the OAPI front panel. Before the images were acquired, to maintain a consistent pulse energy level, the laser was triggered by an external pulse train at a 40KHz rate. This was necessary to protect the laser crystal from the giant pulse that is normally generated when the laser is pulsed after a

short lapse time. In order to prevent these pulses from exposing the film and for safety reasons, a solenoid actuated laser shutter was set up in front of the laser. A hand switch was used to initiate the controlled laser pulsing sequence, which is schematically described in Fig. 2. The corresponding timing sequence is shown in Fig. 3. After the switch is pressed, the circuitry was activated by an event pulse from the OAPI with an output pulse corresponding to the manually preselected angle of attack. The laser pulsing circuit was then inhibited (for 1.1 msec) until the laser shutter fully opened. The laser was enabled at the expiration of the delay and was actually triggered from the next camera pulse, at which time the encoder was latched and recorded in the FIFO. During this short elapsed time, the laser builds up sufficient charge to cause the first pulse to be a "small-giant" pulse, which over-exposed the first frame. This frame served to determine the first image on the film strip; thus, it was possible to accurately match the interferogram images with the phase angle of motion and to correlate the values in the FIFO buffer. A frame counter, started at the first laser-pulse event, permitted capturing the angles corresponding to each of the 200 laser pulses and hence PDI images that were recorded on film. Following the completion of the imaging, the shutter was closed and the laser returned to the constant 40KHz external triggering. The camera alignment was verified by taking test sequences on a Polapan ASA 125 film and the data was obtained on a higher resolution T-MAX 400 film.

Fig. 4 shows a schematic of the PDI optics and its implementation in the dynamic stall facility. The details of the PDI technique have been described in Brock, et al (1991). It uses one single pass of the laser beam through the test section and depends upon the ability of a pin-hole created *in-situ* in a semi-transparent plate to produce the reference beam. The signal beam passes around this pin-hole to produce interference fringes on a continuous basis in real time. In the experiment, the PDI spot was created with no-flow in the test section and once it was determined to be satisfactory (from single event polaroid pictures), the high speed images were obtained.

5. RESULTS AND DISCUSSION

5.1. Flow Development

Fig. 5 compares typical interferograms obtained with two different imaging techniques. Figures 5a and 5c were taken over a *single cycle* of airfoil motion using the high-speed filming method. Figures 5b and 5d were taken over *different cycles* of airfoil motion using the standard method of single-exposure, phase-locked, realization of the flow events. As stated earlier, the phase-locked images obtained over several cycles contain the *pitch rate history* effects as well. The airfoil was tripped in both cases and was oscillating as $\alpha = 10^0 + 10^0 \sin \omega t$ at a reduced frequency of 0.05. The free stream Mach number of the flow was 0.3. The camera framing rate was $\alpha = 10.07^0$ in the high-speed-images sequence and Fig. 5b represents the result for $\alpha = 10.00^0$ from a single-exposure recording of the event. (The triangles seen in the images are registration markers on the glass windows of the facility which are used to determine the airfoil profile during image processing. The slight dark bulge seen near the leading edge region is due to the light beam being bent away from the leading edge due to the very large local density gradients.) A careful comparison of the pictures shows that for this experimental condition of pre-dynamic stall flow, there are no significant differences between the image recording techniques and the fringe count agrees to within one fringe. Fig. 5c and 5d show the corresponding pictures for $\alpha = 13.99^0$, when the dynamic stall process has just begun. (this is evidenced by the appearance of vertical fringes in the flow immediately above the airfoil upper surface near the leading edge). A casual comparison may not show differences in the number and distribution of the fringes and hence no flow field differences, but as will be discussed later, there are differences in the initiation of the dynamic stall process from cycle to cycle, which affect the overall flow development and stall progression. Similar results were obtained at the higher framing rate of 19.62KHz.

Fig. 6a and Fig. 6b compare the global pressure distributions obtained from the images presented in Fig. 5c and Fig. 5d using custom image processing software developed in-house. It is to be noted that even though the two figures appear to be nearly identical, the corresponding pressure fields are indeed different as can be determined from the lines of constant pressure coefficients shown in the figures. The finer details of the flow in the region of dynamic stall vortex formation, $0 \leq x/c \leq 0.10$ differ measurably; Fig. 7 has been drawn to offer a comparison of these details. These differences are important since the instantaneous adverse pressure gradient development with pitching is different in the two images leading to considerably different dynamic stall developments during each pitch-up cycle, which makes the already challenging task of unsteady flow separation control even more difficult.

Fig. 8 shows the pressure distributions over the airfoil surface obtained from the interferograms presented in Fig. 5a and 5b. The pressure distributions agree for the most part. However, there is a difference of one fringe as already noted, which is the uncertainty of the PDI method itself. But, the pressures around the suction peak are somewhat different between the two cases, causing the adverse pressure gradient following the suction peak to be different, leading to major differences in pressure gradient magnitudes at higher angles of attack.

5.2. Interferogram Imaging Concerns

The image size on the film was 3.5mm in diameter and the images shown in Fig. 5a and 5c have been magnified by nearly 1000 times. Despite the large magnification factor, the quality of the images can be seen to be very good. Attempts to enlarge the original size (using extension rings) of the image met with only partial success owing to the long focal length of the mirrors and the fact that the laser beam has a small divergence angle, unlike white light.

Yet another concern in the use of the high-speed imaging system was the ability of the PDI spot to withstand the rapid exposure to the laser energy that occurred during high speed imaging. In the experiment at 20 KHz the PDI spot was exposed to a total of 3.4mJ in 10 milliseconds. At such large energy levels there was a possibility that the PDI spot could get enlarged or even damaged, thus creating inaccurate interferograms. However, the robustness of the holographic plate film coating material used for the purpose prevented this from happening.

It is worth commenting that acquisition of high speed interferograms using white light has been reported in the literature, [Desse and Pegneaux(1993)]. However, the key differences in the present study - the

requirements of phase locking, controlling the laser from the camera pulses, the need to precisely record the phase angle for each pulse (since the flow undergoes significant changes in a very small angle of attack range), and the very short duration of the pitching motion - all precluded the use other measurement methods.

6. CONCLUSIONS

A novel system for recording real-time phase-locked interferograms at very high rates has been developed for use in study of unsteady separated flows. The rapid nature of the flow changes and the extremely high gradients around the leading edge of an airfoil experiencing dynamic stall in compressible flow requires the use of such a measurement technique. The system uses a laser that can be pulsed at high rates to produce interferograms and record these on film at rates of up to 40KHz. Proper electronic interlocking has enabled precise control of the experiment and accurate recording of the resultant interferograms.

ACKNOWLEDGEMENTS

The project was supported by U.S. Air Force Office of Scientific Research through grants, AFOSR-ISSA-89-0067 and AFOSR-MIPR-92-004. Additional support was received from the Army Research Office grant ARO-MIPR-125-93. The support and encouragement of Dr. S.S.Davis, Chief, Fluid Mechanics Laboratory Branch and the help provided by Mr. N.J.Brock and Mr. B.J.Weber of Aerometrics, Inc. in preparing the laser specifications are gratefully acknowledged.

REFERENCES

1. Brock, N., Chandrasekhara, M.S. & Carr, L.W. 1991, A Real-Time Interferometry System for Unsteady Flow Measurements", ICIASF'91 RECORD, IEEE Publication 91CH3028 – 8, pp. 423-430.

2. Carr, L.W., Chandrasekhara, M.S., Ahmed, S. & Brock, N. 1994, A Study of Dynamic Stall Using Real-Time Interferometry, To appear in AIAA J. Aircraft.

3. Chandrasekhara M.S. & Carr, L.W. 1990, Flow Visualization Studies of the Mach Number Effects on the Dynamic Stall of Oscillating Airfoils, AIAA J. Aircraft, Vol. 27, No. 6, pp. 516-522.

4. Chandrasekhara, M.S., Carr L.W. & Wilder, M.C., 1994, Interferometric Investigations of Compressible Dynamic Stall Over a Transiently Pitching Airfoil, AIAA Journal, Vol. 32, No. 3, pp. 586-593.

5. Desse J.M. & Pegneaux, J.C. 1993, Direct Measurement of the Density Field Using High Speed Differential Interferometry, Expts. in Fluids, Vol. 15, pp. 452-458.

6. McCroskey, W.J. 1981, The Phenomenon of Dynamic Stall, NASA TM-81264, March.

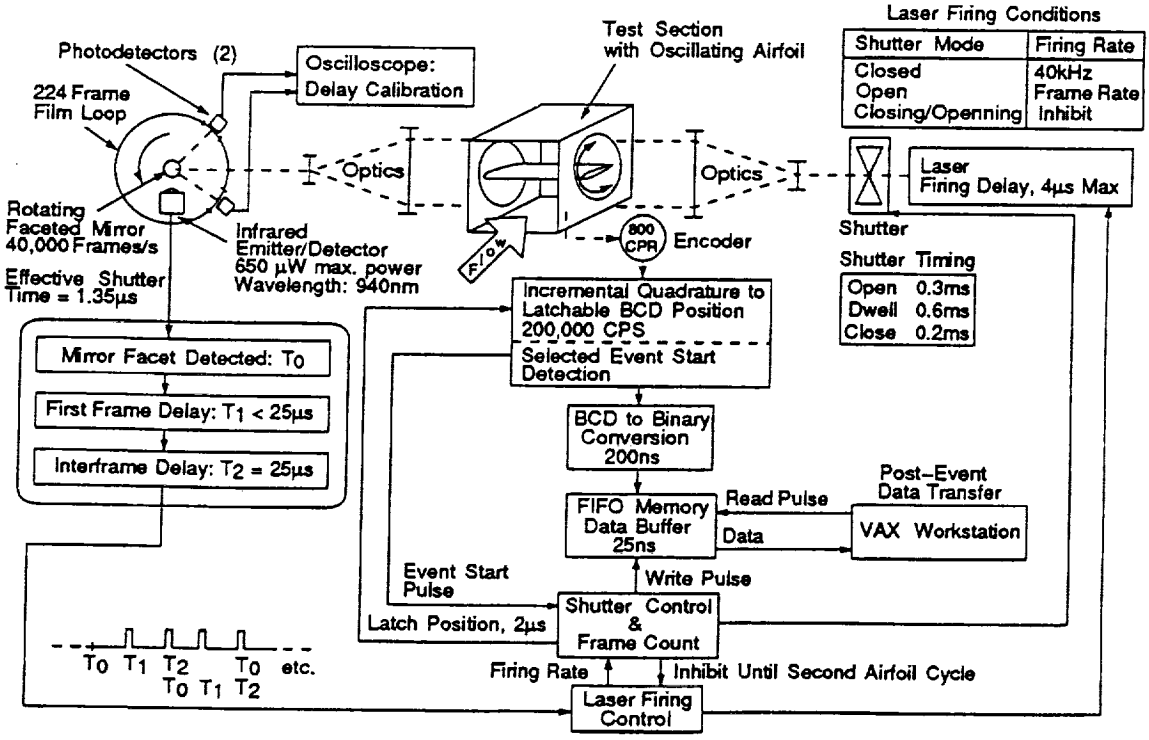

Figure 1. Block Diagram of Camera/Laser Synchronization for the High–Speed Interferometry System.

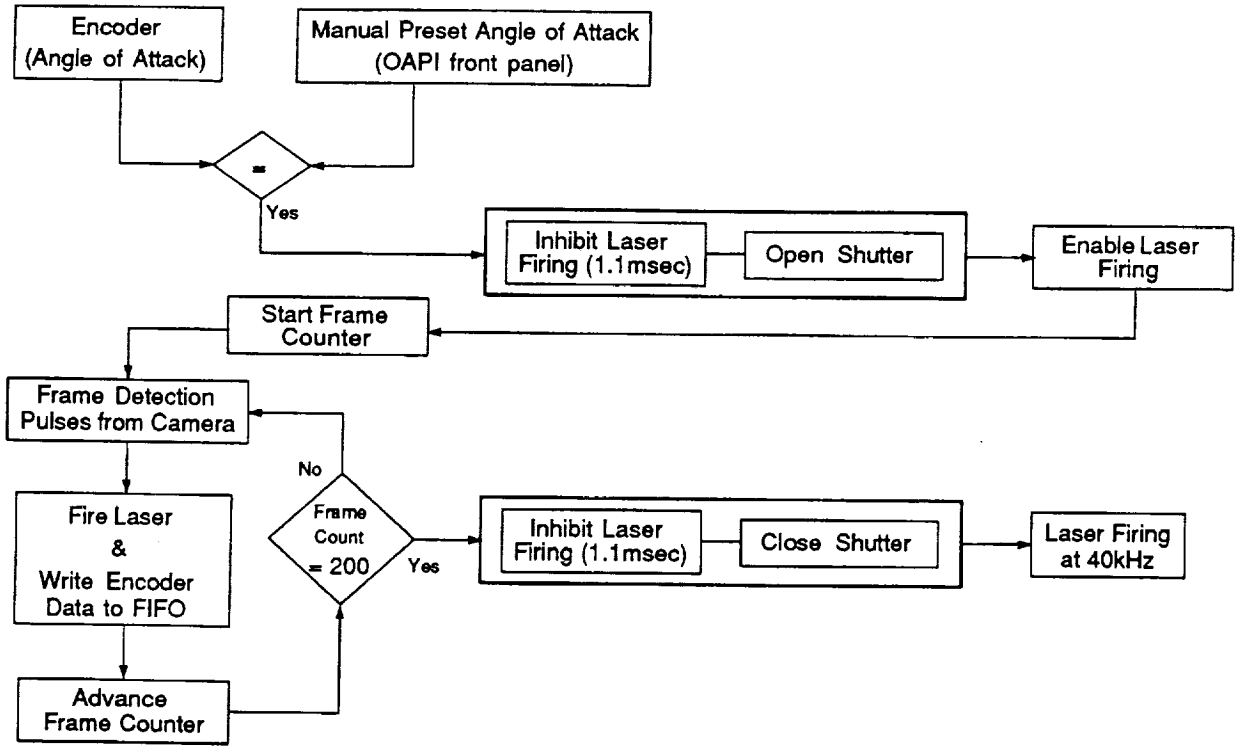

Fig 2. Flowchart of Events Following Handswitch "FIRE" for the High-Speed Interferometry System.

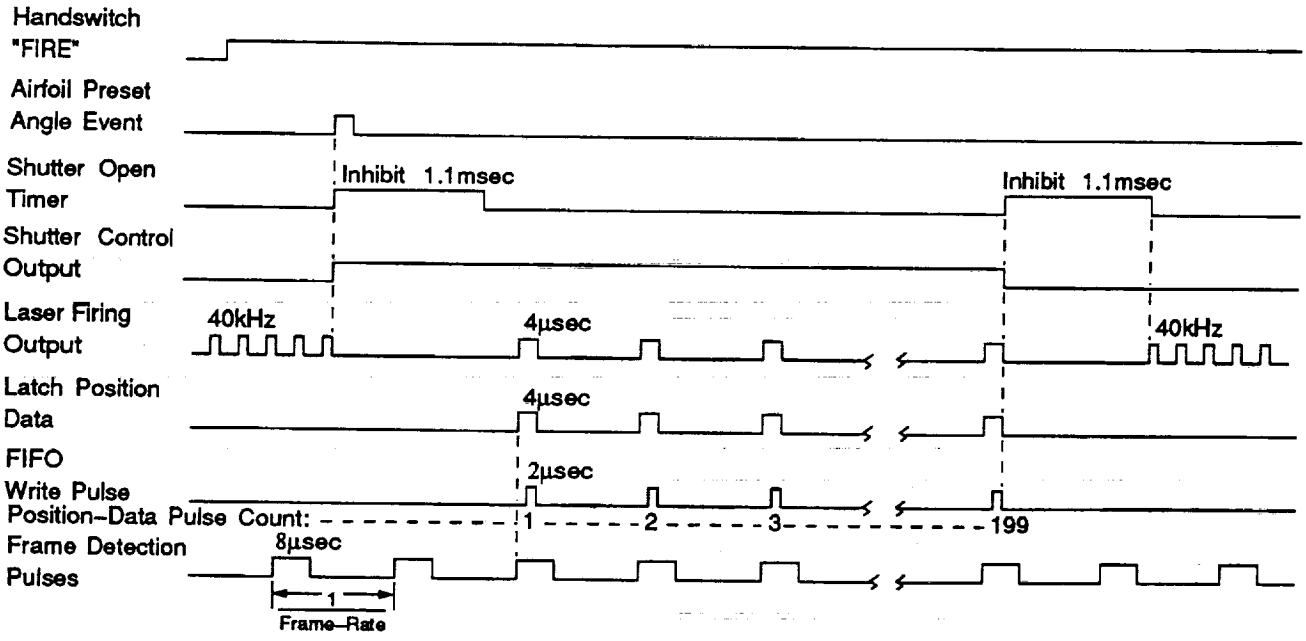

Note: Event edges are shown in proper sequence, but not properly scaled. Refer to the pulse durations shown.

Fig 3. Timing Sequence for the High-Speed Interferometry System.

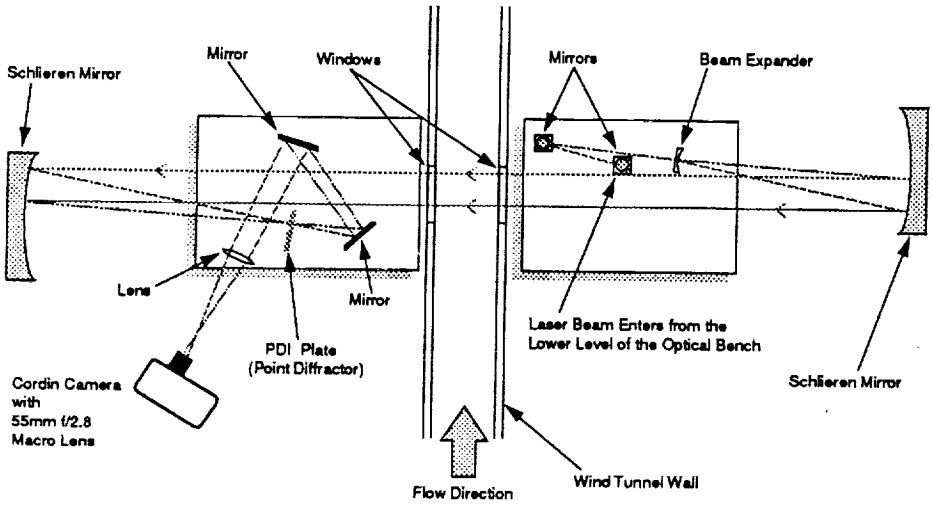

Fig. 4. Schematic of the Point Diffraction Interferometry System.

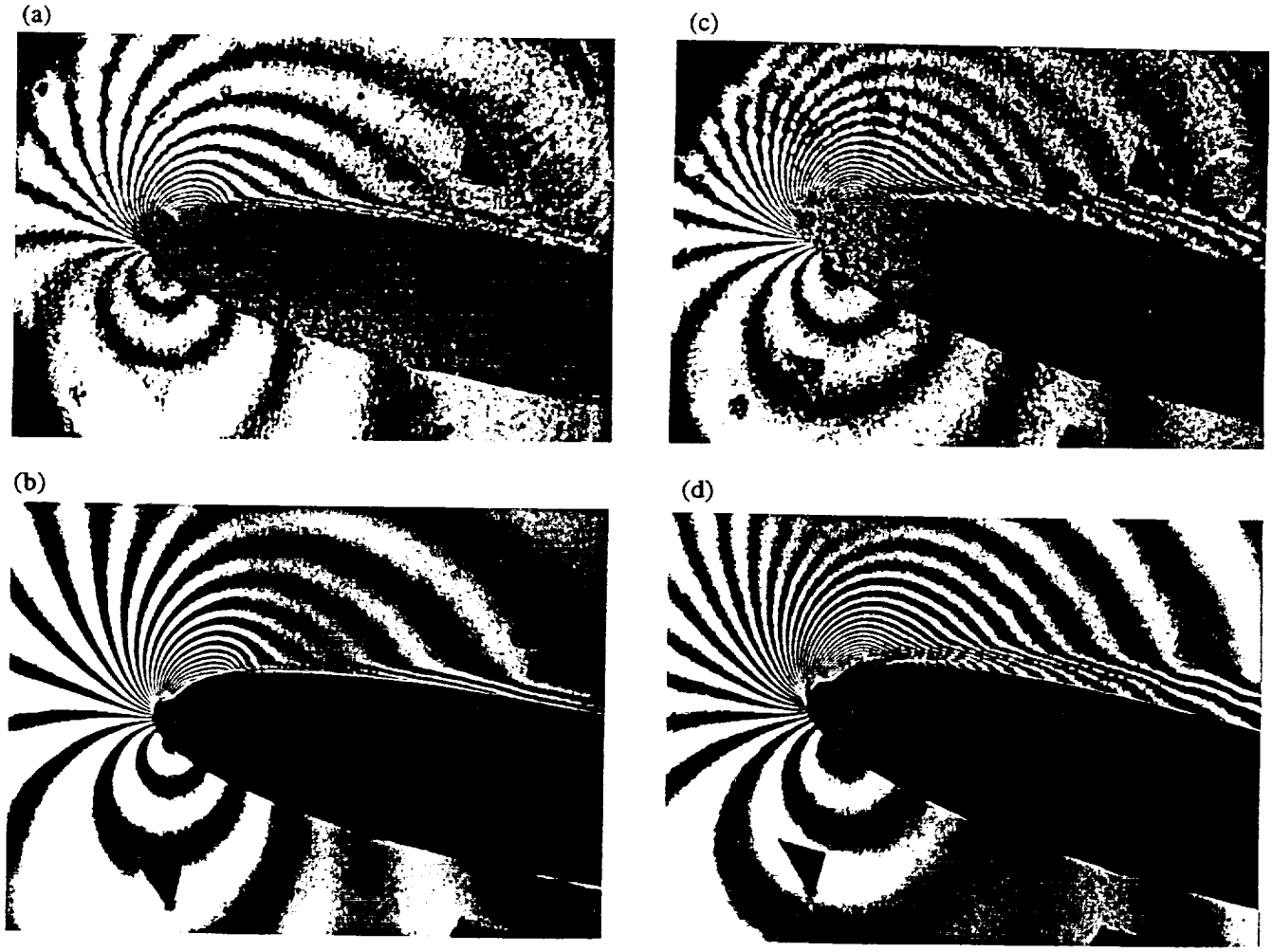

Fig. 5. Representative Interferogram Images of the Flow Field for M = 0.3, k = 0.05. (a) α = 10.07°, High–Speed Camera at 11.56kHz, (b) α = 10.00°, Single–Exposure Camera, (c) α = 13.99°, High–Speed Camera at 11.56kHz, (d) α = 13.99°, Single–Exposure Camera.

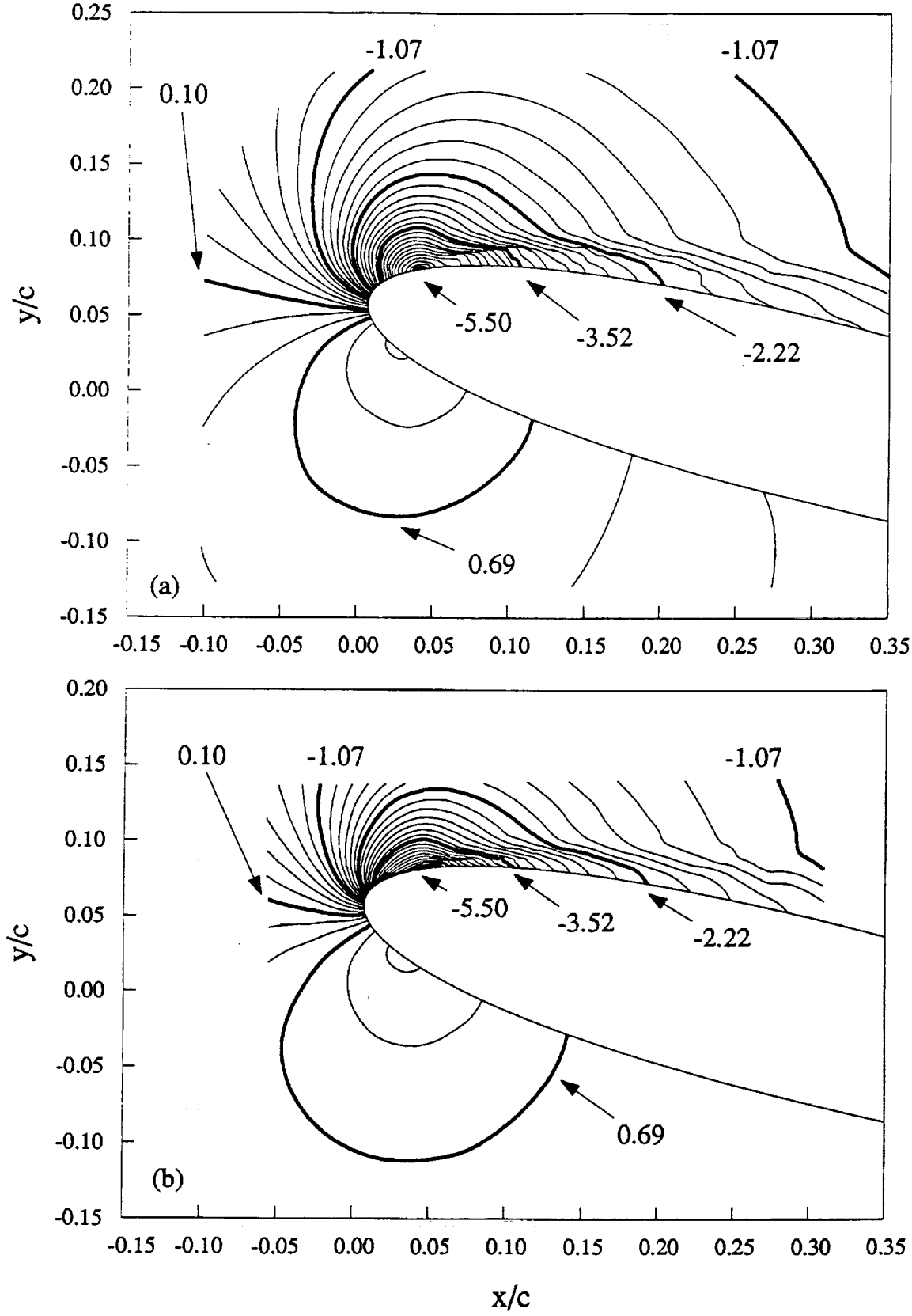

Fig. 6. Global Pressure Distributions for M = 0.3, k = 0.05, $\alpha = 13.99^{o}$. (a) From the High–Speed Camera Image, Fig. 5c. (b) From the Single–Exposure Camera Image, Fig. 5d.

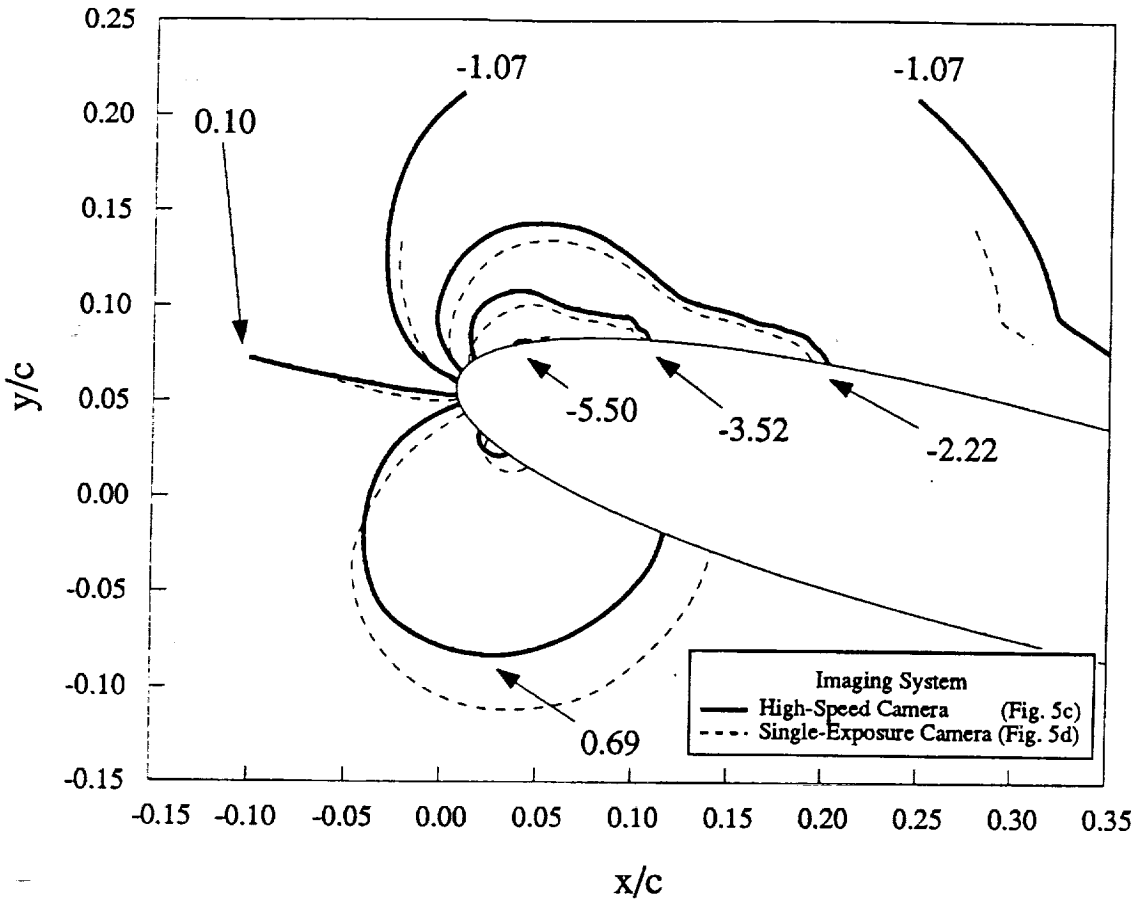

Figure 7. Comparison of the Global Pressure Distributions Obtained with the High-Speed and Single-Exposure Imaging Systems

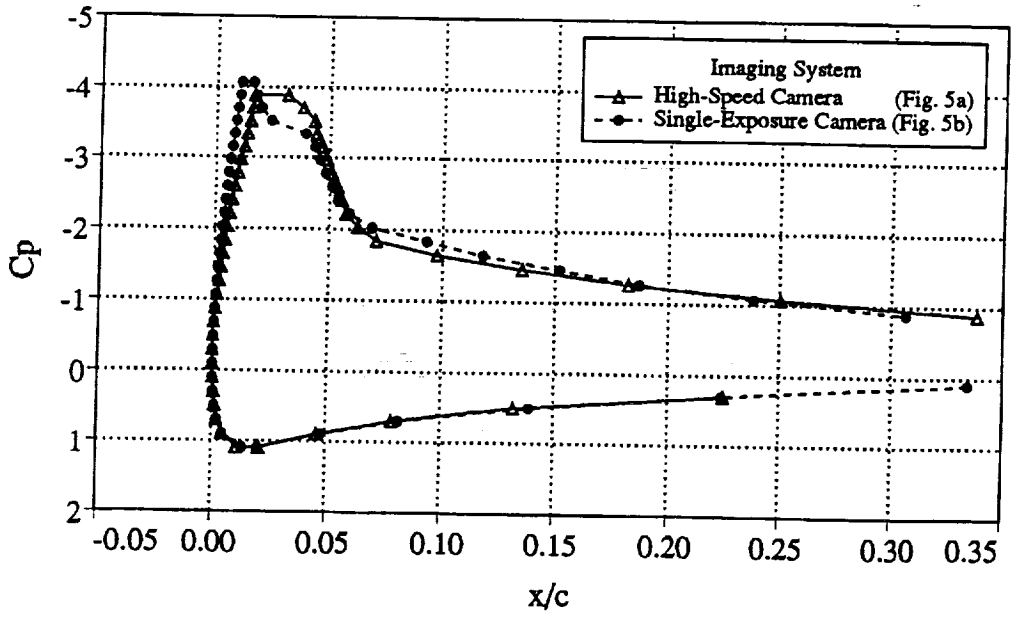

Figure 8. Comparison of the Surface Pressure Coefficient Distributions Obtained with the High-Speed and Single-Exposure Imaging Systems